Three-dimensional Blueprinting of Molecular Patterns in Liquid Crystalline Polymers

by

Mohsen Tabrizi

B.Sc. in Mechanical Engineering, Sharif University of Technology, 2013

M.Sc. in Advanced Manufacturing Technology and Systems Management, University of Manchester, 2015

Submitted to the Graduate Faculty of
the Swanson School of Engineering in partial fulfillment
of the requirements for the degree of

Doctor of Philosophy

University of Pittsburgh

2022

UNIVERSITY OF PITTSBURGH

SWANSON SCHOOL OF ENGINEERING

This dissertation was presented

by

Mohsen Tabrizi

It was defended on

March 16, 2022

and approved by

M. Ravi Shankar, Ph.D., Professor, Department of Industrial Engineering

Bopaya Bidanda, Ph.D., Ernest E. Roth Professor, Department of Industrial Engineering

Youngjae Chun, Ph.D., Associate Professor, Department of Industrial Engineering

Carmel Majidi, Ph.D., Associate Professor, Department of Mechanical Engineering, Carnegie Mellon University

Zeynep Temel, Ph.D., Assistant Professor, Robotics Institute, Carnegie Mellon University

Dissertation Director: M. Ravi Shankar, Ph.D., Professor, Department of Industrial Engineering

Three-dimensional Blueprinting of Molecular Patterns in Liquid Crystalline Polymers

Mohsen Tabrizi, PhD

University of Pittsburgh, 2022

The ability to pattern material response, voxel-by-voxel, to direct actuation and manipulation in macroscopic structures can enable devices that utilize ambient stimuli to produce functional responses at length-scales ranging from the micro- to the macroscopic. Fabricating stimuli-responsive liquid crystalline (LC) polymeric materials, where the molecular director is indexably defined in three-dimensional freeforms can be a key enabler. Here, we exploited the combination of anisotropic magnetic susceptibility of the LC monomers in a reorientable magnetic field and spatially-selective photopolymerization using a digital micromirror device to independently define molecular orientation in light and/or heat responsive multi-material elements, which are additively incorporated into three-dimensional freeforms. This enables structural complexity across length scales in non-trivial geometries which are responsive to either heat or light. In this work, the mechanism of magnetically controlling the molecular orientation of various LC polymeric materials is studied. Based on the results, a new liquid crystalline elastomer (LCE) that can be aligned by low-intensity magnetic field was developed. The proposed platform and new LCE material are further exploited by the development of a battery-free, remotely controlled, bioinspired microflier with potential applications in environmental monitoring. This study can provide the opportunity to expand the applications of molecularly ordered materials to soft robotics and micromechanical devices that are driven by unconventional stimuli. The current and ongoing research works to expand the implementations of this work vision including sub-voxel control over molecular order, endowing multifunctionality, scaling the artificial muscle down to nanoscale, and exploitation of self-sensing and self-regulation are discussed briefly in the end.

Table of Contents

List of Tables

List of Figures

Preface

To my family, and close friends.

1.0 Introduction

Regulating functional properties and directing structural evolution in active polymers by programming composition and microstructural gradients during fabrication is a versatile route for realizing soft machines. Integrating active elements with suspensory structures, including fluidic [1] and solid [2] mechanical logic elements has been used to encode macroscopic actuation and manipulation in soft robots. If individual voxels (volume elements) of the material themselves become capable of active functionalities, a broader design-space of encodable responses can emerge by blurring the distinction between the active and the suspensory, structural elements. The material itself becomes the robotic manipulator. For example, programming anisotropic magnetic domain structures in magnetic particle-infused polymeric inks can enable soft robots, which manifest non-linear shape transformations using magnetic fields [3]. Biomimetic transformations have also been realized via anisotropic swelling in structures 3D printed with aligned nano-cellulose fibers [4]. The underlying organizing principle is to exercise voxel-by-voxel control over both the geometry and the anisotropic coupling between a stimulus and material response. When responsiveness, geometry, and mechanics conspire, emergent design opportunities become possible.

Liquid-crystal (LC) polymeric materials are distinguished among stimuli-responsive materials due to their ability to reversibly generate work densities in excess of $\sim J/kg$ with unusual force-displacement characteristics. Notably, the ability to simultaneously generate large strains and actuation stresses from order-disorder transitions of the long-range orientational order in the macromolecular network [5, 6, 7]. These materials are composed of rigid rod-shaped molecules, also known as mesogens. Figure 1a shows different phases of liquid crystals that are classified on the basis of molecular ordering. In the Nematic phase, the long axes of mesogens are roughly parallel, while they are randomly distributed in different locations. The average of the molecules' directions indicates the direction of the LC molecules that are grouped together with similar alignment. This molecular direction is also known as the "director". Mesogens in the Smectice phase are organized into layers, having the same orientation within a given layer (slightly tilted at Smectic C phase). In the Chiral phase,

molecules twist with respect to each other with a constant pitch. LC polymeric materials may possess one or more than one of these phases at different temperatures. At high temperatures, LC polymeric materials are in the isotropic phase, in which mesogens align randomly. Multiple forms of LC polymeric materials can be synthesized through the attachment of the mesogens from the side (side-chain) or ends (main-chain) to polymeric backbones. They are generally categorized into liquid-crystal polymer networks (LCNs), and liquid-crystal elastomers (LCEs), based on the crosslinking density and thermomechanical properties (Figure 1b). LCNs are highly crosslinked (glassy) and can exhibit actuation with $< 5\%$ strain. LCEs on the other hand, have lower crosslinking density. They are more flexible and are able to demonstrate large deformations such as 75% macroscopic strain [8, 9]. When LC monomers are polymerized in a non-reactive low molar mass LCs (nematic solvent), they can form LC gels, also known as nematic gel and swollen nematic elastomer [10, 11]. The presence of the nematic solvent in the mixture softens the material while maintaining the liquid crystallinity features. As a result, the nematic gels can exhibit a fast response to electric [12, 13] and magnetic field [14].

LC polymeric material actuation can be induced using a range of stimuli, including heat, light and solvent [8, 16]. Therefore, the untethered smart structures can be activated remotely using say, ambient energy, without being encumbered by on-board power sources (e.g. batteries). Light is a particularly attractive energy source for driving mechanical adaptation, where it can selectively address actuation with spatiotemporal selectivity at length-scales ranging from the micro to the macroscopic scales. During the phase transition process from Nematic to isotropic at elevated temperatures, anisotropic shrinkage occurs. Due to the lower molecular order in the isotropic phase, the material shrinks in the direction parallel to the directors, and expands in the perpendicular (Figure 1c). Materials can reverse to their initial shape by lowering temperature to the Nematic phase temperature. Therefore, LC polymeric materials can demonstrate a reversible and repeatable contraction in response to heat [17, 18]. Blueprinting spatially heterogeneous molecular patterns to direct the large work potential is a compelling feature of the LC polymeric materials [8]. This allows for their utilization in actuators across length-scales ranging from the micrometer- to the macroscopic-scale [19, 20, 21]. Furthermore, exploiting the competition between bending/stretching in

slender objects allows for eliciting the rare combination of high-force/large-displacement actuation from hitherto small form-factor actuators [21]. Figure 2 shows different actuation modes of a thin film based on its molecular orientation.

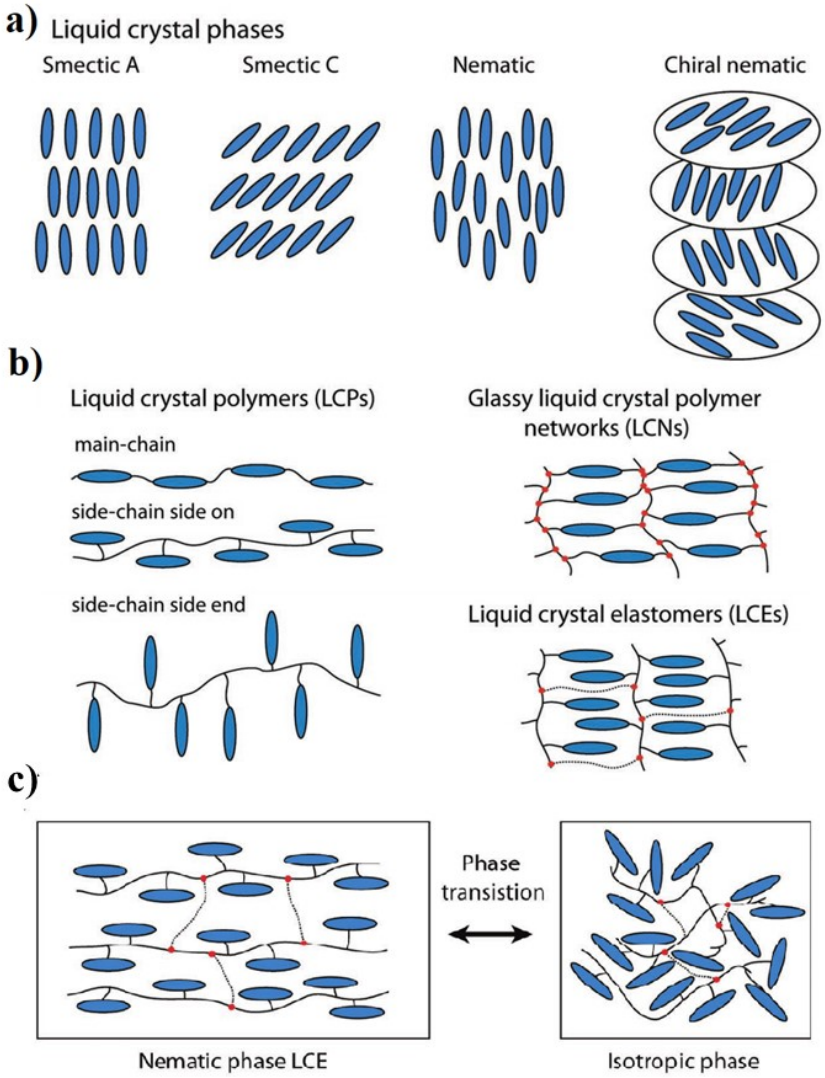

Figure 1: a) Different phases of liquid crystal material b) Different forms of liquid crystal polymeric material based on the mesogen/backbone attachment and crosslinking density c) Nematic to isotropic phase transition and macroscopic deformation of liquid crystal elastomers. Reprinted from [15], with permission from John Wiley and Sons.

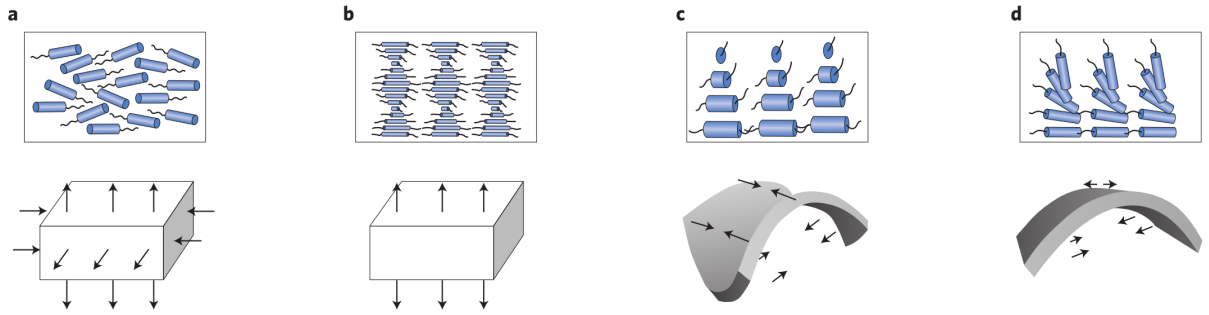

Figure 2: Different molecular alignment in a thin film and the shape changing behavior in response to decreasing the molecular order a) Planar, uniaxial or monodomain (MD) alignment b) Cholesteric alignment c) Twisted nematic alignment d) Splay alignment. Reprinted from [8], with permission from Springer Nature.

Doping the mixture with azobenzene-functionalized crosslinker endows light-responsive actuation due to its ability to performs trans-cis isomerization in response to UV light. Through this transition, the order parameter decreases, leading to macroscopic deformation. Figure 3 shows this mechanism for a flat film with uniaxial molecular alignment. When this sample is irradiated from the top, it bends towards the light due to the the light absorption gradient through the thickness. It can relax to its initial shape as a result of visible light exposure (cis-trans photoisomerization) [22, 23].

Blueprinting molecular patterns has often relied on liquid crystalline (LC) self-assembly of the monomers, which is frozen-in by crosslinking to create the LCN or LCE, often via photopolymerization. Utilizing command surfaces, which have themselves been patterned mechanically, optically or topographically, an array of LCN or LCE director patterns can be generated [8]. Utilization of anisotropic magnetic fields to drive alignment has been resulted in 2 [24] or 2.5D [25] geometries polymerized in molds, although the ability to build 3D free-forms with arbitrarily voxelated LC ordering remains elusive. Harkening back to Finkelman's method for driving alignment via mechanical stretching followed by crosslinking [6], extrusion-based methods have been pursued for the additive fabrication of LCE [26, 27,

28, 29, 30, 31]. Shear imposed on oligomeric inks during extrusion orients the nematic director along the print direction, which is optically crosslinked, soon after the deposition. The raster pattern, which is defined during the build sequence determines the director field during fabrication of macroscopic geometries.

Exploiting the full potential of LC polymeric materials in adaptive structures and mechanisms requires an ability to define the molecular orientation, voxel-by-voxel during the fabrication of a 3D free-form. Doing so, holds the key to encoding arbitrary transformations of three-dimensional geometries along with predefined target metrics [32], which is defined for each voxel. This unlocks a pathway for designing transformable 3D geometries, including complex active kinematic and mechanical logic units, biomimicking actuators and harnessing magnified actuation profiles in soft robotics. Current fabrication approaches constrain the ability to access this 3D design space. The command surface-based methods are intrinsically limited to flat geometries (typically films $< 100\mu m$), necessitating lamination-based assembly for scaling the responsiveness [33]. Using a magnetic field, however influences the alignment within the bulk of the nematogenic monomer, where the selective polymerization can freeze the alignment, as desired. This can simultaneously offer scalability of the fabrication from the micro to the macro-scale, while preserving the spatial resolution of the individual voxels. Thus, we are able to decouple the endowment of molecular alignment (defined by the field

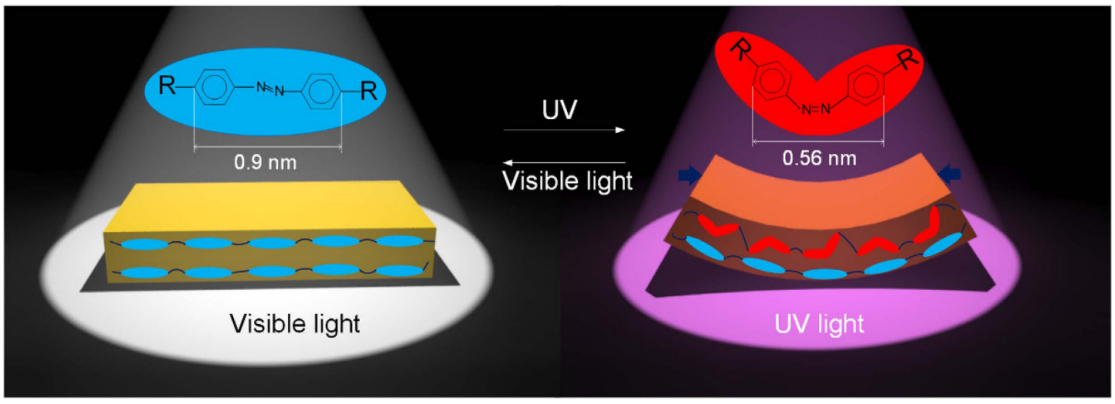

Figure 3: Mechanism of azobenzene isomerization in response to light. Reprinted from [23].

orientation) from the material build path (defined by the selective photopolymerization). As a result, the molecular orientation that was previously constrained by the geometry and the surface patterning or command layers, can now be directly encoded. Designing geometries from responsive materials allows for exploiting mechanical non-linearities. These include snap-through instabilities [34], supercoiling phenomena [35] and related torsional instabilities [36], buckling of plates [37]. This opens the door for realizing ms-scale actuation profiles in soft-actuators, while simultaneously eliciting multi-axial actuation. This framework also allows for arbitrary modulation of the composition of the material from one layer to another. Functional gradations become possible to integrate multi-responsiveness in a facile manner to create response profiles, which were hitherto inaccessible. Note, that magnetic fields are more effective than electric fields for reorienting the directors. It has been shown that 1T has a greater orienting power than 100V/mm [38], which makes it a practical approach for orienting director patterns in macroscopic samples.

This study begins by discussing the interaction of LC molecules with the external magnetic field, followed by reviewing the magnetic-induced alignment of LC polymeric materials and the latest developments in the field of 3D printing LCEs. After addressing the limitations of previous research, the scientific hypotheses are stated in the third chapter. Next, the materials synthesize method, fabrication system and characterization methods are reported. The fifth chapter reports the magnetic field-induced alignment of LCN materials and further proposes a novel platform to pattern material response voxel by voxel in 3D freeforms. In the final chapter, an optimal LCE composition is identified after studying the evolution of molecular orientation as a function of the magnetic field and characterizing the thermomechanical properties. Based on these results, a novel soft robotic application is presented and discussed in the last section.

2.0 Literature Review

This chapter first gives a brief overview of theories regarding the magnetic field-induced orientation of LCs. Next, applications of this method for different LC polymeric materials are reviewed. Finally, recent advances in the field that demonstrated 3D printing of LCEs are discussed.

2.1 Static and Dynamic Theories of Liquid Crystals Distortion due to Magnetic Field

As previously mentioned, one method to control LC molecular orientation is applying an external magnetic field. First, it is necessary to clarify how mesogens interact with an external magnetic field. Organic molecules, aromatic rings in particular, mostly possess diamagnetic properties. Benzene rings, for instance, behave like coils. A magnetic field perpendicular to the molecule's long axis can cause an inner molecular current. This current tends to oppose the magnetic flux. Therefore, diamagnetic mesogens orient parallel to the magnetic field to obtain the lowest energy level. Despite the fact that this energy difference is quite small for a single molecule, nematic LCs with a sufficient number of low viscosity molecules can obtain a large enough coupling energy to overcome the thermal agitation and impose magnetic alignment along the field [39, 40].

In the case of LC material within a voxel, there is always a competition between the external magnetic field orienting effect and the anchoring effect of the walls and the voxel surfaces. To study this, let us first consider a nematic LCE that fills a gap with a thickness of d. Due to the strong surface anchoring effect, mesogens tend to align parallel to the x-axis (Figure 4a). Once an external magnetic field (H) is applied along the y-axis, the magnetic torque tries to align them parallel to the y-axis due to the diamagnetic property of the mesogens. For a small H, mesogens can stay undisturbed, maintaining the uniaxial alignment parallel to the easy axis of wall (x-axis). After increasing the magnetic field more than a

certain threshold, distortions in the form of twist can be found in the molecular orientation. This phase transition was studied and reported by Freedricksz [41]. The magnetic anisotropy can be derived from the difference between diamagnetic susceptibility per volume parallel and perpendicular to the molecular axis.

$$\chi_a = \chi_{\parallel} - \chi_{\perp} \tag{2.1}$$

In this configuration, the vector representing the molecular axis is $n = (cos\theta, sin\theta, 0)$, where θ is the rotation away from the x-axis (Figure 4a). Frank free energy in presence of the external magnetic field can be rewritten as following [42]:

$$F = \frac{1}{2}K_{11}(\nabla.n)^2 + \frac{1}{2}K_{22}(n.(\nabla \times n))^2 + \frac{1}{2}K_{33}(n \times (\nabla \times n))^2 - \frac{1}{2}\chi_a(n.H)^2 \tag{2.2}$$

K_{11}, K_{22} and K_{33} are Frank elastic constant. Minimizing this with respect to z results in the Euler-Lagrange equation:

$$\frac{d}{dz}\left[K_{22}(\frac{d\theta}{dz})^2 + n))^2 + \chi_a H^2 sin^2\theta\right] = 0 \tag{2.3}$$

Inserting the corresponding boundary conditions:
$\theta = 0$ at $z = 0$
$\frac{d\theta}{dz} = 0$ at $z = \frac{d}{2}$
Due to the symmetry we have $\theta(z) = \theta(d - z)$. Thus, the following can be obtained on the threshold of: distortion

$$\chi_a H^2 = K_{22}(\frac{\pi}{d})^2 \tag{2.4}$$

Therefore, the critical field can be computed:

$$H_C = \frac{\pi}{d}(\frac{K_{22}}{\chi_a})^{1/2} \tag{2.5}$$

When $H \gg H_c$, the director orientation is mostly controlled by the magnetic field. For the case of walls with weak anchoring effects, the total free energy 2.2 needs to be modified by adding the surface term [39].

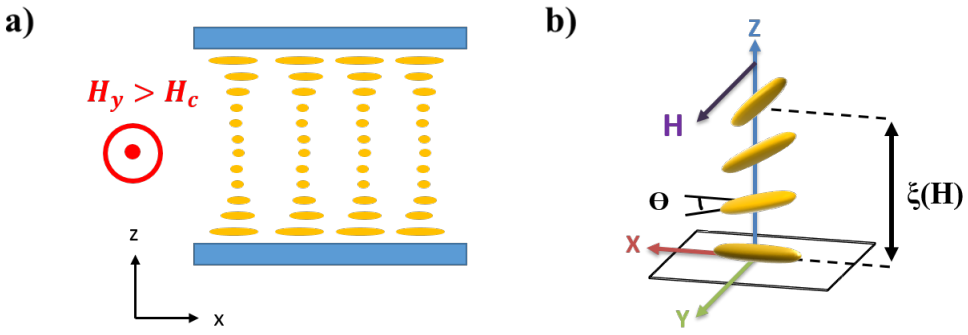

Figure 4: a) Mesogens twist in response to an external magnetic field above a certain threshold ($H > H_C$). This is referred to as the Freedericksz transition b) Transition region close to a surface. Thickness of this transition $\xi(H)$ is called magnetic coherence length. The schematic is inspired by work in Ref. [39].

Let us now consider a similar case but for a semi-infinite volume of LC material. The xy plane at z=0 imposes an alignment along the x-axis, and the applied magnetic field is along the y-axis (Figure 4b). In this case, the competing effects can be studied from the equilibrium of torques point of view. Magnetic torque per volume Γ_M can be derived from the following (M is magnetization):

$$\Gamma_M = M \times H = \chi_a (n.H) n \times H = \chi_a H^2 sin\theta cos\theta \tag{2.6}$$

Surface torque per volume:

$$\Gamma_S = K_{22} \frac{d^2\theta}{dz^2} \tag{2.7}$$

If we define ξ as the follow

$$\xi = \frac{1}{H} \sqrt{\frac{K_{22}}{\chi_a}} \tag{2.8}$$

Then we can write the equilibrium condition:

$$\xi^2 \frac{d^2\theta}{dz^2} + sin\theta cos\theta = 0 \tag{2.9}$$

The boundary conditions:

$\theta = \frac{\pi}{2}$ and $\frac{d\theta}{dz} = 0$ as $z \to \infty$

The integration of 2.9 gives us:

$$tan(\frac{\pi}{4} - \frac{\theta}{2}) = exp(\frac{-z}{\xi}) \tag{2.10}$$

Based on this, ξ represents the thickness of transition (Figure 4b). De Gennes [39] called ξ the "magnetic coherence length". For most of the LCs, the magnetic coherence length is in the scale of few microns, assuming the magnetic flux density to be in the order of 0.1-1 Tesla. Thus, for thick samples ($d \gg \xi$), ξ is negligible and material alignment is mostly controlled by the magnetic field.

The critical field measurement can be a simple and effective method for estimation of Frank elastic constants [43, 44, 45]. Once the magnetic anisotropy χ_a is measured separately [46], the elastic constant can be calculated by using the equation 6.1. The transition can be detected through observation of a sudden change in the intensity of the linearly polarized transmitted light. However, it is difficult to capture the threshold of the twisting deformation (Figure 4a) because the polarization of the light is rotated back to the same initial angle close to the wall [44]. Exposing the light to the sample at an appropriate angle can make it possible to capture the twist deformation threshold [42]. Other methods that can capture the change in anisotropy such as dielectric constant and thermal conductivity measurements can be applied as well [39].

The Freedericksz effect can be further studied from the dynamic behavior point of view. For the configuration shown in Figure 4a, the equation of motion can be obtained as the following [42]

$$K_{22}\frac{\partial^2\theta}{\partial z^2} + \chi_a H^2 sin\theta cos\theta + \lambda_1\frac{\partial\theta}{\partial t} = 0 \tag{2.11}$$

Where λ_1 is the twist viscosity

$$\lambda_1 = \mu_2 - \mu_3 \tag{2.12}$$

μ_2 and μ_3 are coefficients of viscosity (Leslie coefficients). Once the magnetic field is turned on, mesogens twist from $\theta = 0$ to $\theta = \theta_{max}$ with a time constant $\tau(H)$ [42, 47].

$$\tau^{-1}(H) = (\frac{\chi_a}{\lambda_1})(H_c^2 - H^2) \tag{2.13}$$

If the magnetic field is switched off, equation 2.11 would be modified to

$$K_{22}\frac{\partial^2\theta}{\partial z^2} + \lambda_1\frac{\partial\theta}{\partial t} = 0 \tag{2.14}$$

And the decay rate would be:

$$\tau^{-1}(0) = (\frac{K_{22}}{\lambda_1})(\frac{\pi^2}{d^2}) \tag{2.15}$$

2.2 Magnetic Induced Pattering of Main-Chain Liquid Crystal Networks and Elastomers

Thus far, the static and dynamic theories regarding the deformation of LC molecules in the presence of a magnetic field were discussed. The following reviews the previous studies that have explored the magnetic-induced patterning of LC polymeric materials.

The first detailed work on the orientation kinetics of LCN mesogens in the presence of an external magnetic field was reported by Moore and S. I. Stupp [48]. The main-chain LC monomers were polymerized in the presence of a high-intensity magnetic field (4.7 T). Results from the X-ray diffraction experiments confirmed the uniaxial alignment for magnetically aligned LCNs while polydomain orientation was observed in the absence of the magnetic field. Therefore, the molecular orientation was preserved after the polymerization. To better understand the mechanism, Anwer and Windle [49] explored the orientation process as a function of the magnetic field intensity and the molecular weight. The second-order spherical harmonic coefficient of the monomer melt was measured through the X-ray diffraction experiment to determine the preferred orientation. It was shown that applying stronger magnetic field resulted in both higher order parameter and faster uniaxial orientation. It was found that the higher molecular weight monomers required higher magnetic fields to obtain the same order parameter and rate of orientation. However, the utilization of a sufficiently high magnetic field (1-1.5 T) can eliminate the dependence on the molecular weight. While in these works strong and bulky superconducting magnets (> 1 T) were required for imposing molecular alignment, Shin et al. [50] demonstrated the preparation of magnetically aligned LCNs by using NdFeB permanent magnets (~ 0.5 T). They used commercially

available diacrylate monomer RM257and PETMP thiol-crosslinker (5 $mol\%$). Due to the small portion of the crosslinker, the crosslinking density was high enough to be considered a glassy material. In consistence with previous studies [51, 52], it was reported that increasing the crosslinker concentration resulted in reduction of the order parameter. For 20 $mol\%$ crosslinker, polydomain molecular alignment was detected based on the glancing incident wide-angle X-ray scattering (GIWAXS) experiment result. Another important finding was the reorientation of the polymerized LCNs by applying magnetic field. However, no detailed investigation regarding this mechanism was reported.

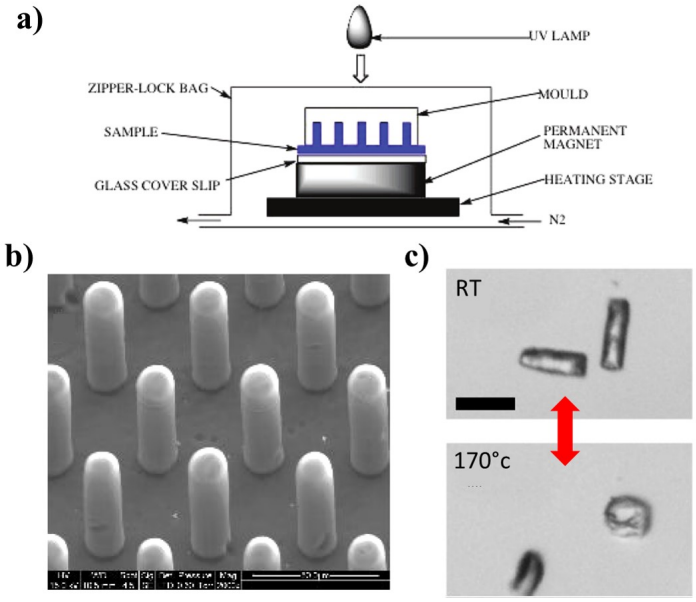

Figure 5: a) Schematic of the experimental setup for the fabrication of main-chain LCEs b) SEM image of the micropillar structure c) Reversible thermal actuation of two pillars that were cut from the structure (scale bar = $100\mu m$). Reprinted with permission from [53], Copyright 2009 American Chemical Society.

In a study conducted by Keller and co-workers [53], magnetically aligned main-chain LCEs were developed. The LCEs were synthesized through the photopolymerization of thiol-ene monomers [54]. An advantage of the magnetic field orientation technique is its ability to align samples with arbitrary geometries. A poly(dimethylsiloxane) PDMS mold with arrays of microholes was filled with the mixture. Vertical alignment was induced to the material at

the nematic phase temperature by using a permanent magnet ($\sim$ 1 T). Then, the material was polymerized through UV exposure in the presence of the magnetic field (Figure 5a). Once the temperature was decreased to room temperature, the PDMS mold was peeled off. Figure 5b shows the final LCE microstructure. While small quantity of thiol (5 $mol\%$) was used in the mixture, the pillars could demonstrate reversible high-stain contraction in response to heating (Figure 5c). There was no measurement of crosslinking density to characterize the elasticity. Besides, the molecular orientation was not confirmed with linear birefringence measurements or X-ray scattering experiments. In their recent works, Ni et al. applied a similar method to fabricate large-size and more sophisticated LCE structures such as honeycomb-shaped, rectangle frame, grid pattern, cubic frame, and spring shapes aligned by 0.5 T magnetic field [55, 56]. The molecular orientation was confirmed by WAXS technique. However, the sample was prepared through thiol-ene/acrylate photopolymerization with high concentration of LC monomer capable of thiol-ene reaction only. As can be seen from the results, the quality of the fabricated structures are relatively low. This is caused by low gel fraction of the structue due to high molar ratio of the LC monomer with -ene group [57]. Furthermore, the single-step thiol-ene reaction requires long time to obtain fully crosslinked polymers. In these works samples were polymerized after an hour of UV exposure [55, 56]. This makes the material incompatible with 3D printing methods.

2.3 Magnetic Induced Pattering of Side-Chain Liquid Crystal Elastomers

Applying magnetic field for fabrication of side-chain LCEs was first reported by Roberts et al. [58]. Similar to the method described for main-chains, the monomers were aligned parallel to the magnetic field and were subsequently crosslinked to fix the orientation and form the LCE film. Keller and co-workers developed a new side-chain LCE [17] and adopted the replica molding method for fabrication of the micropillars which were capable of performing $30 - 40\%$ strain actuation [59]. This method was further exploited for switchable adhesion [60] and wetting [61] behaviors. Since the magnetic field interacts with volume rather than surface, magnetic alignment is not limited by the film thickness. Schuhladen et al. [24] took

advantage of this by making a thick, tunable side-chain LCE [62] iris inspired by human eye muscles. As shown in Figure 6d, two-row of 8 permanent magnets were placed around the sample radially, which generates 0.1T field. This magnetic field induces a radial directors orientation. Applying voltage to the stretchable heater wires that are embedded in the LCE results in a reversible radial actuation, as shown in Figure 6b.

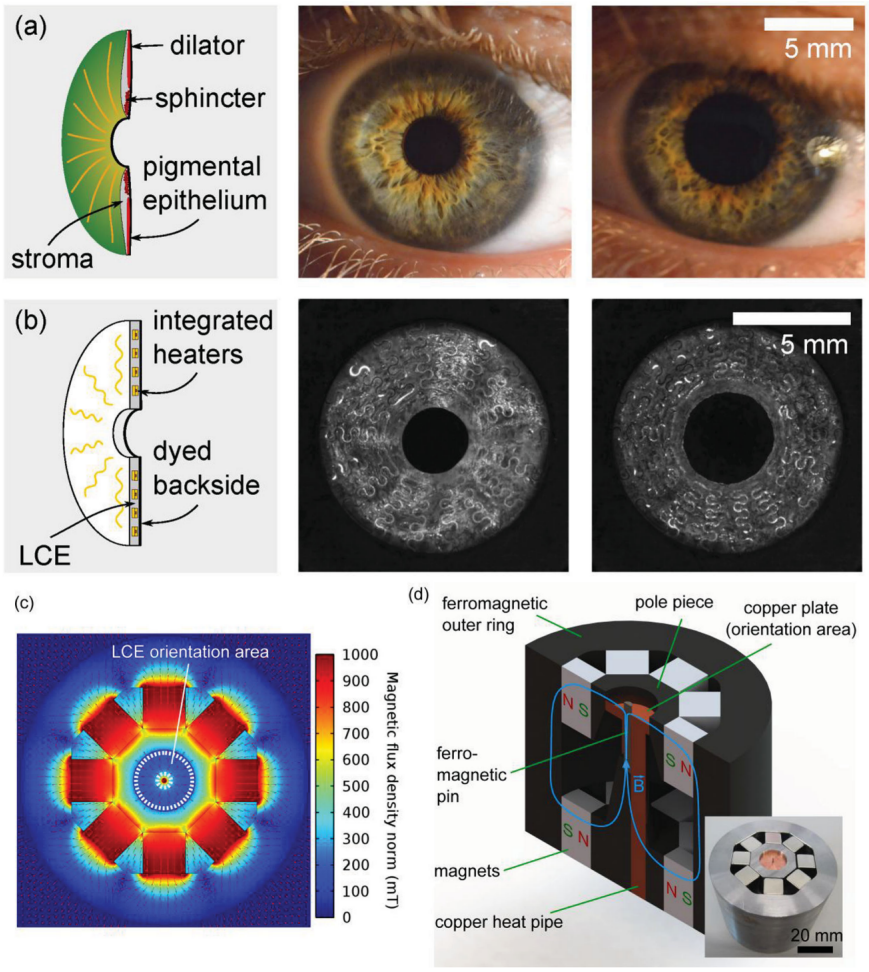

Figure 6: a) Human iris schematic, b) Schematic of LCE tunable iris and its reversible radial actuation by applying voltage to the heater, c) Magnetic field simulation, d) Experimental setup for fabrication of radially ordered LCE. Reprinted from [24], with permission from John Wiley and Sons.

In a recent study, Aizenberg's group employed the same side-chain LCE [62] and the replica molding method to make microstructures that can demonstrate more complex deformations such as shearing, buckling [25] and twisting [63]. Moreover, an array of light-responsive micropillars was developed by introducing the azobenzene dye to the composition. However, the effect of the crosslinker and the orientation mechanism remains unclear. Furthermore, the side-chain LCEs are not able to demonstrate high-stress actuation which limits their application.

2.4 3D Printing Liquid Crystal Elastomers

3D printing or additive manufacturing is a fabrication method that uses the 3D CAD model of a structure to produce an object layer-by-layer. It can generally make each layer by one of the following methods: photopolymerization of the resin, sintering or melting the powder by a laser source, gluing the powder, or depositing the material in form of heated filaments or droplets. The main advantage of 3D printing is fabrication of complex 3D structures. While most researchers have focused on making LCE material in thin films ($< 100\mu m$ thick) or tubes [64], 3D printing has been used recently to fabricate 3D LCE structures. In what follows, 3D printing methods applied by researchers to make LCE structures is presented.

2.4.1 3D Printing Liquid Crystal Elastomers through Material Extrusion

Extrusion-based additive manufacturing (also known as Fused Deposition Modeling) is a powerful fabrication tool that can make complex 3D structures by depositing the material along a path, layer by layer. It has already been used by researchers to print various responsive materials such as hydrogels [4, 65]. This method has been used recently to make LCE structures [26, 27, 28]. Through the printing process, LCE oligomers are extruded at the nematic temperature (Figure 7a). The extrusion process imposes shear stress on the material. Previous studies on electrospinning and fiber drawing [66, 67] have shown that

shear force can be used to induce molecular orientation. At the right temperature and printing speed, this shear force can be sufficient to align the mesogens parallel to the extruding direction. Therefore, the material filaments are aligned uniaxially, parallel to the printing direction (Figure 7b). The material can be polymerized by UV light exposure right after the extrusion or after curing the whole layer in order to fix the alignment.

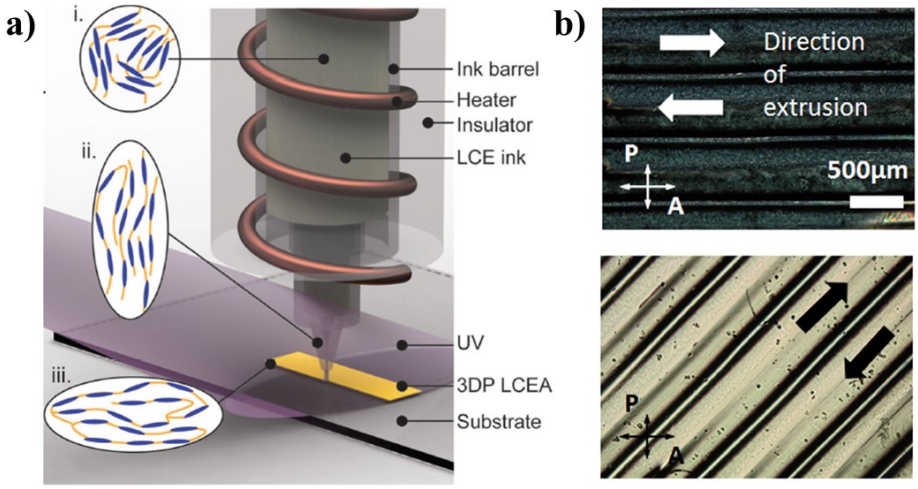

Figure 7: a) Schematic of extruding LCE during the printing process. Reprinted from [27], with permission from John Wiley and Sons. b) POM observation of printed lines at 0° and 45°. Reprinted (adapted) with permission from [26]. Copyright 2017 American Chemical Society.

As explained previously, the orientation can be varied along the printing path. As a result of this, non-uniaxial alignment within the layer can be achieved. A good demonstration of this can be seen in a layer with azimuthal pattern orientation (also known as +1 topological defect). A spiral-like scanning route can result in this pattern. Thermal actuation of this layer of material leads to out-of-plane deformation, morphing into a cone-shaped structure (Figure 8) [28].

The ability to make complex 3D structures is probably the most important advantage of 3D printing LCEs. Figure 9 shows a 3D structure made of both positive and negative Gaussian curvatures with azimuthal alignment. Apparently, this structure cannot be made with other conventional fabrication methods. This structure goes through a reversible, asymmet-

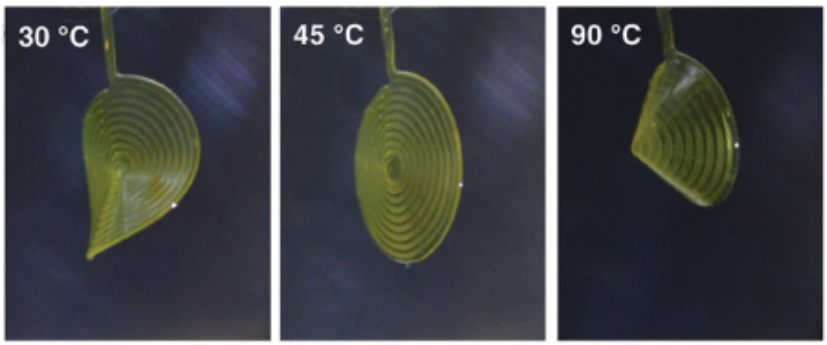

Figure 8: Thermal actuation of a single layer of LCE with spiral-like orientation. Reprinted from [28], with permission from John Wiley and Sons.

ric snap-through shape change in response to heat [26]. While most researchers focused on LCEs with only thermomechanical responsiveness, Ceamanos et al. recently printed monodomain 90 μm thick LCE film containing anazobenzene moiety, capable of performing linear photoactuation [68].

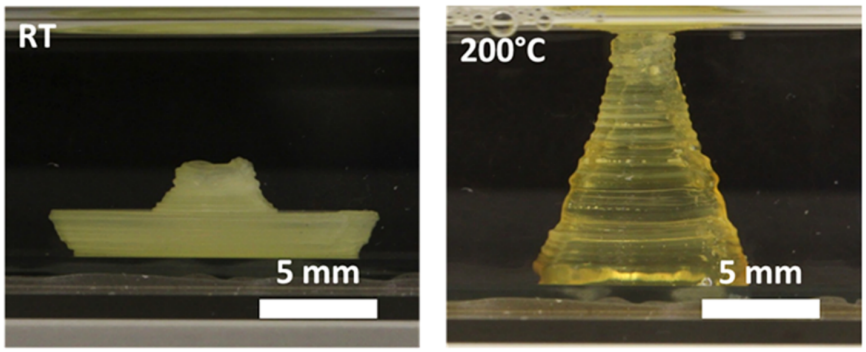

Figure 9: Thermal actuation of the 3D printed structure containing positive and negative Gaussian curvatures. Reprinted (adapted) with permission from [26]. Copyright 2017 American Chemical Society.

Ware and co-workers have proposed printable thiol-ene compositions that can be actuated at lower temperatures. They also demonstrated multimaterial printing of these compositions in a single structure [30]. Lewis and co-workers have further exploited this in sequential

thermal actuation of a self-propelling robot [69]. In another work their group embedded liquid metal (LM) in LCE structures for the purpose of electrothermal actuations. By extruding the LM in the core of the coaxial nozzle, it was encapsulated by the surrounding LCE [70]. Ambulo et al., on the other hand, developed a composite LM\LCE ink and further illustrated the capability of their method through printing multimaterial structures equipped with both electrothermal and photothermal responsiveness [71]. The layer thickness and filament diameter can be varied by changing process parameters, such as printing speed, viscosity, scanning speed and nozzle diameter. However, it is important to bear in mind that these parameters may affect the order parameter as well. Very recently, researchers have utilized printing parameters [72, 73, 74] and the temperature gradient through the thickness [75] for programming the shape-changing behavior.

Deposition-based methods can generate arbitrary geometries, but they cannot decouple molecular patterning from the build sequence [26, 27, 28, 29, 30, 31]. Contrast deposition-based methods against an approach, where the molecular orientation can be independently defined with say, 1° resolution per $\sim 8\mu m$ element. For a 1mm segment, the latter method offers a design-space, which is larger by a factor of $\sim 10^{40}$ in comparison to the deposition-based method. Assuming, 180° is available with 1° resolution per $8\mu m$ length, the total number of design permutations is $180^{(1000/8)} \sim 10^{40}$. For a $1mm^3$ volume, the design space is larger by a googol.

2.4.2 Direct Laser Writing of Liquid Crystal Elastomers

Another additive manufacturing method that has been used for making 3D LCE structures is Direct Laser Writing (DLW) [76]. DLW applies the two-photon absorption method to polymerize a nanoscale voxel of a UV-curable material (Figure 10).

In order to 3D print LCE through DLW, a cell filled with molten LC monomers is placed on the workstation at the nematic temperature. The molecular orientation is programmed by the cell's inner surfaces. One layer can be fabricated by moving the laser focal spot in the plane. This process can be repeated for next layers by changing the depth of focal spot. The two-photon polymerization (2PP) of material enables printing of complex 3D structures

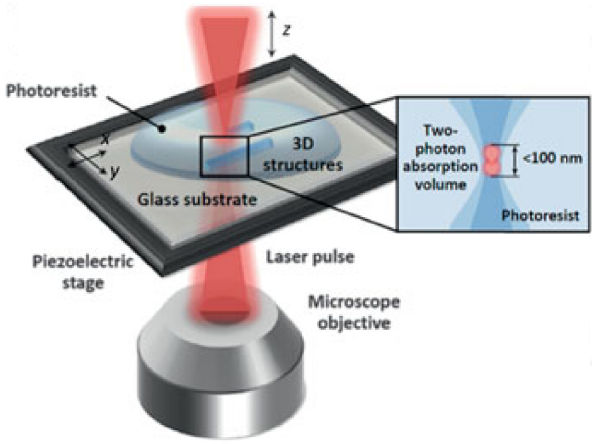

Figure 10: Schematic of direct laser writing (DLW) or 2-photon polymerization (2PP) process. Reprinted from [77], with permission from John Wiley and Sons.

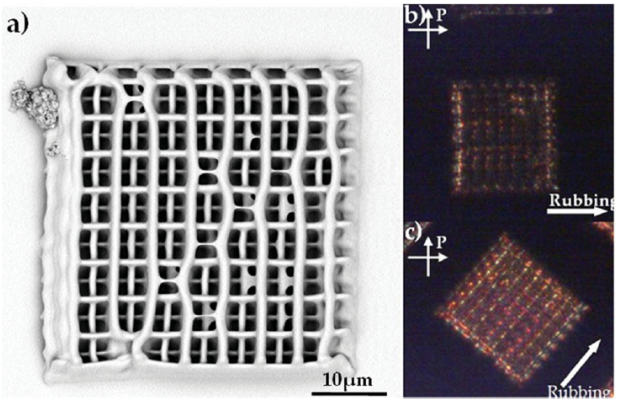

Figure 11: 3D printed LCE woodpiles structure a) SEM image b) POM image of the structure at 0° and c) 45°. Reprinted from [78], with permission from John Wiley and Sons.

with sub-micrometer resolution. Figure 11 demonstrates this capability in a $40\mu m \times 40\mu m$ LCE woodpile structure with uniaxial molecular alignment [78]. The LCE woodpile is a quite complex 3D structure with overhanging features and can have applications in both photonics and microrobotics.

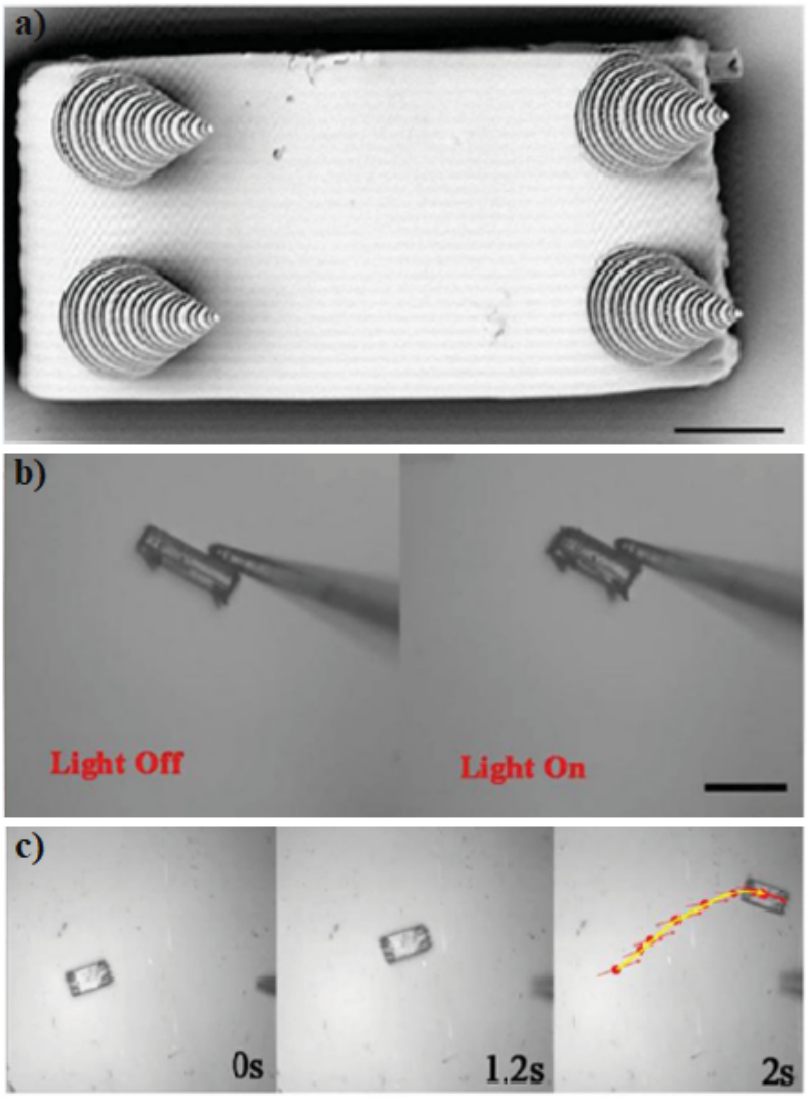

Figure 12: a) Bottom view of microwalker imaged by SEM (scale bar = $10\mu m$) b) Reversible contraction of microwalker in response to the light (scale bar = $50\mu m$) c) Directional walking on a grooved surface in response to laser excitation.Reprinted from [79], with permission from John Wiley and Sons.

Microscopic walker (Figure 12) is a good example that illustrates the possible application of 3D printed LCEs in microrobotics [79]. The walker contracts in response to light due to uniaxial molecular alignment parallel to its longitude (Figure 12b). The actuation energy

is high enough to overcome adhesion and move one step forward (Figure 12c). The 45° tilt makes the adhesion asymmetrical, and prevents sliding or any backward movements. However, it is common that the front or back legs stick to the surface after a few steps due to fabrication defects. Recently White and co-workers reported the development of composite microactuators by infilling the pores of the DLW printed epoxide-based LCEs with acrylate-based LCEs [80].

The similar fabrication method was applied by Guo et al. to generate LCE freeforms. The alignment complexity was enhanced through fabricating microchannels on the walls [81] to induce arbitrary in-plane molecular orientations. While freeforms can be fabricated through this process, they lack the ability to voxelate the stimuli response with indexable, spatial selectivity within the structure. In their next work, they first fabricated LCE cubes with predefined orientations through the same method, then they manually assembled them as building blocks to create the final structure [82]. In addition to the requirement for the manual work and the time consuming and inaccurate nature of the assembling procedure, this method also restricts the geometrical complexity of the structure. Inspired by our first published paper in this work, researchers demonstrated real voxel-by-voxel encoding alignment through combination of an external electric field with DLW photopolymerization technique [83, 84]. While this method is desirable at this small scale, the electric field becomes much more inefficient than magnetic field at larger scales.

2.4.3 Digital Light Processing Printing of Liquid Crystal Elastomers

In addition to our work, multiple groups recently tried to utilize the selective photopolymerization through Digital Light Processing (DLP) to print LCEs [85]. However, the alignment techniques that were applied including shearing [86], anisotropic swelling [87], and mechanical loading [88] they all have intrinsic limitations that lack the ability to voxelate the stimuli response with indexable, spatial selectivity within the structure.

3.0 Problem Statement

Despite their unique features, LC polymeric materials have not been widely applied in the development of new technologies. The ability to pattern the molecular alignment, voxel-by-voxel, in arbitrary freeforms and the potential for composite modulation are the key enablers for bridging the gap between these materials and practical applications such as soft robots. Encoding the orientation with magnetic alignment is the best candidate method for achieving this. Unlike other methods, such as surface-induced alignment, the magnetically-assisted alignment technique is capable of encoding each voxel independently and is insensitive to the sample geometry. Although previous research has explored programming the molecular alignment in glassy LCNs and side-chain LCEs using low-intensity magnetic fields ($< 0.5T$), few prior studies have investigated programming main-chain LCEs. Main-chain LCEs are highly preferred over glassy LCNs and side-chain LCEs for real applications due to their capability to generate large strains ($> 10\%$) and actuation stresses (100's of kPa). This work aims to study the mechanism of magnetic alignment, propose and develop a new LCE composition that can be aligned by low-intensity magnetic fields, and further explore the viability of this composition for new applications in soft robotics and smart meta structures. This work is guided by three hypotheses:

1. Achiral LC monomers within a microscale voxel self-assemble in the nematic phase, orienting along an "easy axis" dictated by the anchoring from the voxel's surfaces and the external magnetic field direction. The molecular alignment can be preserved by crosslinking to create a main-chain liquid crystalline network. A temperature window exists below the phase transition temperature (T_{NI}) for orienting and polymerizing the mesogenic monomers without requiring any temperature cycling. The evolution of the magnetically-assisted generation of nematic ordering is expected to follow the nucleation growth mechanism with a growth rate depending on the interplay of the anisotropy of magnetic susceptibility, the intrinsic rotational viscosity, and the magnetic field intensity.
2. Low-intensity magnetic fields (< 0.5 T) are not sufficient to encode the molecular orientation of LCEs that are synthesized through the Michael-addition reaction. Compared

with LC monomers, LC oligomers require stronger magnetic field to impose orientation due to the higher molecular weight, elastic constant and twist viscosity. Furthermore, introducing significant quantities of thiol chain extenders to the LC monomer generally decreases the magnetic anisotropy. On the other hand, diluting this mixture with a nonreactive nematic solvent increases the magnetic anisotropy. As a result, nematic gels patterned with an external magnetic field can be produced through the polymerization of these mixtures with frozen-in molecular orientation.

3. The utilization of a chain transfer agent (CTA) during the synthesis process allows for tuning the network properties and obtaining the magnetic alignment without the requirement for the oligomerization step. Therefore, the magnitude of the scalar order parameter and the mechanical responsiveness of the 3D printed polymer to thermal and photonic stimuli can be controlled by varying the relative concentrations of the mesogens, CTA, and thiol chain-extender.

The following research tasks were undertaken to test these hypotheses:

1. Derive the $\frac{K_{22}}{\chi_a}$ ratio (twist elastic constant over magnetic susceptibility) of the monomer melt by measuring the critical magnetic field (H_C). This can be done by observation of the birefringence variation as a function of magnetic field intensity. As discussed in section 2.1, H_C can be identified when an abrupt change of birefringence occurs. Measurement of the H_C can help us to better understand the orientation kinetics of the monomer. This information is particularly helpful for optimizing process parameters such as magnetic field intensity, the orienting temperature, and the orientation rate. As explained in section 2.1, if the surface anchoring is not strong enough, the surface term needs to be considered for the calculation of the critical magnetic field (H_C) and the magnetic coherence length (ξ). Therefore, it is also required to investigate the effect of weak surface anchoring on ξ to determine the achievable resolution of the voxel that can be programmed independently.
2. Measure $H_C(T)$ for mixtures with thiol chain extenders to understand the effect of mesogen concentration and chain extender structures. Comparing these results and the data from the previous task will help us to better understand the reason for losing

the magnetic-induced alignment of the LCEs that are synthesized through the Michael-addition reaction.

3. Study the effect of the CTA on the order parameter and the photomechanical and thermomechanical response. The critical field for different concentrations of the CTA will be measured similar to Task 1. Two different CTAs are suggested for this study: 1,4-benzenedimethanethiol (BDMT) and Tetrabromomethane (TBM). Once the optimized mixtures are obtained, we compare the thermomechanical properties through the measurement of glass transition temperature (T_g), phase transition temperature (T_{NI}) and thermal actuation strain.
4. Develop the "working curve" and optimize a range of monomer compositions to include photoinitiators, light absorbers, and polymerization inhibitors to modulate the polymerization characteristics, while simultaneously retaining the tailorability of the nematic alignment. Working curve demonstrates the correlation between the polymerization depth and photonic energy dosage for each composition. This is critical to identify the compositions and processing conditions to control the depth to which crosslinking occurs. Depending on the orientation timescale (dwell time), the composition may require thermal inhibitors to avoid unintended thermal polymerization. The presence of the thermal inhibitor can affect the rotational viscosity and the magnetic alignment. Similarly, it has been observed that the azobenzene dye concentration can influence the molecular orientation. Therefore, it is required to repeat Task 1 to optimize the azobenzene dye and the thermal inhibitor concentrations as well as the process parameters.
5. Utilize a custom-built 3D printing platform to fabricate voxelated 3D free-forms, where the principal directions of strains in response to heat and light can be modulated voxel-by-voxel. Characterize the thermomechanical and photomechanical responses as a function of composition and process conditions. The process parameters such as dwell time, exposure time, exposure time, polymerization temperature, and dwell time for each composition are derived from the previous tasks.

4.0 Materials and Methods

The general synthesis, fabrication, and characterization methods are described in this section. More details about specific materials and methods are provided in chapters 5 & 6.

4.1 Material Synthesis Method

RM257 (1,4-bis-[4-(3-acryloyloxypropyloxy)benzoyloxy]-2-methylbenzene) and RM82 (1, 4-Bis-[4-(6-acryloyloxyhexyloxy)benzoyloxy]-2-methylbenzene) are used as mesogenic diacrylate. For the purpose of decreasing crosslinking density and modulating the modulus and responsiveness of the LCE, TBM (Tetrabromomethane, Sigma-Aldrich) as chain transfer agent (CTA) and BDMT (1,4-benzenedimethanethiol, Sigma-Aldrich) chain extender are used (discussed in more details in the next chapters). Another useful component is BHT (2,6-Di-tert-butyl-4-methylphenol, Sigma-Aldrich) which inhibits inadvertent thermal polymerization during the fabrication or characterization procedures. Light-responsiveness is endowed to the material by doping the mixture with azo 6c (4,4′-di(6- (acryloxy)-hexyloxy)azobenzene). Based on the polymerization light wavelength, Iragcure 819 (375 nm peak) or Iragcure 784 (visible light) was added for the purpose of photoinitiation. Cells with $50\mu m$ gap are made by gluing two coverslips, utilizing spacers in between them. The coverslips are generally prepared through sonicating in IPA, followed by plasma cleaning. To impose surface alignment, coverslips are spin-coated with Elvamide (DuPont), baked, and rubbed with a velvet cloth. To minimize surface-induced alignment Polydimethylsiloxane (PDMS, Sylgard 184 Dow Corning 184 Silicone Elastomer) substrate or optically clear Polytetrafluoroethylene (PTFE) silicone films (FEP) are used due to their weak surface anchoring. The melted monomer mixture infiltrates the cell at the isotropic state. Then the cell is cooled down to the nematic phase temperature. After 5-10 min, it is polymerized using UV light exposure.

4.2 High Resolution 3D Magnetic Printer

4.2.1 Fabrication System

A commercially available DLP projector (D912HD, Vivitek), which was modified to remove the UV filters, was purposed for these experiments (Figure 13). The projection resolution was further increased to $\sim 8\mu m$ by applying optical cage systems (Thorlabs). The position of the build plate was controlled in XYZ using three orthogonally mounted motorized translation stage (PT1/M-Z8, Thorlabs). The bottom window was made of a clear acrylic sheet coated with a thin layer of PDMS or FEP film. In order to control the printing temperature, a heating system including a ring disc heater (200W, McMaster), a temperature controller (PXR3, Fuji Electric), two thermocouples (5SRTC-TT-J-30-36, Omega) and a thermometer (HH802U, Omega) was built. Permanent Neodymium magnets were purchased from K&J Magnetics and mounted on a motorized rotation stage (PRM1Z8, Thorlabs) in order to control the direction of the magnetic field.

4.2.2 Printing Method

First, A 3D model of the desired structure was designed using Solidworks (Dassault Systems) and saved in .stl format. Then, the 3D model was sliced into black and white 2D patterns of the cross-section by a slicer software (CreationWorkshops). These patterns were later used to photopolymerize the cross-section at each layer. Within each layer of the structure, regions that have different molecular alignment were placed in different layers in the CAD model in order to produce different patterns after the slicing step. A coverslip (build plate) was spin-coated with Elvamide (DuPont) to achieve sufficient adhesion between the cured material and the coverslip. If needed, it can also be rubbed in the desired directions to impose the alignment on mesogens close to the build plate due to the surface anchoring phenomenon. Once the coverslip was attached to the platform, it was moved to the desired location (build-gap) close to the PDMS (or FEP). The cell was then heated to the desired temperature that falls within the nematic phase range of the monomer. The molten monomer mixture was then introduced into the build-gap to build the subsequent layers. A 0.3 T

magnetic field was introduced by using two Neodymium permanent magnets (grade N52, K&J Magnetics). In order to achieve the programmed orientation induced by magnetic field, a 5-10 min dwell time was required before polymerization. The dwell time provides enough time for the mesogens to rotate completely and align parallel to the magnetic field. Then, the desired 2D pattern was exposed. The exposure period and the intensity were derived from

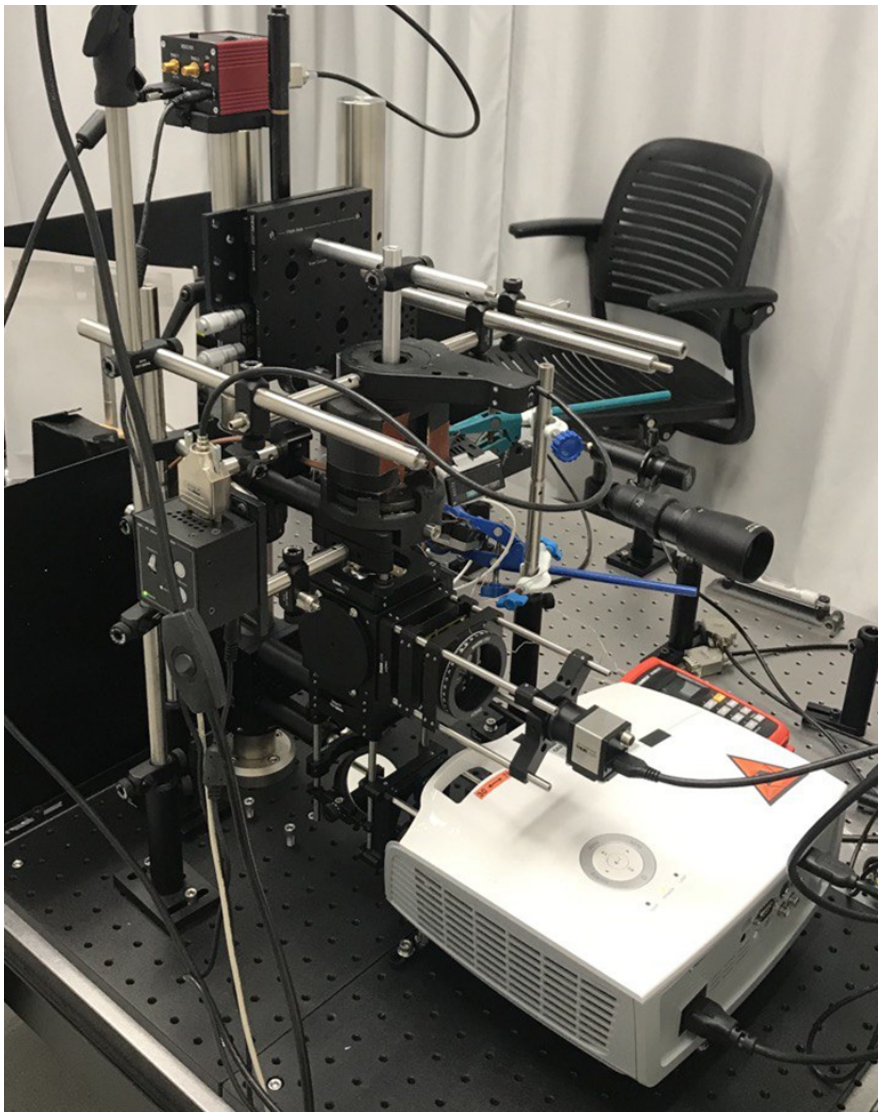

Figure 13: 3D printer setup capable of programming the mesogens orientations voxel-by-voxel.

the working curve (chapters 5 & 6). For light-responsive materials (doped with azobenzene), a 495 nm long-pass filter was used to prevent the photoisomerization and order distortion during the photopolymerization. The printing process continued by lifting the platform, rotating the magnetic field (if required) and exposing 2D patterns repeatedly. Once all the layers were polymerized and the 3D object was completed, the build plate moved up and the printed structure was removed from the printer. For the final development, the sample was immersed in the Propylene glycol monomethyl ether acetate (PGMEA, Sigma-Aldrich) for 20 minutes, followed by sonication in IPA for 5 minutes. Finally, it was dried in a vacuum chamber for 2-3 min. The final product generally required a post-curing process that was executed by exposing $\sim$20 mW/cm^2 UV light (green light for light-responsive materials) for about 30 minutes or heating the sample up to 75 $^{\circ}C$ for 1 hour. As it's demonstrated in the following chapter, this platform is capable of integrating different materials during the printing process. This multimaterial printing procedure is implemented by washing the monomer inside the printer setup and introducing monomer of a different composition. This feature can be exploited for modulating the composition and enables the design and fabrication of complex structures with multifunctionality.

4.2.3 In-situ Observation

The setup was recently modified by adding an imaging system (DCC3260M and M730L5, Thorlabs) for in-situ polarized optical microscopy (Figure 14a). This provides the empowerment to study the change of the molecular order as a function of composition, magnetic field intensity, temperature, and time (Figure 14b) inside the 3D printer.

4.3 Characterization Methods and Devices

4.3.1 Critical Field Measurements

For critical field measurement experiments, cells with 15 μm gaps were made by gluing glasses with indium tin oxide (ITO) coating (06478B-AB, SPI Supplies) and 10 mm $\times$ 10 mm coverslips, utilizing spacers (15μm silica microspheres) between them. After cleaning

the coverslips and glasses through sonication in IPA and plasma cleaning, they were spin-coated with Elvamide (DuPont). After 10 minutes baking at 80°, they were rubbed with a velvet cloth to impose surface alignment. Once the cell was assembled, the melted monomer mixture was added and infiltrated the cell at the isotropic temperature. Then the cell

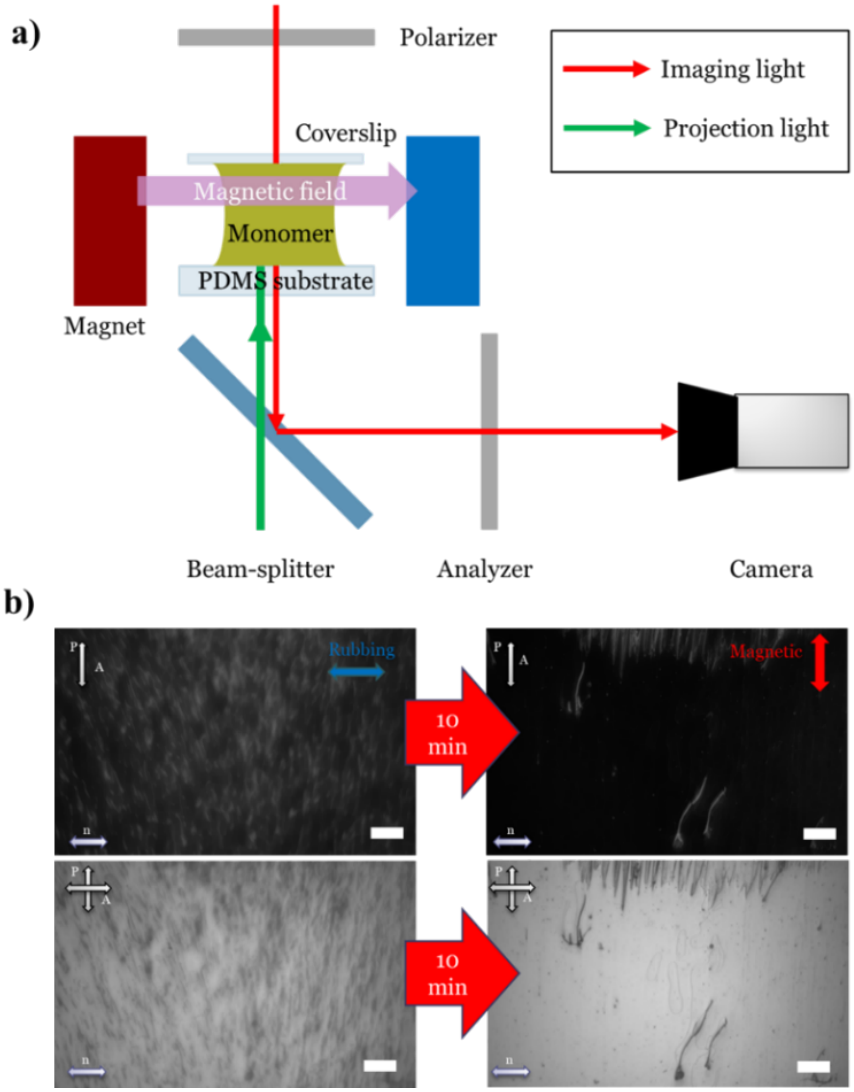

Figure 14: a) Schematic illustration of the printing process and in situ observation b) In situ observation of change in the monomer birefringence over time at $70°C$ under the influence of a magnetic field (scale bars = 1 mm).

was cooled down, the gaps were sealed using epoxy glue, and the wires were connected by applying conductive epoxy or soldering. The uniaxial molecular orientation was checked at nematic phase using crossed polarizers. The sample needs to be perfectly transparent as any defect can affect the measurements of the transmitted light. Next, the cell was mounted between two crossed polarizers, in a way that the molecular alignment (rubbing direction) was vertical. The exposed light from a He-Ne laser (λ = 633 nm, HNL050L, Thorlabs) transmitted through the polarizers, cell, and a Soleil-Babinet Compensator (SBC-VIS, Thorlabs). The transmitted light power was capture by a highly sensitive photodiode power sensor (S120C, Thorlabs). Two permanent neodymium magnets (K&J Magnetics) were mounted on a linear stage (59-337, Edmund Optics) to apply a wide range (20-680 mT in the center) of external magnetic field (perpendicular to the rubbing direction, as depicted in Figure 15) by adjusting their distance to each other. A Teslameter (SDL900, Instrumart) was used to track the magnetic flux density. To control the cell temperature, an Arduino PID controlling system and a self-adhesive thermocouple (SA3-K, Omega) were connected to the cell. The measurements were executed at a certain temperature (nematic phase) rather than going through a N-ISO thermal cycle for each data point.

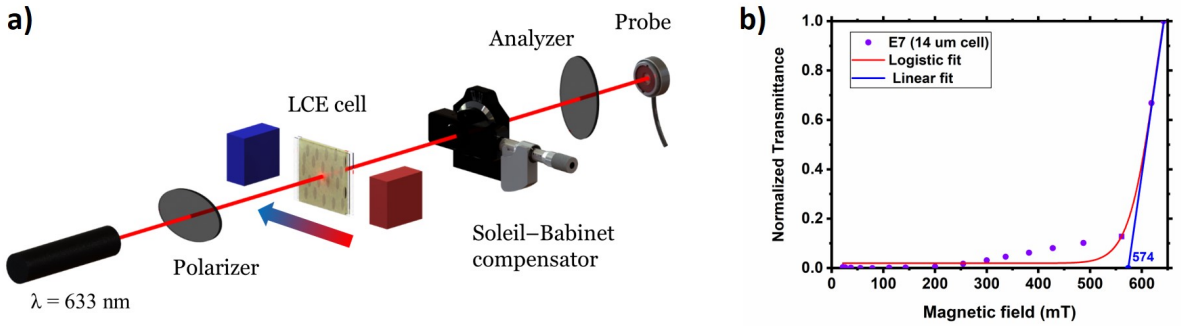

Figure 15: a) Schematic of the critical field measurement setup. b) Measured magnetic flux density–transmittance for E7 monomer at room temperature. The Red line illustrates the logistic fitting curves and the blue line was derived from linear fitting to estimate the magnetic field threshold.

To study the magnetic orientation mechanism and determine the critical field, the intensity of the transmitted light was measured as a function of the magnetic field (magnetic flux density). The kinetic effect was eliminated by executing the measurement after the data was stabilized (generally after 10-20 minutes) at each point. After the threshold, a sudden change could be observed that indicated the change in the molecular alignment (twisting in this case) as the magnetic field started to overcome the surface anchoring effect [89]. Sigmoid functions were used to fit a curvature to the data. Finally, the critical field was estimated by fitting linear. The accuracy of the setup was confirmed by measuring the critical field for E7 material at room temperature (Figure 15b). The result (574 mT for 14μm thick cell) demonstrated good agreement ($\sim$ 1% error) with the reported data in Ref. [89, 46]. Based on the critical field values we were able to calculate the required magnetic field and De Gennes's magnetic coherence length [39] for different composition and surfaces.

4.3.2 Polarized Optical Microscopy

Due to the birefringence property of LC materials, the refractive index depends on the angle between the director and the light polarization. This unique property enables us to study the molecular orientation by using linearly polarized light. Polarized Optical Microscopy (POM) is an optical microscope with a polarizer and an analyzer that can be rotated with respect to each other. Films with uniaxial and twisted nematic alignment can be determined by observation of the transmitted light through crossed and parallel polarizers.

4.3.3 Thermal Properties

The composition thermal properties such as glass transition temperature (T_g) are collected using differential scanning calorimetry (DSC, Perkin Elmer Diamond). The sample heat flow and the reference heat flow are compared as a function of temperature to detect thermal transitions. The nematic-isotropic phase transition temperature (T_{NI}) can also be identified by polarizers.

4.3.4 Mechanical Properties

The viscoelastic behavior of the LCE films can be studied using dynamic mechanical analyzer (DMA, Perkin Elmer 8000). Rectangular samples are clamped to the device and sinusoidal forces applied, capturing the stress and strain as a function of temperature. Important mechanical properties such as storage modulus, loss modulus, and phase angle can be determined from the data.

4.3.5 Shape Change Characterizations

To measure the contractile strain in response to heat stimuli, rectangular pieces were cut and placed on a hotplate with a temperature controller. Silicone oil was added to decrease the friction and a thin coverslip was placed on top of the sample to restrict the the deformation to in-plane shrinkage. Two thermocouples (5SRTC-TT-J-30-36, Omega) and a thermometer (HH802U, Omega) were used to measure the temperature. Images and videos were captured by Aven Mighty Scope 1.3M USB Digital Microscope cameras (20-200x magnification, 7 frames/s rate). The shrinkage strain as a function of temperature was calculated using an open-source video analysis software [90] that can track the displacement. The strain values as a function of temperature were generally plotted by calculating the average values from cycles 2,3, and 4 (first cycle is not perfectly repeatable).

Photoactuation characterizations were executed by utilizing a UV LED lamp (OmniCure AC450, Lumen Dynamics) to irradiate unpolarized UV light up to 520 mW/cm^2 intensity. The photostrain values were calculated from the curvature of the film that was held by a tweezer in front of the UV lamp, or from performing photoactuation experiments where the film lifted 10mg weight against gravity.

PHANTOM V2511 High Speed Video Camera was used to capture images at high speed (5000 fps). For higher magnification imaging Smartzoom(5 Digital Microscope, ZEISS) used. Another useful tool is optical profilometer (VR-3200, Keyence) which could provide 3D data of the surface.

5.0 Main-Chain Liquid Crystalline Network (glassy)

Due to the higher concentration of nematogenic content in LC glassy materials compared to LCEs, and prior research that already demonstrated the effect of magnetic field on the molecular pattern of these materials, here we first studied this group of LC polymeric materials. The works reported in this chapter were undertaken to test hypothesis 1 in Chapter 3.

5.1 Study of Magnetic Field-induced Molecular Alignment in Main-Chain Liquid Crystalline Network (glassy)

In the preliminary work, we utilized two neodymium magnets to provide 300 mT magnetic field in the middle. While in the case of Freedericksz experiment the surface anchoring exists on both surfaces [39], we used PDMS on one side to limit the surface anchoring effect on one side only, making it more simple to detect the twist deformation optically, and without the need for the critical magnetic field setup. Therefore, 50 μm cells consisting of coverslip and PDMS were made. The coverslip was coated with Elvamide and rubbed with a velvet cloth to create a planar anchoring condition. When the monomer RM257 is introduced, the anchoring from the rubbed Elvamide created a monodomain molecular orientation. Application of the magnetic field transverse to this orientation should drive the twist in the molecular director. We found that indeed this is possible with this setup (300 mT magnetic flux density), with the temperature of the monomer at $0.9T_{NI}$ following a dwell-time of 300 seconds. T_{NI} is the nematic isotropic transition temperature. The competing effects of the surface anchoring and the magnetic field resulted in twisting the mesogen in a transition layer close to the rubbed surface (Figure 16a). The De Gennes's magnetic coherence length (ξ) was estimated $\xi = \frac{1}{H}\sqrt{\frac{K_{22}}{\chi_a}} \ll 10\mu m$ for a 300mT magnetic field, assuming $K_{22} \sim 10^{-7}$dyne (twist Frank constant) and $\chi_a \sim 10^{-7}$(the anisotropy of magnetic susceptibility in c.g.s.) [39, 91]. In a typical voxel $50\mu m \times 50\mu m \times 50\mu m$, when

the characteristic dimensions are much larger than ξ, the effect of anchoring from adjacent voxels declines exponentially and the alignment will be essentially dictated by the magnetic field [39]. The orientation was then fixed through selective photopolymerization. Figure 16b illustrates POM images of a gear-shaped LCN structure. Here, the layer was characterized by the planar orientation of the nematic director (perpendicular to the rubbing direction), where the corresponding geometric profile was selectively built. Due to the twisting in the transition layer, it can be observed similar to a twisted nematic orientation under POM. This can demonstrate the ability of patterning RM257 mesogens orientation by applying magnet field.

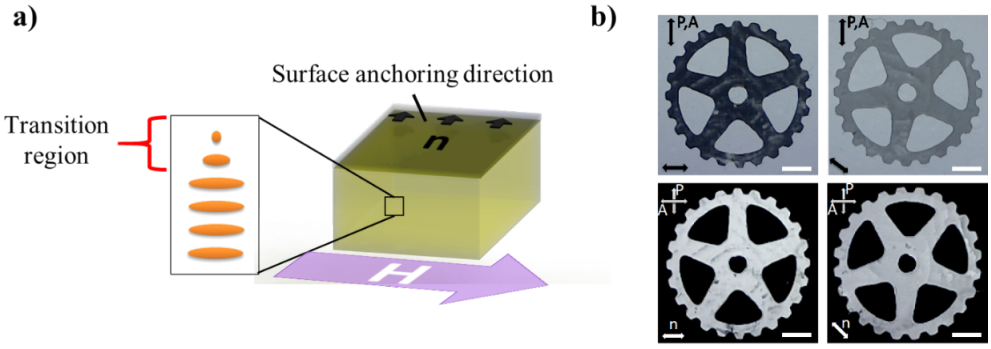

Figure 16: Controlling the molecular orientation of LCN material through the combination of surface anchoring and magnetic field. a) The voxel molecular orientation is programmed by applying a magnetic field. orthogonal to this orientation, which leads to a rotation of the director b) POM images of a gear-shaped layer that confirm the molecular order of the structure at 0° and 45° under parallel and crossed polarizer (P) and analyzer (A)) (All scale bars = 1 mm). Reprinted from with permission from [92] Copyright 2019 American Chemical Society.

To further study the magnetic-field induced mechanism in glassy material, the critical magnetic field was measured for RM82 monomer using the method that was described in details in sections 4.3.1 and 2.1. Since the measurement procedure needed to be implemented at $90°C$ (nematic phase temperature) for more than 2 hours, 1 wt % BHT was added to RM82 as thermal inhibitor. For a 15 μm cell, a certain threshold was observed around 389

mT, after which a sudden surge of the transmitted light intensity was observed (Figure 17). Based on this result, the ratio was calculated as $\frac{K_{22}}{\chi_a} \approx 2.18\ (A^2)$. This agrees with our initial estimation of ξ, and the dominance of the magnetically imposed alignment within a $50\mu m \times 50\mu m \times 50\mu m$ voxel.

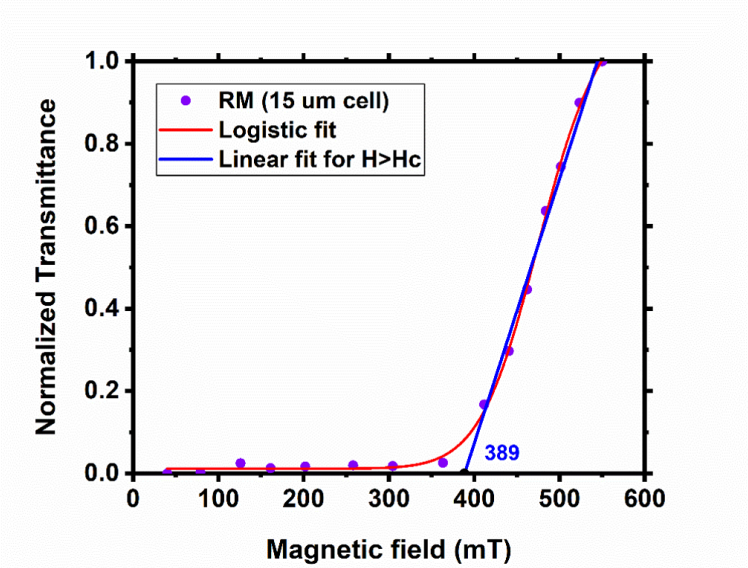

Figure 17: Normalized transmitted light intensity through a $15\mu m$ cell filled with RM82 monomer at nematic phase, versus applied magnetic field. Red line illustrates the fitted logistic curve, and the blue line was derived from linear fitting. $\frac{K_{22}}{\chi_a} \approx 2.18\ (A^2)$ can be calculated based on 389 mT critical magnetic field (H_C).

5.2 Voxelated Molecular Patterning in Three-dimensional Freeforms

*Reprinted from; Tabrizi, M.; Ware, T. H.; Shankar, M. R. Voxelated Molecular Patterning in 3-Dimensional Freeforms. ACS Appl. Mater. Interfaces 2019, acsami.9b04480.

Author Contributions

Mohsen Tabrizi (myself), Taylor H. Ware, and M. Ravi Shankar conceived the research. Mohsen Tabrizi composed the manuscript. M. Ravi Shankar oversaw the preparation of the manuscript. All authors reviewed the manuscript.

Here we presented a framework for breaking out of the confines of prior approaches by exploiting the combination of anisotropic magnetic susceptibility of the LC monomers and spatially-selective photopolymerization using a digital micromirror device (DMD) in a bottom-up (inverted) 3D printing configuration. The system illustrated in Figure 18a utilizes an indexable 300mT magnetic field (H) generated using permanent magnets, which are mounted on a rotation stage to drive alignment of the LC monomers. A DMD system (Vivitek D912HD projector) with a pixel resolution of $\sim 50\mu m$ polymerizes desired regions to preserve this orientation with spatial selectivity. The dimensions of the voxels are defined by the resolution of the DMD system (tens of μm). Independently dictating the alignment using a reorientable magnetic field and polymerizing as needed to build a 3D free-form layer-by-layer allows for fabricating structures, where the molecular alignment and the geometry can be defined in a truly voxel-by-voxel fashion. Furthermore, during the fabrication of each layer, the monomer is confined in a build-gap between the prior polymerized layer (or the build plate, if it is the first layer) and a Polydimethylsiloxane (PDMS) substrate. After selective polymerization under the influence of the reorientable magnetic field, the polymerized layer is detached from the PDMS substrate by retracting the build-plate to create the subsequent build-gap. The sample remains attached to the build-plate during the build process and after each retraction of the build-plate, a fresh monomer mixture (of same or different composition) is introduced. The process is then repeated. Thus, we decouple

the endowment of molecular alignment (defined by the field orientation) from the material build path (defined by the DMD system). As a result, the molecular orientation that was previously constrained by the geometry and the surface patterning or command layers, can now be directly encoded.

This platform does not restrict the molecular director to a fixed orientation in a given layer. Figure 18b, illustrates the creation of multiple nematic orientations in different voxels of a single layer. To demonstrate the idea, a glass build-plate was spin-coated with Elvamide and rubbed to create a surface anchoring condition (along n_x) to emulate a prior layer and it is positioned $50\mu m$ away from a PDMS substrate. A monomer mixture composed of 95 wt.% mesogenic monomer RM257, 1 wt.% photoinitiator Irgacure 369 (2-Benzyl-2-dimethylamino-1-(4-morpholinophenyl)-butanone-1) and 4 wt.% UV-absorber Tinuvin 328 (2-(2H-Benzotriazol-2-yl)-4,6-di-tert-pentylphenol) was introduced in the build-gap. A constant temperature of 100 $^{\circ}C$ was maintained and a 300mT magnetic field was applied perpendicular (in plane) to the surface anchoring direction for 300 s (dwell time). Selective photopolymerization (with 0.8 s exposure time and 170 mW/cm^2 intensity) using the DMD system was used to crosslink regions with a director pattern, which is rotated by $\pi/2$ with respect to the prior alignment. After which, the magnetic field was rotated to restore the axis with n_x in the unpolymerized regions. Meanwhile, alignment of the already crosslinked regions remains fixed. Crosslinking of the remaining monomer was then used to generate a striped sample with alternating layers of uniform alignment along n_x in some regions and rotated nematic patterns in the rest.

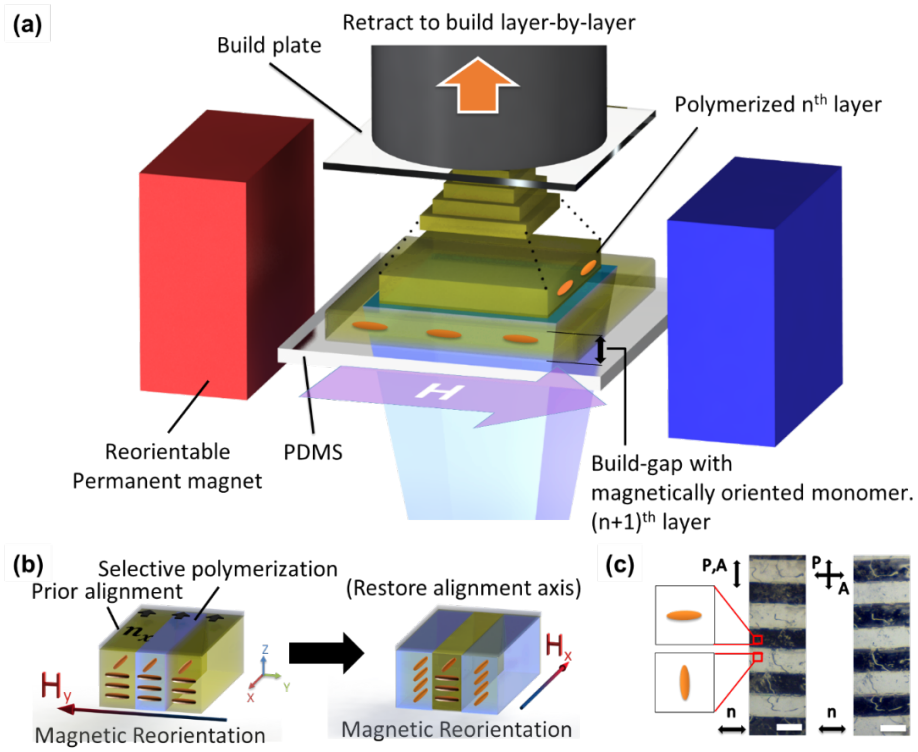

Figure 18: a) Schematic of a layer-by-layer 3D printing system capable of fabricating three dimensional geometries with molecular alignment encoded using a magnetic field. Reorienting the magnetic field on demand and spatially selective polymerization using a DMD light source allow for independently indexing the molecular orientation voxel-by-voxel b) Example of control over the molecular director within a given layer. A build-plate with an alignment layer is used to trigger a preferred alignment direction. Application of a magnetic field reorients this alignment, which is selectively frozen-in via crosslinking. Then, the magnetic field is rotated to coincide with the prior orientation, following which crosslinking is used to preserve the patterning. c) Polarized optical microscopy (POM) images of the sample with mutually orthogonal molecular orientation, which was generated using the steps described in b. The regions with uniaxial alignment are bright (maximum light transmission through the material, polarizer and analyzer) at 0° and dark (less light transmission) at 45° under parallel polarizers (images in the left) and dark at 0° and bright at 45° under crossed polarizers (images in the right). Other regions are characterized by a pattern, which is rotated through the thickness (All scale bars = 1 mm). Reprinted from [92].

Figure 18c illustrates the polarized optical microscopy (POM) images of a single layer built using this idea. The parallel and crossed polarizer (P) and analyzer (A) images illustrate regions where the director patterns are all aligned along n_x or are rotated perpendicular with respect to n_x by the magnetic field. Parenthetically, we note the presence of a temperature window for orienting and polymerizing the mesogenic monomers without requiring any temperature cycling. The ability to 3D print molecularly-ordered polymers at a constant temperature eliminates in-process deformation of the responsive material and added process-time due to the heating-cooling cycles. Often, temperature cycling into the isotropic state of the monomer followed by cooling into the nematic state in the presence of an orienting field has been used [25, 93]. Eliminating this thermal cycling decreases the possibility of thermal curing of the monomer during the printing.

Table 1: Heat-Responsive Monomer Mixtures of Various Compositions, Their Curing Temperature, and Parameters

chemical composition and printing process conditions	R3P1T1	R3P0.5T1	R3P1T4	R3P1T1I0.5
RM257 [wt %]	98	98.5	95	97.5
I369 photoinitiator [wt %]	1	0.5	1	1
Tinuvin (UV light absorber) [wt %]	1	1	4	1
inhibitor methylhydroquinone [wt %]	0	0	0	0.5
Q_c $[mJ/cm^3]$	20.8±3.1	66.0±2.2	44.1±5	105.3±2.6
D_0 $[\mu m]$	909±105	1083±80	740±116	352±50

When seeking to create complex geometries with highly defined structural features, the ability to control the polymerization depth in individual polymerized voxels becomes critical. We found that the interplay of the optical absorption of absorbing dyes and relative concentrations of photoinitiator and inhibitor of polymerization can provide control over the depth to which crosslinking occurs within the build-gap. But for this control, as the material is built, unintended polymerization can occur, especially when overhanging structures are fabricated in subsequent layers. To achieve this control, while simultaneously achiev-

Table 2: Light-Responsive Monomer Mixtures of Various Compositions, Their Curing Temperature, and Parameters

chemical composition and printing process conditions	RZ7P1	RZ7P1R0.1
RM257 [wt %]	89	88.9
Azo 6C [wt %]	10	10
I784 photoinitiator [wt %]	1	1
methyl red (visible light absorber) [wt %]	0	0.1
Q_c $[mJ/cm^3]$	194.6±23.1	565.1±24.4
D_0 $[\mu m]$	628±56	113±6

ing molecularly-ordered material, a range of monomer mixtures were developed. RM257, a diacrylate, was used as the host-mesogen, which generate temperature sensitive actuation. Doping with an azobenzene-functionalized crosslinker (Azo6c) endows light responsive actuation. For the compositions shown in Tables 1 and 2 ,the polymerization depth (D_p) is found to be a function of the photonic energy dosage ($\sim It$) where I is the intensity and t is the exposure time. We utilize the scaling relation: $D_p = D_0 ln(It/Q_c)$, where D_0 and Q_c are constants characteristic of the monomer mixture [94]. The curing depth was measured for the variety of photonic energy intensities and material compositions in Tables 1 and 2. By controlling the grayscale values in the 2D patterns, which were projected, control over the light intensity was achieved. Direct measurements of intensity using a power meter were performed. To measure the polymerization depth, the build plate was placed ~ 2 mm from the PDMS and the whole gap was filled with the monomer. By exposing square patterns with different intensities, the polymerization started from the PDMS surface up to some level below the build plate. Squares with higher intensity (brighter patterns) cured up to higher levels. Measuring the thickness of these squares by a digital micrometer yielded polymerization depth for the respected conditions. This data was used to populate the "working curves", which are illustrated in Figures 19a,b. D_0 encapsulates the effect of attenuation of light through the monomer and its effect on the depth to which polymerization occurs. An

effective approach for controlling this parameter is via the addition of the absorbing dyes. For thermally responsive RM257-based resins (Table 1), controlling the concentration of the UV absorber (Tinuvin) leads to a smaller D_0. See Figure 19a for comparison of R3P1T1 vs R3P1T4, where the slope of the working curve is smaller with increasing UV absorber. The effect of the photoinitiator on the slope, however, is small as seen from the comparison of R3P1T1 vs R3P0.5T1. These systems are polymerized using Irgacure 369 (Ciba) as the photoinitiator and using unfiltered irradiation from the projector, which has components from UV to visible. In contrast, the azobenzene-functionalized materials (Table 2) are polymerized using light filtered with a 495 nm long-pass filter to avoid isomerizing the azobenzene during the polymer- ization. Here, Irgacure 784 (Ciba) is used as the photoinitiator and methyl red is used as the absorber. The working curves for the photoresponsive resins are illustrated in 19b. We identify compositions and processing conditions to overcome challenges in the incorporation of photochromic molecules, which modify the stability of the mesophase and present challenges in cross-linking monomers with spatial selectivity to preserve the molecular order [95, 96]. The constant Q_c in Figure 19a,b is correlated with the minimum energy density that is required to start the polymerization, which increases when the amount of photoinitiator is decreased. This can be seen by comparing Q_c for R3P1T1 vs R3P0.5T1. A similar increase in the Q_c is observed when a polymerization inhibitor (methylhydroquinone) is added in the composition R3P1T1I0.5. Increasing Q_c leads to a shifting of the working curves to the right, wherein the intercept along the x-axis (energy dose) increases. These calibration curves enable the scalable fabrication of molecularly ordered freeforms at scales, which outstrip conventional cell-based fabrication methods, while also enabling precise control over the geometry. Figure 19c illustrates a pyramid-like structure fabricated with R3P1T1, where the molecular director (n) throughout the sample is oriented along the indicated arrow. The pyramid is 3.8 mm high made of 38 layers with a 100 μm layer thickness. Access to molecularly patterned structures at these scales holds the key to magnifying the work potential and the utility of LCN actuators in practical systems.

The versatility of this framework is illustrated in an array of examples, including thermomechanical generation of Gaussian curved structures from flat geometries (Figure 20a) and light responsive freeform topographies (Figure 20b). In the first case, a ring-shaped

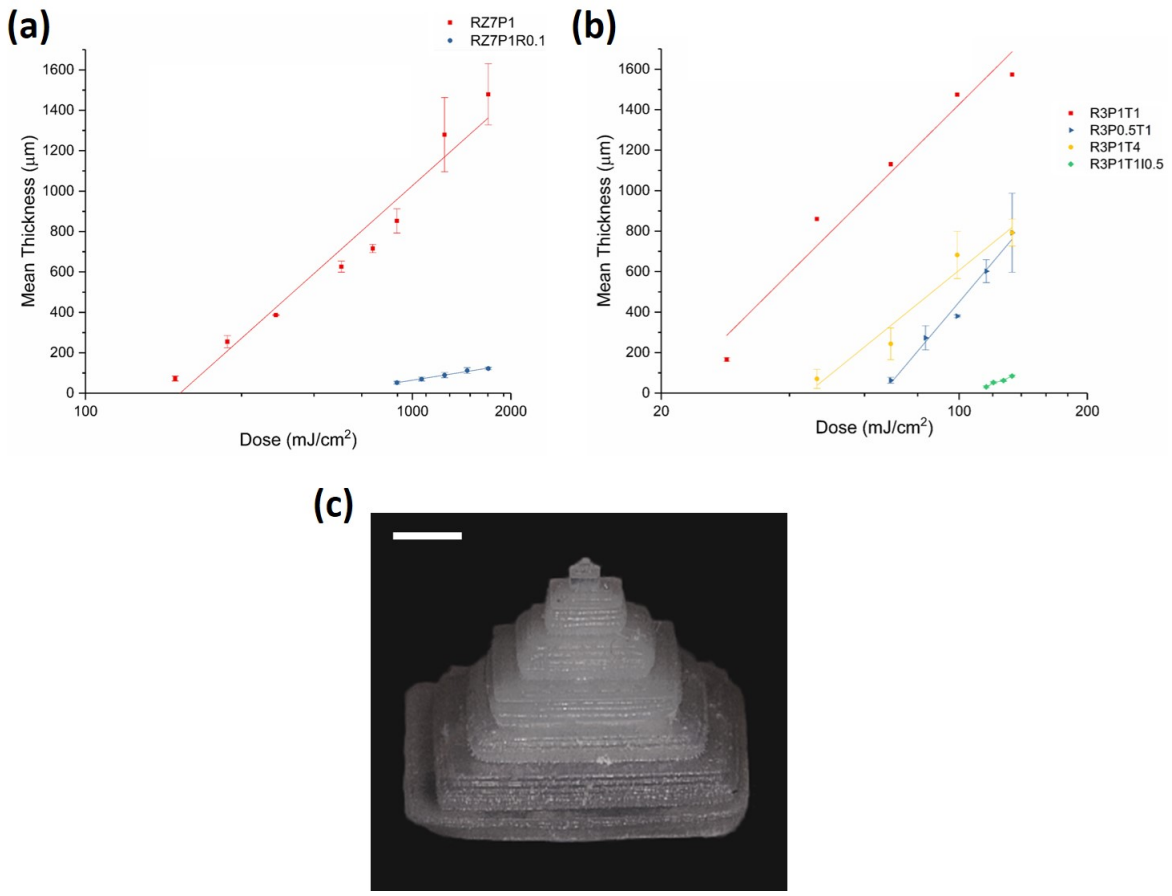

Figure 19: Polymerization depth as a function of irradiation energy dosage for various compositions. (a) Heat-responsive LCN mixtures. (b) Azobenzene-functionalized light-responsive mixtures. (c) Image of a 3.8 mm high pyramid structure made of R3P1T1 which is aligned uniaxially (blue arrow) throughout the sample. This figure illustrates the scalability of the proposed fabrication method (scale bar = 1 mm). Reprinted from [92].

structure was printed, segment by segment (see Appendix B), with the director pattern, which is azimuthally oriented. This ring can also be thought of as an annular section of a +1 topological defect [21]. This was integrated with a subsequent layer, which was printed with a square weave-hatched pattern and a polydomain alignment, in the absence of a magnetic field. This structure allows for exploiting the idea of overcurvature to create geometries with a Gaussian curvature, even when starting from a prior flat state [97]. While a bilayered

flat strip will bend when heated, confining the bilayer into a closed ring with a curvature orthogonal to that generated with heat can trigger buckling out of the plane. While this has been explored in the buckling of rods [97], here, we exploit our fabrication platform to drive transformations of surfaces from a flat state into the one characterized by negative Gaussian curvature. The overcurvature is defined by the parameter $O_p = \sqrt{1 + (\kappa R)^2}$, where κ is the curvature caused by the heat actuation and is orthogonal to the in-plane curvature R^{-1}. At room temperature $O_p = 1$ ($\kappa = 0$), the geometry is flat with an initial curvature R^{-1}. $R = 2.6$ mm in Figure 20a. By increasing the temperature ($\kappa > 0$), the ring generates an orthogonal curvature κ. As the periphery of the sample buckles out of plane to minimize the bending and torsional energies, the hatched surface is forced by the constraints along its periphery into a negative Gaussian-curved shape. By modifying the value of R,differing levels of overcurvature can be accessed to create a range of geometries following thermal stimulation (see Appendix B).

Monomer system RZ7P1R0.1 was used to demonstrate the fabrication of light-responsive microstructures in Figure 20b. Azobenzene-functionalized mixtures result in a glassy LCN, which respond to irradiation with 365 nm UV by bending toward the actinic light [98]. The ability to spatiotemporally modulate the actinic light to direct actuation in microstructures is particularly attractive for creating functional surfaces and active topographies. In contrast to prior approaches, involving cholesteric self-assembly [8] or micromolding [99], the design space possible with the 3D printing approach is broader, including opportunities creating re-entrant microstructures, which are capable of unusual properties (e.g., robust superomniphobic responses [100]). Figure 20b illustrates an 86 array of overhanging cantilevers mounted on pillars with different heights (also, see Appendix B). The idea is to demonstrate fine structures composed of re-entrant features, which are responsive to light. This system was polymerized using light filtered with a 495 nm long-pass filter to avoid isomerizing the azobenzene during the polymerization. The pillars have polydomain molecular orientation, and the molecular directors in the monodomain cantilevers are aligned parallel to their long axis, as illustrated in Figure 20b. Cantilevers are 60 μm thick and 700 μm long. During the sample development to wash off residual monomers after finishing the printing process, the capillary forces from the solvent bent the cantilevers downward. This can be solved by

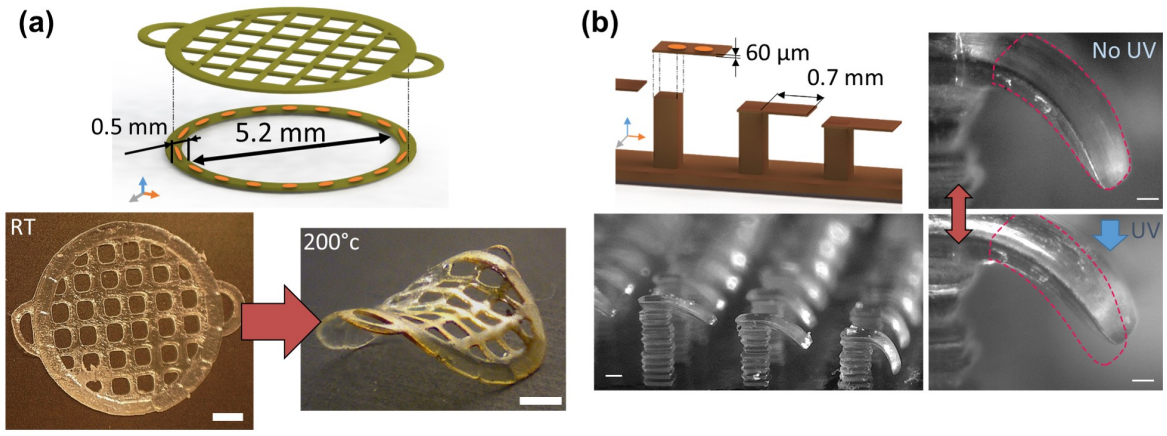

Figure 20: a) Harnessing the response of a 3D printed bilayered actuator in overcurvature-driven assembly of Gaussian curved geometries. Creating an annular geometry with an azimuthally-patterned director, which resides on a hatch-patterned suspensory structure (polydomain) elicits the creation of a Gaussian curved (saddle-like geometry), when heated (scale bars = 1 mm) b) Light responsive array of microstructures is shown. The overhanging cantilevers are monodomain, while the vertical pillars are polydomain. Irradiation with 365 nm UV elicits a bending of the cantilevers. Insets illustrate the schematic of actuation due to photoisomerization of azobenzene. Red dashed outlines indicate the initial shape of the cantilever before the actuation (scale bar of the array image = 200 μm, scale bars of a single cantilever on the right = 50 μm). Reprinted from [92].

utilizing support structures, which are removed after the development. When this structure is irradiated from the top, the absorption of light by the overhanging cantilevers leads to their bending toward the light. The deflection is illustrated by tracking the outline of the cantilever, as illustrated in Figure 20b. Graded contractile strains ($\sim -1.8\%$ strain on the exposed side) are generated along the nematic director, which generates the bending. Strains were calculated by measuring the change in the curvature of the cantilevers ($\Delta\kappa$) and the initial bending angle (α). After the UV light was turned off, the cantilever spon-

taneously relaxed to its initial shape after $\sim$ 30 min at ambient temperature. The ability to fabricate such responsive microstructures along arbitrary surface profiles can hold the key to modulating functional responses, including hydrophobicity, fluid drag, and biological responses.

This framework also allows for arbitrary modulation of the composition of the material from one layer to another. Functional gradations become possible to integrate multi-responsiveness in a facile manner to create response profiles, which were hitherto inaccessible. To accomplish this, after printing with monomer 1, the build plate is retracted to release the sample from the PDMS substrate. After the temperature is lowered to ambient, a solvent (toluene and isopropyl alcohol (IPA) in a 4:1 weight ratio) is introduced to dissolve the residual monomers while not swelling the polymerized structure. Then, the build plate is reset to the desired location, and the temperature is raised to dry the build gap. Now, the second monomer is introduced, and the build process continues. Using this multicomposition process, a multi-responsive robotic arm was built. Figure 21 illustrates an arm, which is capable of 2 independent degrees of freedom (θ_y and θ_x), which are responsive to light and heat respectively. The segments of the arm are intentionally bulky to ensure they remain entirely non-responsive and serve a structural role. Joint 1, which is designed to be light responsive (was made from RZ7P1R0.1 monomer) and is characterized by a homeotropic alignment through its thin axis over the entire thickness of 75 μm. Irradiating this joint with 365nm light leads to bending away from the actinic source. Irradiating from different sides can be used to drive back and forth actuation at this joint by $\theta_y \sim 9^\circ$. Another joint (joint 2), was fabricated with the heat responsive monomer mixture (R3P1T4) in a bilayered configuration as illustrated in Figure 21. The slender axis (60 μm thickness) of this joint is designed to be normal to that of joint 1 to enable the bending to occur along an orthogonal axis. Heating the entire structure elicits a bending behavior along $\theta_x \sim 11^\circ$. This behavior is roughly analogous to that observed in twisted nematic LCN created using an analogous composition in Ref [93]. In addition to actuating the joints using one stimulus at a time, the combined application of heat and light leads to the simultaneous triggering of manipulation along both θ_y and θ_x. Further study could assess the development of sequential actuation by fabricating robotic components with different transition temperatures [30] or separate light-responsive

units (joints) that can be actuated independently [101]. This work also paves the way for applications such as mechanical logic [102, 103] in which each active unit acts as an input and a specific complex route can be programmed by utilizing the embodied AND/OR/NAND logics. This can give rise to the development of feedback loop, adaptability, and autonomy that are the major concepts in developing robots.

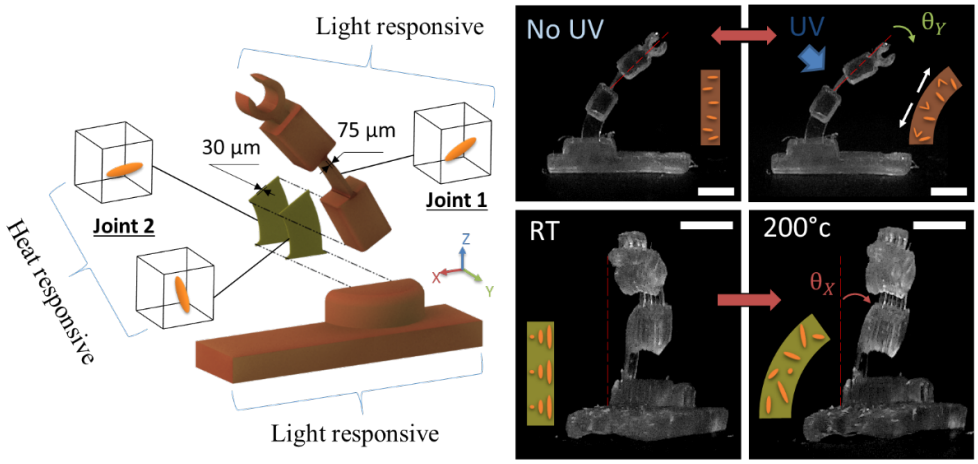

Figure 21: Two-axis robotic arm, which is directly 3D printed to realize responses to different stimuli in the different joints. Joint 1 is responsive to light, by bending away from the actinic light due to its molecular pattern. Joint 2 is a bilayered system, which is responsive to heat. Actuation with light (θ_y) is shown in the top and the thermal actuation (θ_x) is shown in the bottom. Red dashed are used to illustrate the original location of the fingers of the arm (scale bars = 1 mm). Note the different views used in the figure panels to illustrate the multiaxial manipulation in response to different stimuli. Reprinted from [92].

Despite the aforementioned davantages of this platform, the response magnitude of the printed actuators are not big enough. The characteristic strain in glassy LCN is $\sim$1%. Indeed, side-chain LCE's can be aligned with a moderate magnetic field (0.1-0.5 T) to demonstrate large strain actuations (40%) [24, 25], they produce small actuation stress (few kPa) that limits their functionality. Therefore, more studies for investigating the magnetically-assisted patterning of main-chain LCEs are required. In the next chapter, different strategies were exercised to address and resolve these issues.

6.0 Main-Chain Liquid Crystalline Elastomer

The main goal of this chapter is to identify and develop a new LCE composition with enhanced thermomechanical and photomechanical properties. By creating new structures using the proposed framework, we further demonstrate unconventional soft robotic applications.

6.1 Magnetic Field-induced Molecular Alignment in Liquid Crystalline Gels

To enhance the material softness, we introduced thiol chain extenders (such as EDDT (2,2′-(ethyl- enedioxy) diethanethiol))to the mixture and prepared the mixture via a Michael-addition reaction [7, 30]. This synthesis method is made of two-step reactions. First, the composition goes through oligomerization initiated by Triethylamine (Sigma-Aldrich). This results in a weakly cross-linked network material. In the second step, the molecular alignment is locked-in by fully polymerizing the material. Similar to section 5.1, we first tried to investigate the influence of magnetic field by trying to make twisted nematic samples inside a PDMS\coverslip cell (magnetic field direction $\perp$ rubbing direction). We observed the inadequacy of the 300 mT magnetic field (as well as elvamide surface anchoring) in controlling the molecular orientation (check Appendix B for POM images). This can be explained by the higher molecular weight of the oligomers [49], and lower magnetic anisotropy in the mixture due to smaller concentration of the mesogenic content. To address these challenges, we can either utilize a strong magnetic field ($> 1T$ flux density) [49] or increase magnetic anisotropy by including more mesogenic components.

The nonreactive LC mixture E7 (Figure 22) can be a good candidate due to its high magnetic anisotropy (Figure 15b) and relatively low rotational viscosity. Therefore, the mixture was diluted with E7 for the purpose of increasing the magnetic anisotropy (As mentioned in Chapter 1, this results in liquid crystalline gel or nematic gels as the final sample, rather than LCE). First, mesogen RM82, the thiol chain extender, triallyl-1,3,5-triazine-2,4,6-trione (TATATO) crosslinker, and Triethylamine were mixed and melted. After

mixing E7 with this mixture at 90 $^{\circ}C$ (isotropic temperature), the mixture was oligomerized through Michael-addition reaction after 3 h at 50 $^{\circ}C$. We utilized three different thiols, (2,2′-(ethyl- enedioxy) diethanethiol (EDDT), glycol di(3-mercaptopropionate) (GDMP), and 4,4′-Bis(mercaptomethyl)biphenyl (BMBP) are the thiols (Figure 22), to assess their effect on the magnetic alignment and thermomechanical properties. The E7 concentration for these three compositions was optimized to achieve magnetically driven alignment in these mixtures (Table 3). Finally, the photopolymerization was performed by UV light at room temperature (nematic phase) under the presence of the magnetic field (similar to glassy material) to fix the orientation and finalize the polymerization. The sample was later washed to remove the unreacted monomers by following the method described in Ref [13].

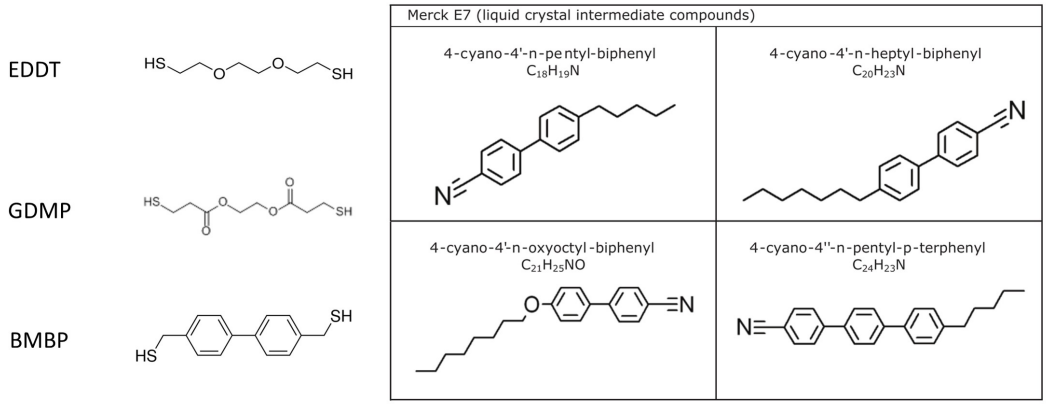

Figure 22: Chemical structure of the thiol chain extenders and E7 nematic solvent used to make different nematic gel compositions.

As shown in Table 3, the composition with BMBP thiol can be aligned with 300 mT magnetic field with significantly less amount of E7 (50% vs 70%). This is the result of its higher magnetic susceptibility due to the possession of benzene rings. From the actuation point of view, GDMP thiol is more ideal as it can demonstrate higher thermomechanical deformation at lower temperatures (i.e. less input energy required). Figure 23 shows the thermal actuation of a nematic gel made of 70% wt. E7 and 7.2% wt. GDMP thiol. This has been repeated for multiple cycles within the range of 23-50°C. We observed that increasing the final actuation temperature more than this can prevent full relaxation and repeatability.

Table 3: Comparison of Composition and Thermomechanical Properties of Different Nematic Gels.

Thiol chain extender	EDDT	GDMP	BMBP
E7 [wt %]	70	70	50
Actuation Strain [%]	35	40	30
Actuation Temperature [$^{\circ}C$]	60	50	70

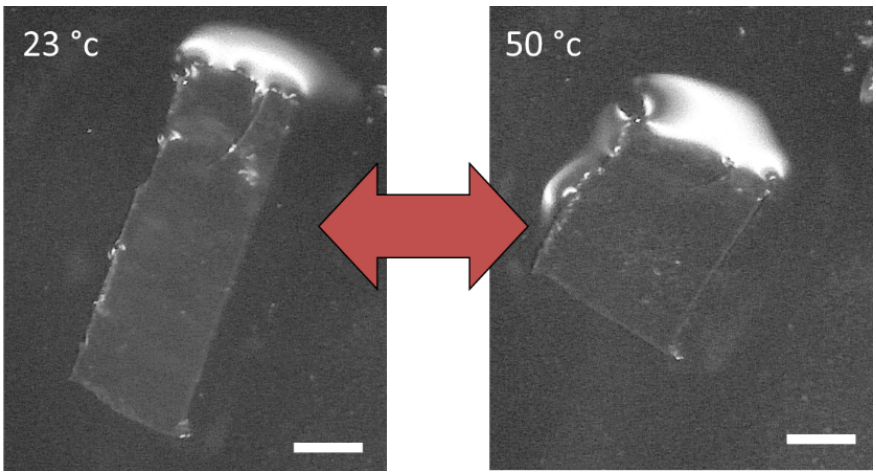

Figure 23: Reversible 40% strain thermal actuation of GDMP nematic gel (scale bars = 1 mm).

In order to 3D print these materials through previously (see section 5.2) discussed voxelated molecular patterning platform, I369 (2.5% wt.) as photoinitiator, BHT (2.4% wt.) as thermal inhibitor, and Tinuvin (4% wt.) as light-absorber were added to the composition. While these materials demonstrated some interesting advantages and capabilities, such as demonstrating high deformations at low temperatures, we faced multiple challenges in printing them. After finishing the photopolymerization and printing procedure, the uncured monomers should be washed away by solvent. In this case, we immersed the printed part in

THF (Tetrahydrofuran, Sigma-Aldrich) for 5 minutes. However, the nematic solvent E7 was removed after this step. This swollen sample was unable to demonstrate reversible actuations. To solve this, we decided to follow the procedure reported in Ref [13]. Through the first step, the sample deswelled inside methanol after 10 minutes. Then for the purpose of reintroducing E7, the dried sample was immersed in E7 and went through a thermal cycle (room temperature - 80°C) to have the network fully swollen in E7. However, all these steps resulted in extreme irreversible deformations and curling of the samples (Figure 24) during which the material can also stick to itself. Further work is required to address these challenges by utilizing solvents that can cause less swelling\deswelling. Applying E7 to wash away the monomer could be an alternative method to minimize these challenges. Moreover, the nematic gels can not produce deformations with high work densities due to their inability to generate high stress actuations. Therefore we decided to focus more on developing main-chain LCEs that can be aligned with magnetic field.

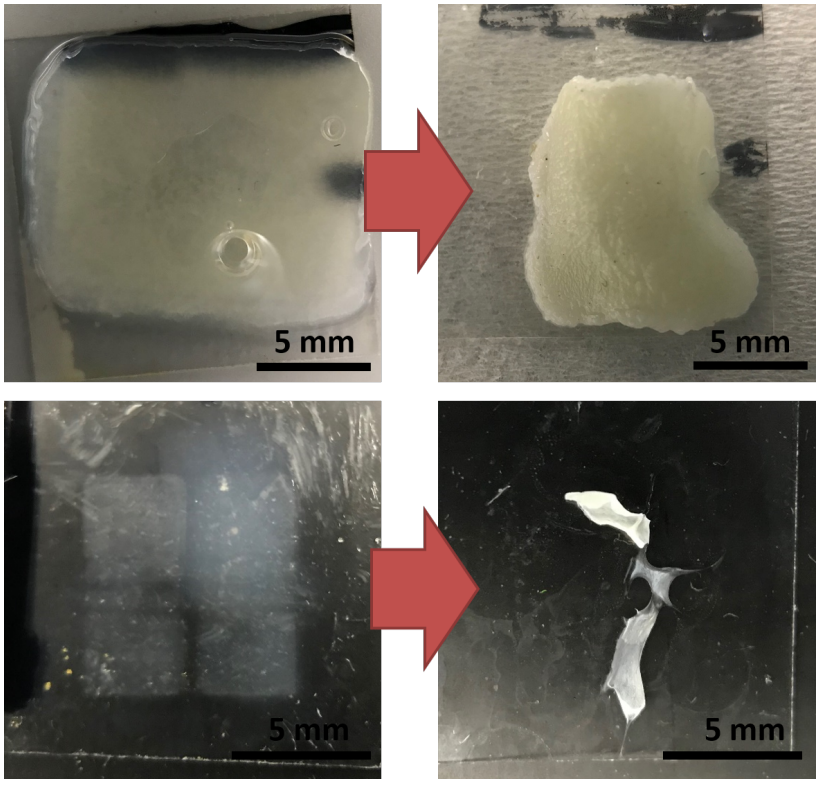

Figure 24: Challenges in 3D printing nematic gel

6.2 Synthesis of Liquid Crystalline Elastomer by Introducing Chain Transfer Agent (CTA)

As discussed in the previous section, we tried to make softer materials and decrease the crosslinking density of the glassy composition by introducing thiol chain extenders. We explored the feasibility of the common two-step Michael-addition synthesis method to make magnetically aligned LCEs. However, the results showed that a weak magnetic field (<0.5 T) is not able to dictate the alignment of the oligomers, synthesized through the Michael-addition reaction. Godman et al. [104] reported a distinct and facile strategy to synthesize LCEs and decrease the crosslinking density by applying chain transfer agent (CTA). In their study, 1,4-benzenedimethanethiol (BDMT) was used for the chain transfer process (chain termination) during the reaction process, leading to lower crosslinking density. Unlike the Michael-addition two-step procedure, the mixture can be polymerized directly without any requirement for oligomerization. We adopted this procedure by employing BDMT and Tetrabromomethane (TBM) as CTAs to RM82 monomer (glassy), and further studied how these can influence change in order parameter in presence of the external magnetic field.

Table 4: Monomer Mixtures of Various Compositions

chemical composition	RM	RMC3	RMT10C3	RMZ4T10C3
RM82 [wt %]	99	96	86	80
BDMT [wt %]	0	0	10	10
Azo 6C [wt %]	0	0	0	4
TBM [wt %]	0	3	3	3
BHT [wt %]	1	1	3	3

Table 4 shows different compositions that were developed with the goal of decreasing crosslinking density while maintaining the ability to control the alignment with magnetic field. We first checked the adequacy of the 300 mT magnetic field for programming the molecular orientation of these mixtures by making twisted nematic samples inside a PDMS\coverslip cell (magnetic field direction $\perp$ rubbing direction) and analyzing the align-

ment by POM observations (Figure 41 in Appendix B). In order to study the magnetic-induced alignment mechanism and compare the influence of each component in more detail, the critical magnetic fields (H_C) were measured as a function of thiol chain extenders, CTA, and mesogen concentration (Figure 40 in Appendix B). The measurements were conducted at nematic phase temperature. As we also observed before, a temperature window ($0.7T_{NI} - 0.9T_{NI}$) exists for orienting the mesogenic monomers. However, we observed that the temperature value (within the range) has a negligible effect on the magnetic threshold. Thus no further study to measure H_C as a function of temperature was needed. Compositions that contain BDMT require more BHT thermal inhibitor to prevent thermal polymerization during the measurements. To better compare the compositions independent of cell thickness, $\frac{K_{22}}{\chi_a}$ ratio (twist elastic constant over magnetic susceptibility) was further calculated by applying Equation 6.1, and further illustrated in Table 5. This is also helpful to understand the correlation between the molecular structure and the diamagnetic anisotropy. For the first step to decrease the crosslinking density, 3 wt % TBM was added to RM82 glass composition. This composition (RMC3) shows an insignificant change in $\frac{K_{22}}{\chi_a}$ ratio compared to RM. Therefore TBM is demonstrated to be a useful component in maintaining the order in presence of the magnetic field. The BDMT was increased as much as we can obtain surface-induced alignment, without which the critical field measurement conditions can not be met. Interestingly, we were unable to make optically clear with perfect uniaxial aligned samples for a composition with 10 % wt BDMT and TBM. In contrast to the TBM effect, the concentration of the chain extender (BDMT) demonstrated remarkable control on the elastic constant ($\frac{K_{22}}{\chi_a}$ dropped by 60 % for RMT10C3). Similarly, it can be observed that the incorporation of the azobenzene dye to the network (RMZ4T10C composition) also increased the threshold magnetic field as expected (lower magnetic susceptibility and higher elastic constant).

Table 5: Influence of the Materials Composition (chain transfer agent, chain extender, and azobenzene) on Twist Elastic Constant and Magnetic Susceptibility.

	RM	RMC3	RMT10C3	RMZ4T10C3
$\frac{K_{22}}{\chi_a}(A^2)$	2.18	2.24	3.58	4.23

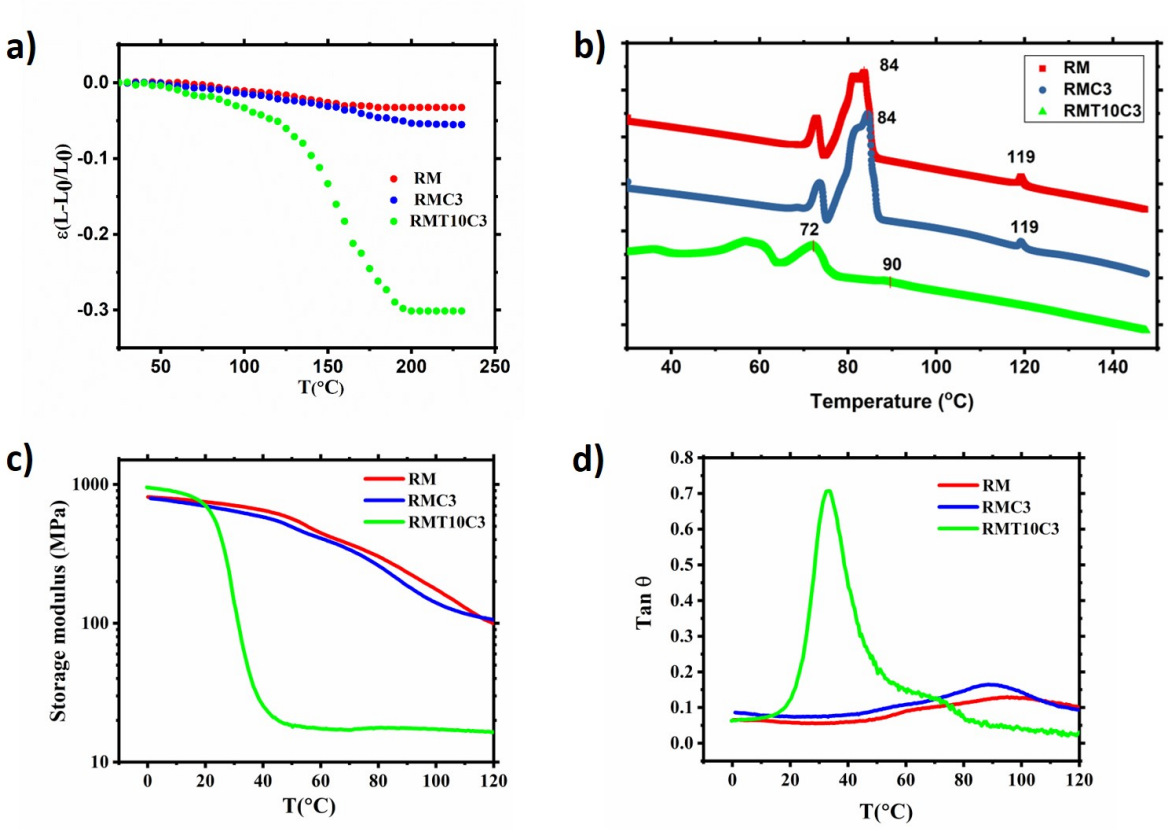

Figure 25: Thermomechanical properties of material as a function of composition. a) Thermal actuation strains. b). c & d) DMA curves shows change in material viscoelasticity by introducing TBM and BDMT to the composition.

After understanding the effect of mesogen, chain transfer agent, and chain extender concentrations, we studied their effects on material properties. We first characterized the thermomechanical properties by measuring the shrinkage strain of a uniaxially aligned LCE

film as a function of temperature. To fabricate LCE films, the monomer infiltrated PDMS-PDMS cells with 50 μm gap. Once the external 300 mT magnetic field was applied at nematic temperature, the mixture was further polymerized by UV light, without any requirement for oligomerization reactions. Figure 25a shows the average of thermalstrain for three cycles (cycles 2,3, and 4) for each composition. RMT10C3 sample demonstrated up to 30% shrinkage strain which is extremely higher than the strain of glassy materials (RM). This is mainly caused by the presence of the BDMT, as the inclusion of only TBM (RMC3) did not increase the shrinkage strain by more than 10 %. To determine the phase transition temperatures of the unpolymerized mixture, differential scanning calorimetry (DSC) measurements were conducted for the compositions in the form of powder mixtures. The T_{NI} values were additionally confirmed by POM observations. The results indicate that the inclusion of TBM resulted in very minor changes, While phase transition temperatures (T_g and T_{NI}) decreased significantly after adding BDMT (Figure 25). To further characterize the thermomechanical properties as a function of monomer structure, dynamic mechanical analysis (DMA) was utilized to measure storage modulus (E') and phase lag ($Tan\theta$). From Figure 25c and d, it can be seen that by far the BDMT component has the main role in enhancing the material softness.

Taken together, we tuned material properties and molecular alignability by changing the material network through the introduction of TBM and BDMT to the mixture. The results showed that RMT10C3 composition can be identified as a great candidate to be 3D printed into complex LCE structures, since it can be aligned by low-intensity magnetic fields and can undergo large strain shape changes (up to 30 % shrinkage strain).

6.3 Three-dimensional Blueprinting of the Molecular Order in Light Responsive LCEs

In the last section, we successfully applied the versatile CTA synthetic method to develop a new LCE that can be programmed with a 300mT external magnetic field and is capable of generating large mechanical deformations in response to the stimuli. This can break the

limitations of the previous work with glassy materials, paving the way for more practical applications. Figure 26a shows the main components of this new mixture (RMZ4T10C3). In the next step, we exercised a similar approach as section 5.2 to blueprint the molecular orientation voxel-by-voxel in 3D freeforms (Figure 26b). To begin the process, the monomer mixture is introduced to the system at the nematic temperature and infiltrates the gap between the window and build-plate. The mesogens order is controlled independently by an external rotatable magnetic field (300mT). The mesogens in the monomer state can always be reoriented (twist in this case) by the field. However, the reorientation is not instantaneous and a few minutes of dwell time (depending on the material and the strength of the magnetic field) is always needed. Once the orientation is fully accomplished, selective photopolymerization by the DMD system induces the crosslinking that results in a LCE voxel with fixed alignment (Figure 26c). As in-situ POM observations show (Figure 42 in Appendix B), the alignment is fully conserved after polymerization. After a layer of material is fabricated through the repetition of reorientation-polymerization sequences, the build-plate is lifted, detaching the polymerized layer from the window. While in the previous work the PDMS coating on the window was able to prevent the adhesion of the printed glassy material into the window, the presence of the BDMT thiol in the new LCE composition reduces the oxygen inhibition effect, resulting in sticking the printed layer to the window [105]. Therefore, optically clear FEP tape was used on the window to avoid this. The freeform is 3D printed through these layer-by-layer fabrication steps. Finally, the surplus uncured monomer needs to be dissolved and washed away by PGMEA solvent, followed by drying and post-curing. In this work, we focused on the light source as the external stimulus. Compared to other environmental stimuli, light has provides unique advantages such as scalability and high spatiotemporal control. By making some optical setups (e.g. utilizing DMD [101]), photonic energy can be transferred in a form of complex patterns without a physical connection requirement. Furthermore, concepts such as self-shading and self-regulation [106] can be easily exploited for soft robotics applications. To endow light-sensitive actuation, the composition was doped with azobenzene cross-linker. The composition was tailored for the printing procedure by including the free radical photoinitiator, 1 wt % Irgacure 784 (Ciba Specialty Chemicals), and light absorbing dye, 0.1 wt % methyl red.

The latter also helped to inhibit thermal polymerization in addition to deceasing the light scattering and increasing the printing resolution. Therefore, BHT was not needed anymore.

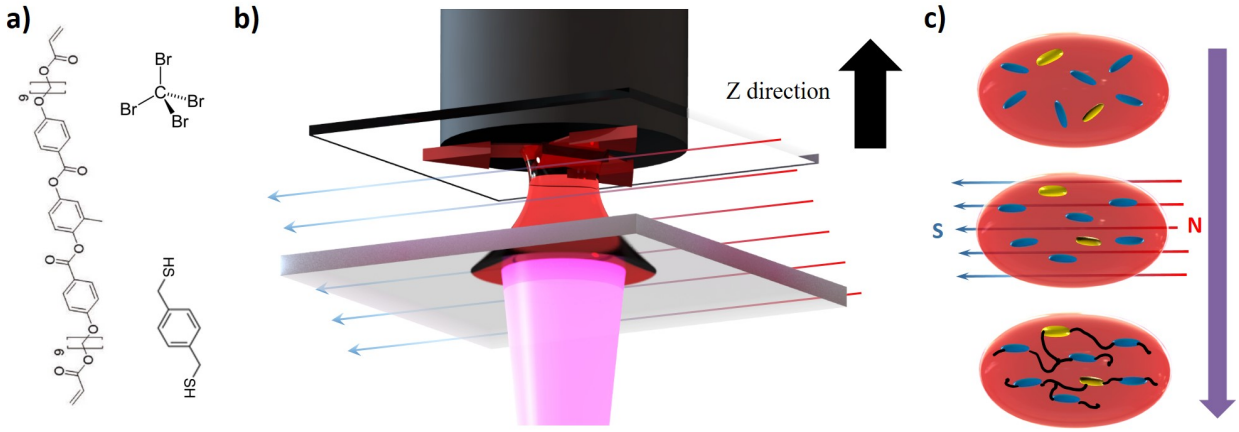

Figure 26: a) Chemical structure of the LC monomers, TBM chain transfer agent, and BDMT thiol used in the mixture to print 3D freeforms. b) Schematic of the bottom-up 3D printing system. c) The underlying principle of LCE molecular patterning. Mesogens within a voxel of material are aligned by a reorientable magnetic field. The orientation is subsequently locked-in through selective photopolymerization.

Before fabricating complex structures first we need to realize the optimal printing parameters and conditions (such as curing temperature, dwell time, curing time, and exposure intensity) as well as to characterize the photoactuation performance. The latter is, in particular, required to understand the design space for soft robotic applications. The alignment rate and required time for the mesogens to rotate and align parallel with the magnetic field (dwell time) depends on the twist viscosity, elastic constant, and the applied magnetic field (see section 2.1). The decay rate, however, is independent of the field value (H_C) and only depends on the composition and cell thickness. We used the same critical field setup for the decay rate ($\tau^{-1}(0)$) measurements to realize the dynamic nature of the mesogens. As illustrated in Figure 27a, the reorientation is relatively quick and the decay rate is ~ 35 seconds. This data can also be useful for future works in which the samples need to be transferred outside the magnetic field for further polymerization. Nevertheless, this data is not sufficient

to estimate the dwell time due to different boundary conditions. Figure 27b shows the in-situ POM observation (check subsection 4.2.3) of the evolution of the molecular order after 10 minutes at 65 $°C$ under the influence of the 300 mT magnetic field. The boundary conditions are FEP with weak anchoring on the bottom and elvamide with strong anchoring on the top, rubbed in a direction perpendicular to the magnetic field. It can be seen that the optically clear LC monomer is obtained after 10 minutes. This is higher than the required dwell time (5 minutes) for glassy materials, resulting from the higher elastic constant (and probably twist viscosity) of the LCE composition. In addition to making the process time-consuming, this long dwell time can also lead to unintended thermal polymerization and the requirement for thermal inhibitors.

While in the previous work the resolution of the voxels was $50\mu m \times 50\mu m \times 50\mu m$, after finalizing the setup modifications the resolution increased to $8\mu m \times 8\mu m \times 8\mu m$. At this scale, we need to take the influence of the surface anchoring and magnetic coherence length (ξ) into account. As it was shown in section 2.1, the critical field in presence of strong anchoring on both walls can be derived from the following:

$$H_C = \frac{\pi}{d}(\frac{K_{22}}{\chi_a})^{1/2} \tag{6.1}$$

For the case of walls with weak anchoring effects, the equation needs to be modified by adding the surface term:

$$H_C = \frac{\pi}{d + 2l_e}(\frac{K_{22}}{\chi_a})^{1/2} \tag{6.2}$$

where

$$l_e = \frac{K_{22}}{W} \tag{6.3}$$

W is surface anchoring strength For strong anchoring $W \to \infty$.

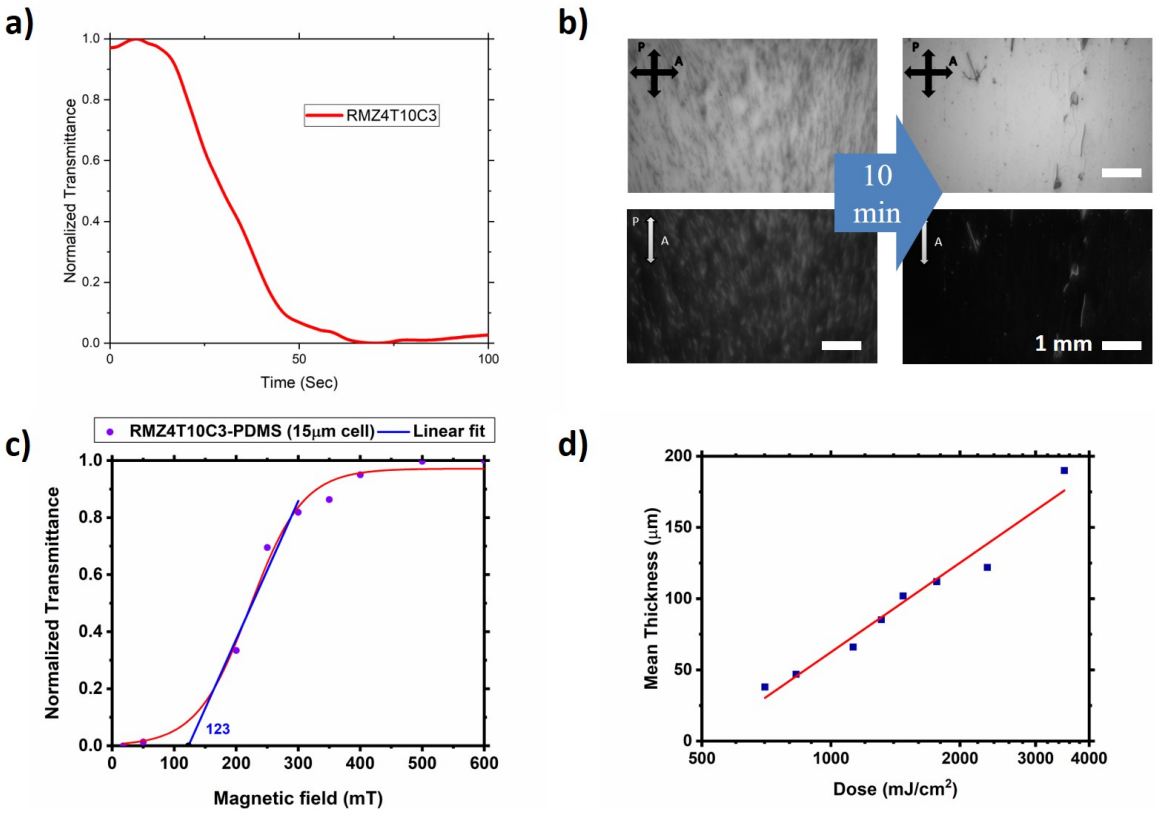

Figure 27: 3d. a) Change in the light transmission of material as a function of time once the magnetic field is removed, demonstrating the mesogens reorientation. This data is useful to understand the dynamic mechanism of magnetic alignment and decay time and decay rate phenomena (2.15). b) In-situ POM images of LC monomer mixture right after being fed to the printer compared to after 10 minutes dwell time (magnetic field $\perp$ surface induced alignment). c) Measuring critical field (H_C) for RMZ4T10C3 composition with weak anchoring on one wall (PDMS coating) and strong anchoring on the other (rubbed elvamide). d) Working curve was developed to enhance the control over polymerization depth and voxel depth resolution.

For the current printer configuration, the lateral resolution (in XY plane) can be derived based on the boundary conditions of the voxel and can be categorized into the following three groups:

1. No adjacent voxel is cured:

   In this case, no surface anchoring exists and the dimensions of the voxel are dictated solely by the resolution of the DMD system (in this case 8 μm).

2. One adjacent voxels is cured

   The polymerized LCE has a strong anchoring and can affect the mesogens alignment. Assuming that the splay and bend elastic constants have approximately the same values as the twist elastic constant, the lateral resolution can be estimated from the following:

$$L_{min} = \xi = \frac{1}{H}(\frac{K_{22}}{\chi_a})^{1/2} = \frac{\mu}{B}(\frac{K_{22}}{\chi_a})^{1/2} \tag{6.4}$$

   Based on the data from Table 5, it was calculated $L_{min} \approx 8.6\mu m$.

3. Both walls are polymerized

   This case is similar to the critical field measurement conditions, having strong anchoring on both walls. As it was demonstrated in section 2.1, at critical field ($H = H_C$) the magnetic coherence length can be derived from $\xi = \frac{d}{\pi}$ [39]. Thus, we calculated the minimum width from the followings:

$$L_{min} = \pi\xi = \frac{\pi}{H}(\frac{K_{22}}{\chi_a})^{1/2} = \pi\frac{\mu}{B}(\frac{K_{22}}{\chi_a})^{1/2} \tag{6.5}$$

   After substituting the values from Table 5 and B=0.3T, we get $L_{min} \approx 27\mu m$.

This resolution in the depth (Z) is slightly a different case, as it is governed by the platform (or the previous printed layer) position or the material composition and the photonic energy of the exposed light, rather than the DMD system. From the molecular alignment point of view, there is always a weak surface anchoring condition in the bottom surface of the voxel (due to FEP or PDMS coating), and strong anchoring from the Elvamide (or printed material) surface. Instead of measuring the surface anchoring for the FEP or PDMS materials directly, the critical field was measured for the LC monomer that was sandwiched between PDMS (weak anchoring) and rubbed elvamide (strong anchoring), resembling the 3D printing case. Based on the critical field value (H_C) measured from this, we can derive the resolution from the following:

$$Z_{min} = \pi\xi = \frac{H_C \times d}{H} = \frac{130.5 \times 15}{300} \approx 6.15\mu m \tag{6.6}$$

These results are summarized in Table 6. This data enabled a pathway for high resolution 3D printing of LCE using magnetically assisted stereolithography.

Table 6: Estimations of the Minimum Dimensions of a Voxel of Material to Obtain Fully Independent Magnetically Induced Alignment (300 mT magnetic field).

	XY (case 1)	XY (case 2)	XY (case 3)	Z
Minimum dimension [μm]	8	9	27	6.15

In addition to the constraint of achieving independent mesogenic orientation within the voxel, the polymerization depth is also another crucial factor that determines the voxel depth. While in many cases the depth is the same as the gap between the window and the previously printed layer (or build plate in the case of first layer), for the case of structures with overhanging features the depth value is dictated by the interplay of the light energy dosage, the optical properties of the composition (absorption or scattering effect), and required energy to initiate the polymerization. For the composition that was developed for this work, the polymerization depth (or minimum thickness) was plotted as a function of photonic energy dosage (Figure 27d). This plot, which is referred to as "working curve", was used to determine the intensity of the polymerization light to achieve the desired thickness.

Having determined the printing conditions, we next investigated the photomechanical responsiveness of the LCE that can be printed by this proposed method. A single layer $6cm \times 4cm$ rectangular LCE strip with $50\mu m$ thickness was printed through the process that was discussed. The mesogens were aligned in a monodomain configuration along the length by the magnetic field. After developing the sample, it was mounted vertically and a 10 mg weight was hung from its lower end (Figure 28a). Once the sample was exposed to UV light it contracted along its length due to decreasing the order parameter. This

resulted in raising the weight. Upon turning off the UV light source, the sample relaxed toward its original shape, lowering the weight. We repeated this for three cycles and for two different intensities (420 mW/cm^2 & 530 mW/cm^2). From the graph in Figure 28b we can see that the first cycles are not fully reversible (1.5 % for 420 mW/cm^2 and 8 % residual for 530 mW/cm^2). This mechanical hysteresis effect was reported in previous work of other research groups [68], is mostly caused by the lack of complete crosslinking during the polymerization step or by incomplete cis isomerization once the light is off. The latter can be circumvented through long blue light illumination. Nonetheless, the sequential actuation almost stabilized after the first cycle and the mechanical deformations were mostly repeatable. In both weight lifting experiments, photothermal aspects exist that work in conjunction with the photoactuation. For the case of the lower intensity (420 mW/cm^2), the light energy increased the temperature up to $85°C$ (Figure 28c). Based on Figure 25a this can lead to $\sim 1.7\%$ contraction. Therefore the photoisomerization dominates the mechanical deformation for this intensity ($\sim 5\%$ repeatable strain). On the other hand, the high intensity irradiation (530 mW/cm^2) generated much higher deformations ($\sim 11\%$ repeatable strain). This is due to the fact that the photothermal effect is significantly higher compared to the previous case ($\sim 3.2\%$ thermalstrain at $100°C$). This result demonstrated that by controlling the light intensity we can tune the displacement of the actuator. Furthermore, we performed photogenerated actuations with much higher strain ($5 - 11\%$) with this newly developed LCE compared to glassy material ($\sim 1\%$).

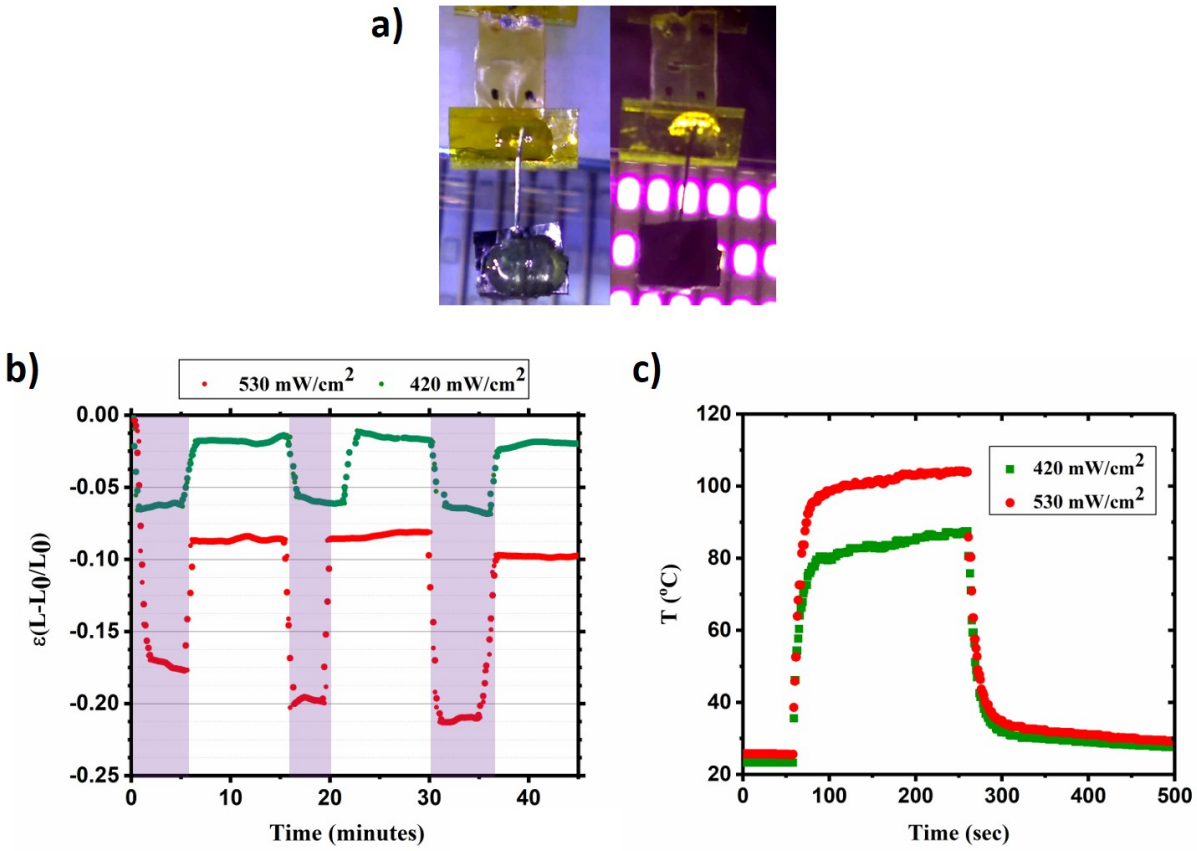

Figure 28: Mechanical response of the printed uniaxially aligned LCE to UV light at two different intensities. Repeatable shape changes of up to 10% in response were observed. a) Image of the weight lifting setup. The magnetically aligned LCE film lifts a 10mg weight in response to UV light exposure. b) LCE photostrain shrinkage for three consecutive cycles. c) The photothermal effect for two different light intensities (420 mW/cm^2 & 530 mW/cm^2).

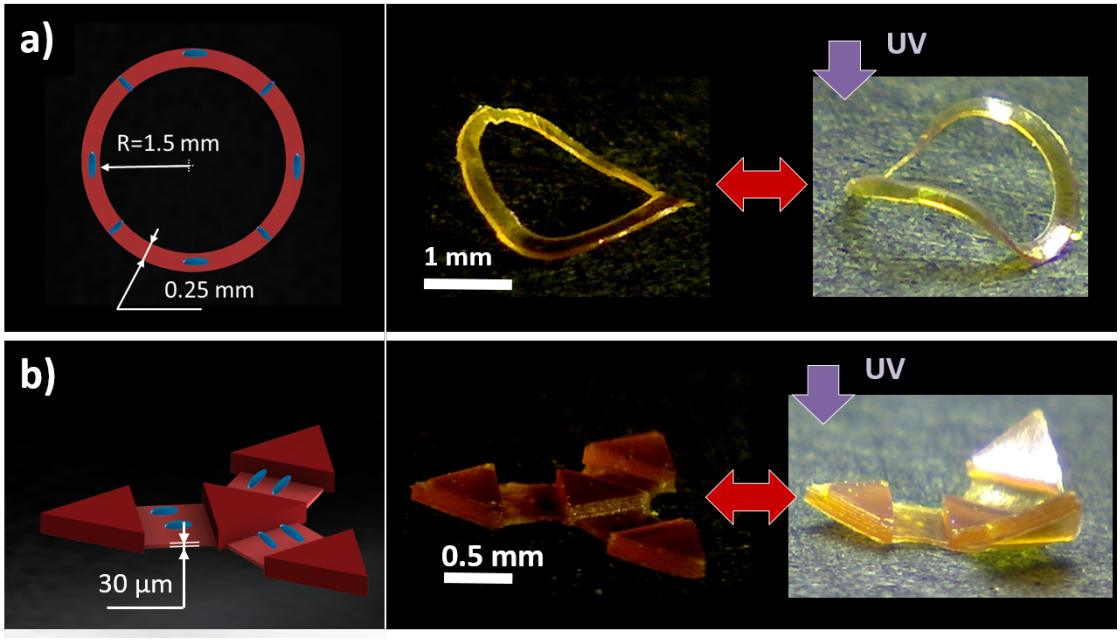

Figure 29: 3D printed structures with controlled and reversible shape morphing in response to UV light. a) "-1 defect" ring. b) Gripper-like structure.

To further demonstrate the versatility of this platform using the newly developed material (RMZ4T10C3), we printed multiple light responsive LCE structures. First, a $50\mu m$ thick ring with a complex molecular orientation (-1 topological defect) pattern was printed. Since the sample was photopolymerization at elevated temperatures (65 $°C$), it was deformed into a 3D shape after development and peeling due to anisotropic thermal expansion [107]. The ring demonstrated highly repeatable shape change in response to 530 mW/cm^2 UV light (Figure 29a). The next sample is a gripper-like structure with three fingers. Due to the active monodomain alignment of the fingers, they can bend reversibly in response to UV exposure (Figure 29b).

Thus far, we identified and optimize monomer compositions, derived the printing conditions, characterized the photomechanical responsiveness of the printed sample, and finally provided a few examples of printed LCE 3D structures with preprogrammed voxelated molecular patterning, capable of reversible shape change in response to UV light source. In the chapter that follows, a novel soft robotic application of the proposed platform is presented.

6.4 Demonstration of a Real-world Application: Biomimetic Microflier with Controllable Flight Dynamics

The design and development of miniature flying robots have recently been studied by researchers using inspirations from nature such as flying insects or small birds. Piezoactuator driving wings remain the most commonly applied method to generate mechanical propulsion at this scale [108, 109]. However, delivering the required energy (utilizing wires that tether the robot to the power supply, on-board battery, or photovoltaic array) to the actuator and integrating the control system remain the major challenges due to weight limitation of the flying devices [110, 111]. This can even make the flaying impractical when scaled down to few centimeters. Light-weight LCE actuators on the other hand can be activated and controlled remotely by light with spatiotemporal selectivity. However, research to date has not yet demonstrated any LCE applications for this field. Rogers and coworkers [112] studied free falling seeds and then designed and manufactured a bio-inspired 3D microflier with enhanced levels of performance (high drag forces and low terminal velocities) during the fall. Novel applications such as environmental monitoring (e.g. fine dust pollution) were further proposed and illustrated through the integration of battery-free colorimetric sensors. However, no active mechanical element was used and integrated into the fliers and their work failed to demonstrate any control over the flight dynamics.

Maple (Acer) seeds, like many other wind-dispersed seeds, possess high elevated performance and aerodynamic efficacy that enable them to travel considerable distances [113]. This can be attributed to high lift forces generated through the autorotation of the seeds as they descend. 3D measurements of the flow around a dynamically scaled model of the maple seed revealed that the "angles of attack" (angle between the seed's reference line and the flow direction or more accurately $\alpha = \arctan(V_d/V_h)$, where V_d is descent speed and V_h is horizontal speed) and wing shape play the major roles in generation of the lift force [114]. As a result, the aerodynamic efficacy of the seed can be tuned by varying the angles of attack. Inspired by this flight mechanism and the potential of control over the flight dynamics through the shape change, a regular maple seed was scanned at different angles by the optical profilometer (VR-3200, Keyence) and then the 3D data were merged into a single

3D geometry using Geomagic (3D Systems). This 3D shape (reverse engineered data) was later used to design our seed in Solidworks (Dassault Systems). To mimic the heavy nut and the leading edge of the seed, the same regions were designed with higher thickness (150 μm). Figure 30a illustrates the steps were undertaken to design and print the microflier inspired by a real maple seed. The molecular orientation was programmed in a way that the angle of attack and the profile change as a result of UV irradiation (Figure 30b). The mechanical deformation was limited to the thinner area (25 μm thick) while the leading edge and the core maintain their original shape due to their higher thickness. To study the change in the flight dynamics of the microflier in response to UV light, we made a simple setup (Figure 43, Appendix B) to drop it from the same location and monitor the fall by a high speed video camera at 5000 fps rate. The videos were captured at 25 cm distance from the dropping point, where its rotating movement is more stable without much deviation to the sides. For the case of "UV on", the microflier was dropped after being exposed to 530 mW/cm^2 UV exposure for 1 minute. Each case was repeated 5 times to ensure the reliability and repeatability of the data. The results (Figures 30c and d) verified that UV light can be used to control the flight dynamics of the microflier. The falling speed and pitch length increased by 15.5% and 34% respectively. Basically, the microflier demonstrated more non-rotating behavior and less lift generation in presence of the UV owing to the change in its profile shape and decline of the angle of attack. The considerable variation of the data for the case of "UV on" can be explained by non-uniform relaxation of the microflier as it was moving away from the UV source in addition to less flight stability.

This proposed microflier benefits from a simple and remote controlling method, UV lamp, without the need to expose the light at a certain angle. We can further take advantage of the light as the power source to irradiate the microflier at different frequencies and with more spatiotemporal selectivity. We can envision a swarm of these microfliers that are dispersed over an area and their flying behavior is selectively and locally controlled by the light. Sensor integration for the purpose of data collection, as discussed by Kim et al., can further broaden the applications of these structures [112].

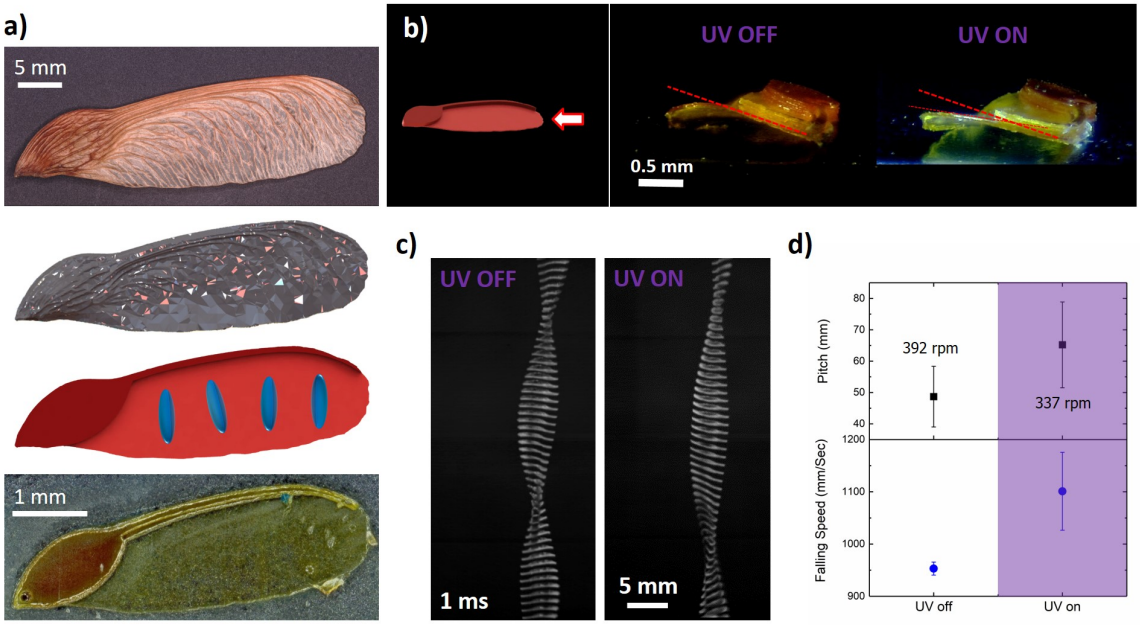

Figure 30: Tuning the flight dynamics of the LCE microflier inspired by autorotating maple seeds. a) Design and fabrication of the LCE microflier through reverse-engineering of a maple seed. b) Change in the seed profile in response to UV irradiation. c) Tracking the autorotating free-flight path of a the printed seed (in presence and absence of the UV irradiation). The images were generated by time stacking images with 1 ms intervals. d) Increase in average falling speed (15.5% increase) and average pitch distance (34% increase) as the result of UV light exposure. For each case 5 trials were implemented.

7.0 Conclusion and Future Work

The present research aims to study the molecular patterning within voxels of liquid crystal (LC) polymeric materials by using remote low intensity (<0.5 T) magnetic fields. To bridge the gap between these materials and practical applications, it is essential to alleviate the shortcomings of the current state of research with respect to geometrical complexity of the structures and freedom of molecular orientation programming independent from the geometry, process conditions, and boundary conditions. Encoding the orientation with magnetic alignment is the best candidate method for achieving this. To study the mechanism of magnetic alignment, propose and develop a new LCE composition that can be aligned by low-intensity magnetic fields, hypotheses and required tasks were identified and discussed in Chapter 3. Through the preliminary work in chapter 5, the concept of magnetically controlling the molecular pattern was firstly demonstrated for Main-chain LCN (glassy) materials. A framework for voxel-by-voxel indexing of the molecular order in 3D freeforms was realized with magnetically-assisted additive manufacturing of LCNs. We utilized a reorientable magnetic field and spatially-resolved irradiation from a digital micromirror device to build 3D objects in an inverted (bottom-up) configuration. This platform expands the design space of molecularly-ordered solids to enable microstructural and composition gradients in hitherto difficult-to-realize geometries. As exemplars, we fabricated a heat responsive structure that generates Gaussian curvatures from initially flat, light responsive freeform topographies and a multiresponsive robotic manipulator. However, high crosslinking density of the LCN network restricts its shape morphing (< 1% strain). In Chapter 6 multiple strategies were undertaken to enhance the softness. A new LCE composition was developed through a straightforward chain transfer reaction synthesis strategy. We explored the mechanism of magnetic field alignment as well as thermomechanical characterizations for different concentrations of mesogens, chain transfer agent, Thiol chain-extender, and azobenzene dye. After identifying the printing parameters and conditions, the capability of this was further exemplified in fabricating a light responsive gripper and a topological defect. Finally, we demonstrated the capability of this work by creating a novel bioinspired microflier with

controllable flight dynamics. It has the potential to be utilized as a soft robot or for environmental monitoring. This work enables researchers in a variety of fields from soft robotics to implantable medical devices. This work will also accelerate a growing trend in manufacturing techniques that are designed to introduce molecular-level control into engineering structures. Specifically, the fields of self-assembly and liquid crystal chemistry will be further integrated into additive manufacturing; it is expected that this integration will lead to further advances in the design of smart materials and devices.

Future research will be continued to investigate the implementations of the newly developed LCE material and the proposed platform. The potential biomedical applications can be explored through the development of implantable devices, tissue scaffolds, and bioelectronics. The ongoing research is at the confluence of material design and process engineering to assimilate multifunctionalities ranging from actuation, sensing, optical activity (polarization control and engineered photonic bandgaps). In the following sections, the main goals and preliminary findings of the future studies are provided.

7.1 Ultra-thin Light Responsive Artificial Muscle

Researchers have achieved unprecedented material properties such as negative index of refraction, through development of metamaterials whose structures are engineered on small scales (from nano- to micrometers). The aim of this work is to create smart metamaterials with tunable properties. The ability to tune the gap between metastructure and gold allows us to manipulate meta-atom for multi-resonance. Liquid crystal elastomers (LCEs) are a suitable candidate material for achieving this since it can generate large reversible deformations in response to light exposure through order-disorder transitions in the macromolecular network. Blueprinting spatially heterogeneous molecular patterns to direct the large work potential is a compelling feature of the LC polymeric materials. While most of the researchers apply command surfaces to define the molecular orientation, the thickness ($\sim$ 90 nm) of these command layers is considerable for the metastructure experiments and can significantly influence the resonance. On the other hand, applying an external magnetic

field to control LC molecular orientation eliminates the need for the alignment layer. The most important advantage of the magnetic-driven alignment is the capability of encoding each voxel independent of the geometry and the adjacent layers. Furthermore, since it interacts with the volume of material, it is a scalable method. The LCE composition that was developed in this work is a desirable choice as it can be aligned with magnetic field and demonstrate up to 10 % deformation strain in response to UV light.

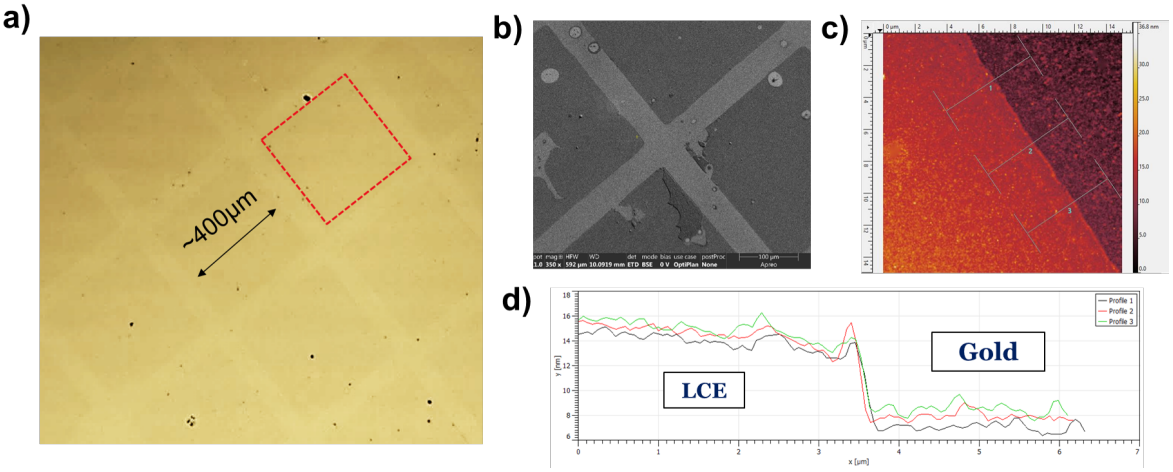

Figure 31: Characterization of ∼10 nm thick LCE pads a) Optical microscopy and b) SEM Image of arrays of LCE pads. c) AFM of the pad edge. d) AFM line scan to measure thickness.

Ultrathin LCE pads with less than 15 nm thickness (Figure 31) were created on gold \titanium substrate through soft lithography process (see Figure 44 in Appendix B for process steps). Another advantage of this composition is lower viscosity compared to other LCE monomers or oligomers which facilitates the LCE infiltration. Due to the small thickness of these pads, we were unable to investigate the molecular orientations. Recently, our collaborator Anqi Ji from Brongersma Group successfully demonstrated thermomechanical actuation of the pads which confirms the vertical orientation of the mesogens. Since nm-scale LCEs were developed for the first time in this work, these shape changing results can further help us to understand the thermomechanical responsiveness of LCEs at this scale. We are hoping to finalize the photomechanical characterizations of this platform and demonstrate this interesting and unconventional application soon.

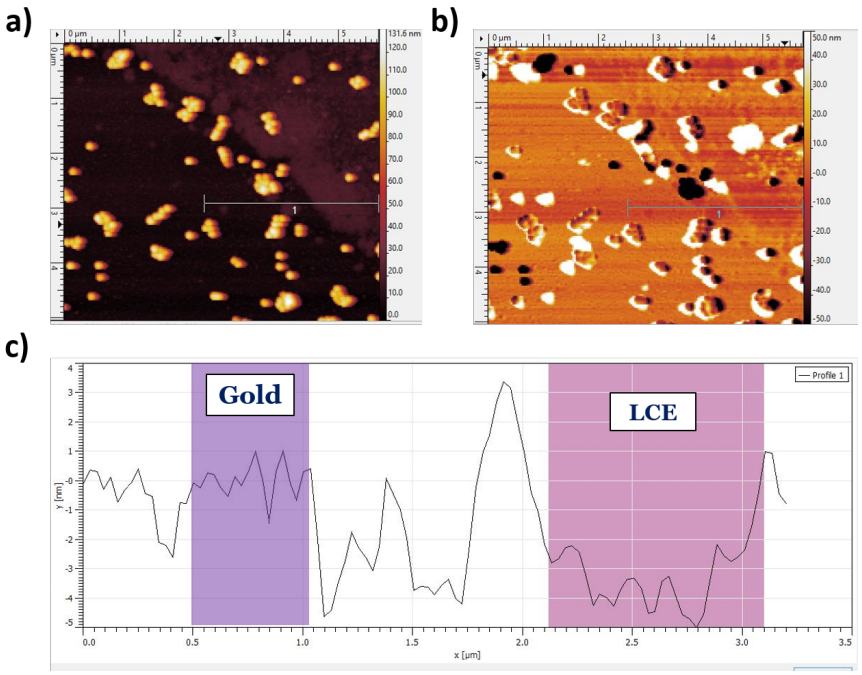

Figure 32: Thermomechanical responsiveness of the ultrathin LCE pads a) AFM of the pad edge at room temperature. b) Subtraction of AFM data the pad edge at 165 $°C$ from AFM data at room temperature. This helps us to track the change of thickness in different regions. c) AFM line scan to measure thickness change from the subtracted data. The LCE region data illustrated 3.3 nm shrinkage.

7.2 3D Print Choleretic Liquid Crystal (CLC) Polymeric Materials

The work reported here mainly focused on LC polymeric materials in Nematic phase for mechanical response purposes. We proposed and demonstrated the capability to blueprint the molecular order of the achiral LC monomers within a voxel of material within microscale resolution. While it significantly expands the design space of the encodable mechanical responses, the dependency of the resolution on the voxel size can be broken through patterning the order of LC monomers in chiral phases. The cholesteric pitch can be controlled by varying the concentration of the dopant as well as the intensity and direction of the

external magnetic field [115, 116, 117]. This can substantially enhance the patterning resolution to 400-1000nm scales, comparable to the wavelength of light ranging from visible to near-IR. This endows non-trivial optomechanical functionalities such as stimuli-responsive color-changes (Figure 33a) [118, 119]. Further studies are needed to investigate the effect of mesogenic monomer content, chiral dopant concentration and magnetic field intensity and orientation on the chiral molecular alignment. It is also required to characterize the optomechanical response of objects change structural color in response to stimulus. Similar to our work reported here, by combining this patterning approach with selective polymerization, we can ultimately print freeforms with sub-voxel chiral molecular orientations that can perform both mechanical morphing and tunable structural color in response to the stimuli. As illustrated in Figure 33b, Pozo et al. were successful in fabrication of freeforms from cholesteric liquid crystalline photonic photoresist through DLW method. However, the cholesteric pitch was dictated only by the dopant concentration and sub-voxel chiral molecular orientations was not exploited in their work [120].

7.3 Study the Mechanism of the Magnetic Alignment for Other LC Polymeric Materials

The setup we used in this work to study the mechanism of magnetic alignment for different compositions (check subsection 4.3.1), has the limitation of 0.6 Tesla as the maximum magnetic flux density. While this was sufficient for most of the compositions that were developed in this work, materials with high molecular weight may require field strength as high as 1.12 Tesla to obtain alignment, as shown in Ref [49]. A high intensity magnetic field setup capable of generating up to 2 T within a 20 mm gap, has already been purchased and assembled (Figure 34). As the next step, we can go back and study the alignment of the oligomers prepared through Michael-addition reaction. As discussed in the next section, this setup is also useful to understand the magnetic alignment for new LCE composites as well. The same setup can further be exploited to fabricate LCEs that require high intensity magnetic field through polymerization in presence of the magnetic field.

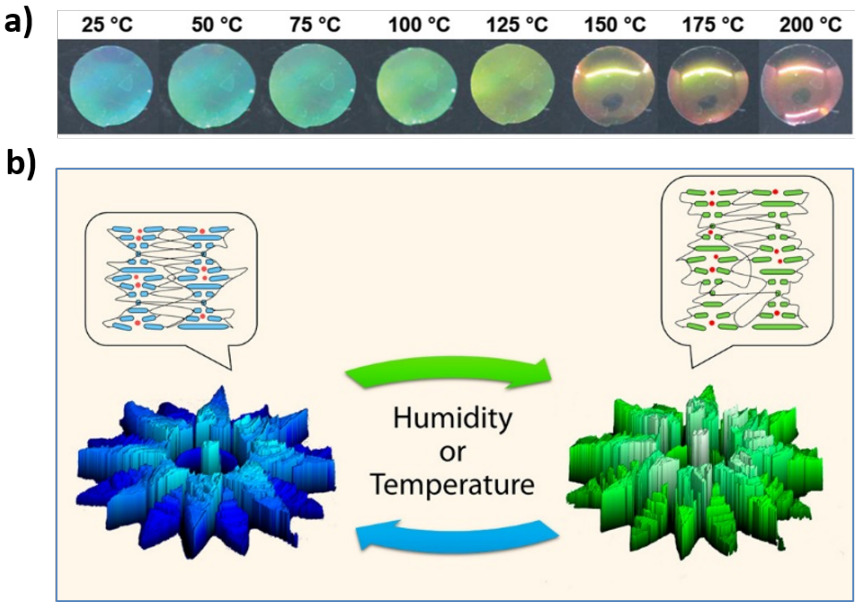

Figure 33: a) Heat-responsive color-change of cholesteric liquid crystal elastomer (CLCE) films. Reprinted from [121], with permission from John Wiley and Sons. b) Optomechanical responses of a microflower structure fabricated from cholesteric liquid crystalline photonic photoresist through DLW method. Reprinted with permission from [120], Copyright 2020 American Chemical Society.

7.4 3D Print Multifunctional Liquid Crystal Elastomer Composites

Several attempts have been made to enhance the physical properties of liquid crystal polymeric materials through the development of LCE composites. These materials can also benefit from multifunctionality and multiresponsiveness for soft robotic application [122]. Liquid Metal (LM), ionic liquid, magnetic particles are among the most common fillers that have been utilized by researchers to design and fabricate LCE composites. Embedding highly conductive and intrinsically stretchable liquid metal (LM) into LCEs provides the opportunity to trigger the actuation locally through joule heating. As discussed in 2.4, Ambulo et. al. 4D printed LM\LCE composites through material extrusion. The fabricated structures were capable of both photothermal and electrothermal actuation. While we successfully

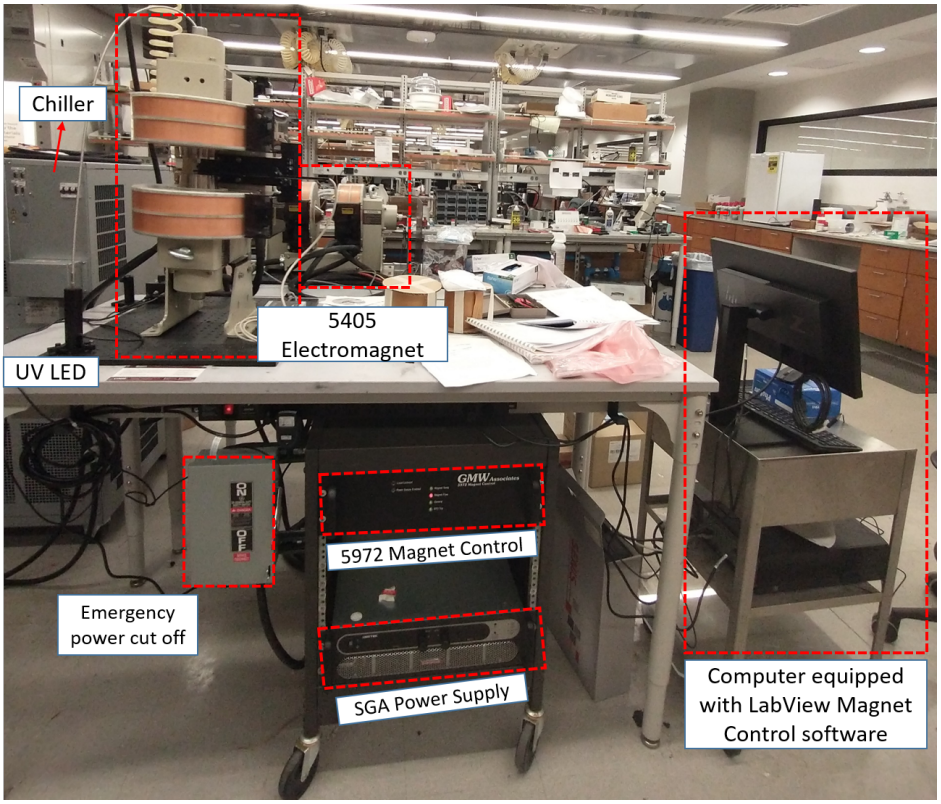

Figure 34: The vertical and horizontal closed-loop electromagnets setup, capable of generating high intensity magnetic fields up to 2 Tesla.

developed LM\LCE composites in our lab [123], these composites were not studied for the purpose of being fabricated through the proposed method in this work. Magnetic field has been utilized by many researchers as a remote stimulus. Complex, fast, precise, and instantaneous manipulation of magnetically responsive soft robots at different length-scales have been demonstrated. The inclusion of magnetic particles into LCE matrix can offer additional stimuli, magnetic fields, to LCE material and expand the deformation modes and applications in soft robotics [124]. The electric actuation can also become possible through the incorporation of ionic liquids and development of ionic liquid crystal elastomers (iLCEs) [125]. Utilizing the new magnetic setup we can explore the effect of LM, magnetic dopant, and ionic liquid concentration on the critical field. Once we determine the optimal compositions for each case, novel multifunctional freeforms can be developed through the presented voxel-by-voxel fabrication method.

7.5 Self-sensing & Self-regulation

Kotikian et al. exploited the change of resistance in LM due to shape change during the actuation to demonstrate self-sensing [70]. Through integration of a PID control system, an innervated LCE actuator with self-regulation capability was developed. After developing a new iLCE actuator, repeatable change of resistance (through the thickness) with small hysteresis effect in response to temperature variation was detected (Figure 35). This finding provides the opportunity to develop soft actuators with closed-loop control systems with applications in autonomous soft robots.

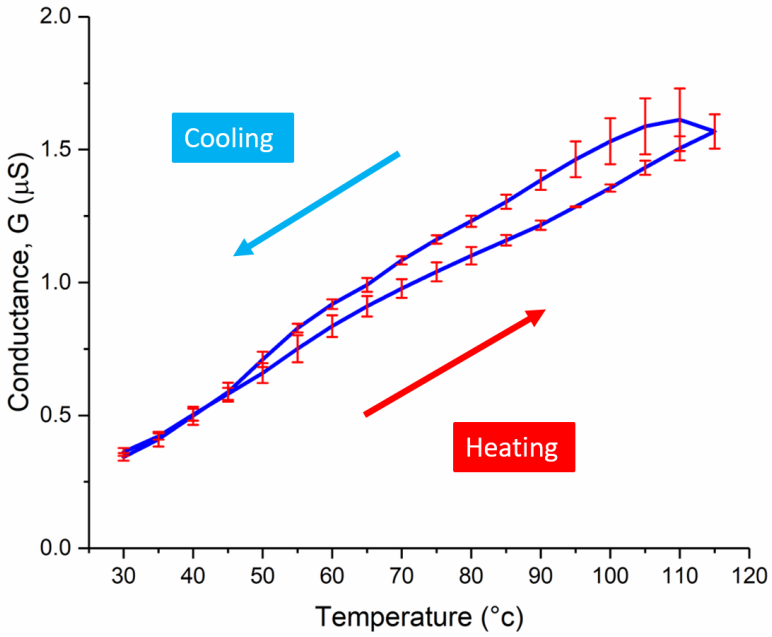

Figure 35: Resistance of iLCE film as a function of temperature. The data was calculated from the average of 3 cycles (first cycle was eliminated).

Appendix A

Publications

A.1 Peer Reviewed Journal Publications

Gao, J., Clement, A., **Tabrizi, M.** and Shankar, M.R., 2021. Molecularly Directed, Geometrically Latched, Impulsive Actuation Powers Sub-Gram Scale Motility. Advanced Materials Technologies, p.2100979.

Martinez, A., Clement, J. A., Gao, J., Kocherzat, J., **Tabrizi, M.**, Shankar, M.R., 2020. Thermomechanically Active Electrodes Power Work-Dense Soft Actuators. Soft Matter, 17(6), pp.1521-1529.

Haque, A.T., Tutika, R., Gao, M., Martinez, A., Mills, J.M., Clement, J.A., Gao, J., **Tabrizi, M.**, Shankar, M.R., Pei, Q. and Bartlett, M.D., 2020. Conductive liquid metal elastomer thin films with multifunctional electro-mechanical properties. Multifunctional Materials, 3(4), p.044001.

Tabrizi, M., Ware, T.H. and Shankar, M.R., 2019. Voxelated Molecular Patterning in Three-Dimensional Freeforms. ACS applied materials & interfaces, 11(31), pp.28236-28245.

A.2 Patent

M. Ravi Shankar, **M. Tabrizi**, Taylor H. Ware, 2019. "Voxelated molecular patterning in 3-dimensional freeforms", World pending patent, application number: WO2021055063A3.

A.3 Working Papers

Tabrizi, M., Babaei, M., Martinez, A., Clement, J. A., Gao, J., Ware, T.H. and Shankar, M.R., Three-dimensional Blueprinting of Molecular Patterns in Liquid Crystalline Elastomers.

Clement, J. A., **Tabrizi, M.** and Shankar, M.R., Molecularly Ordered Polyionic Actuator.

Tabrizi, M., Zubritskaya, I., Ji, A., Clement, J. A., Brongersma, M.L., and Shankar, M.R., Ordering in nanostructured thin films of a liquid crystalline main chain polymer.

A.4 Conference Presentations

Tabrizi, M., Ware, T.H. and Shankar, M.R. *"Voxelated Molecular Patterning in 3- Dimensional Freeforms"*, Materials Research Society Conference (MRS), Boston, Massachusettts, 2019.

Tabrizi, M., Ware, T.H. and Shankar, M.R. *"Voxelated Molecular Patterning in 3- Dimensional Freeforms"*, International Mechanical Engineering Congress & Exposition (IMECE). Salt Lake City, UT, 2019.

Tabrizi, M., Saed, M., Ware, T.H. and Shankar, M.R. *"3D printing of molecularly ordered heterogeneous active matter"*, International Mechanical Engineering Congress & Exposition (IMECE). Pittsburgh, PA, 2018.

Appendix B

Supporting Information

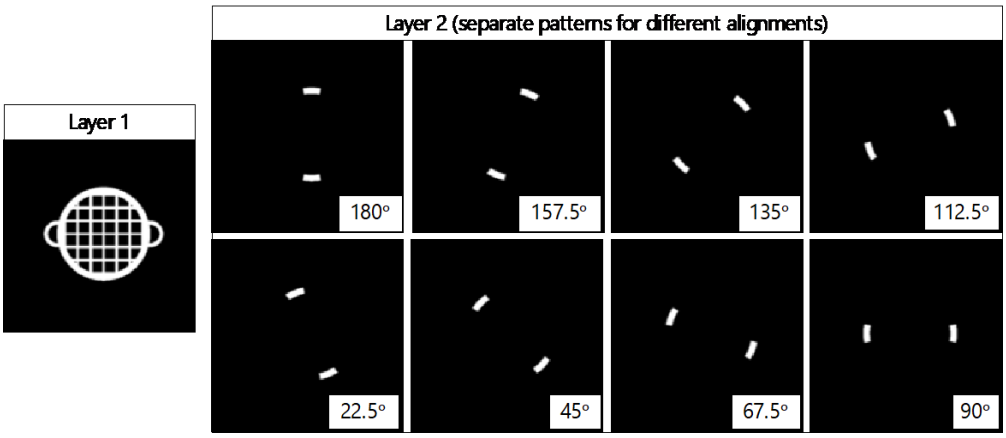

Figure 36: Black and white 2D patterns used for fabricating the bilayer basket (Figure 3). The azimuthal molecular orientation was encoded by breaking the ring into 16 different segments and 8 different molecular alignments. Potentially, the accuracy can be increased by segmenting the pattern into smaller sections. The magnetic field direction for each pattern (two segments) are noted in the insets [92].

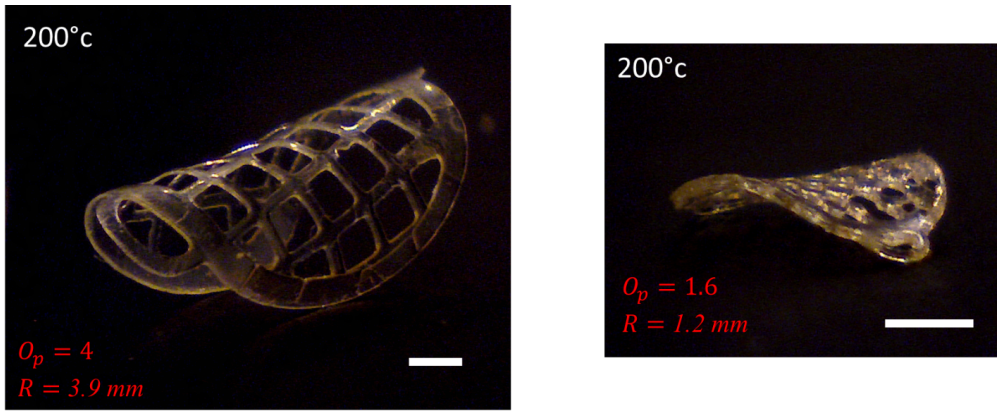

Figure 37: Overcurvature driven transformation of the basket-like geometries due to thermal actuation. A range of overcurvature values can be accessed by varying the radius of the azimuthally-oriented pattern in the prior flat state. (scale bars = 1 mm) [92].

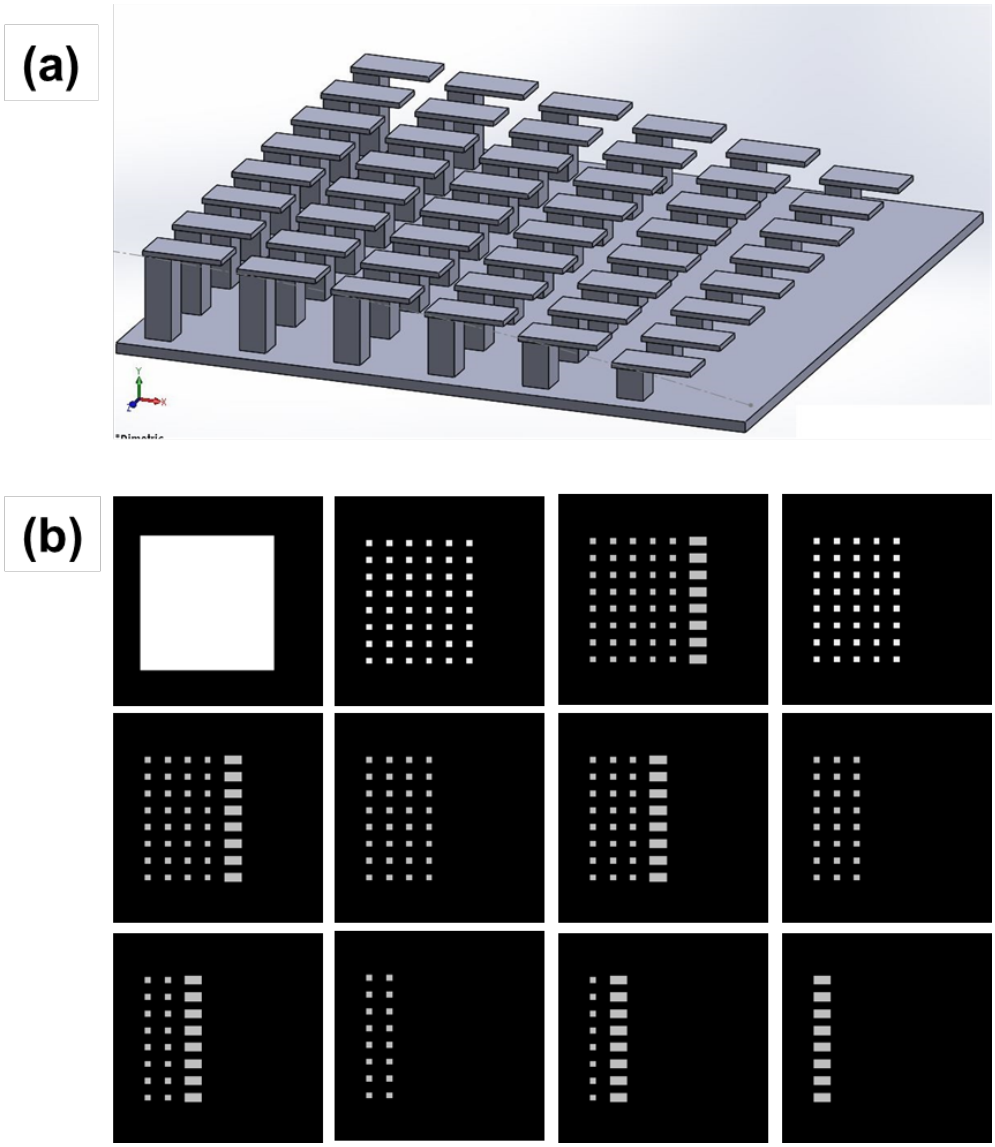

Figure 38: (a) Three-dimensional CAD model and (b) patterns used for making the array of overhanging cantilevers [92].

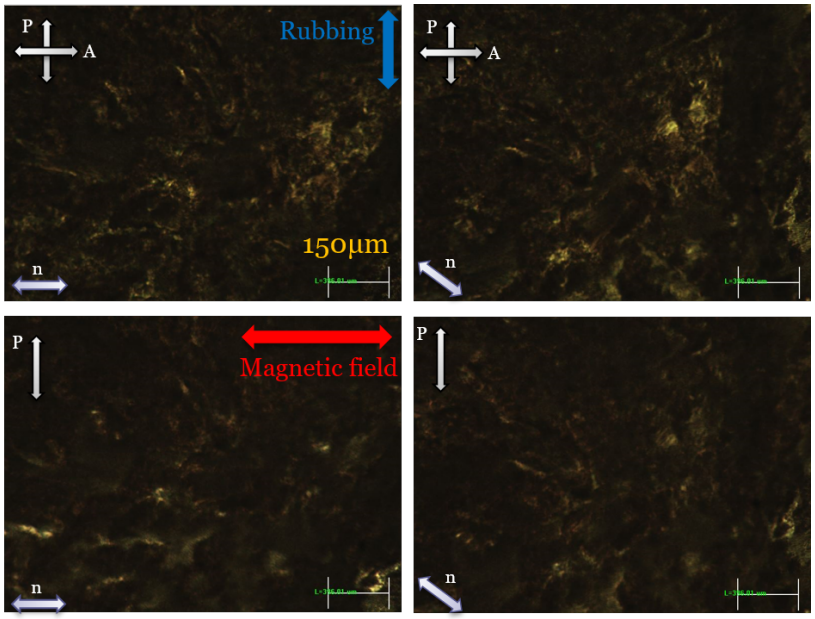

Figure 39: Crossed and parallel POM images of a 50 μm thick LCE fabricated through two-step Michael-addition method. The material (in oligomeric state) was fully polymerized at 55°C in presence of a 300 mT magnetic field and strong surface anchoring (rubbed elvamide) was applied on one side. This data demonstrates the inadequacy of 300 mT external magnetic field (as well as elvamide surface anchoring) in controlling the molecular orientation through this method (Section 6.1).

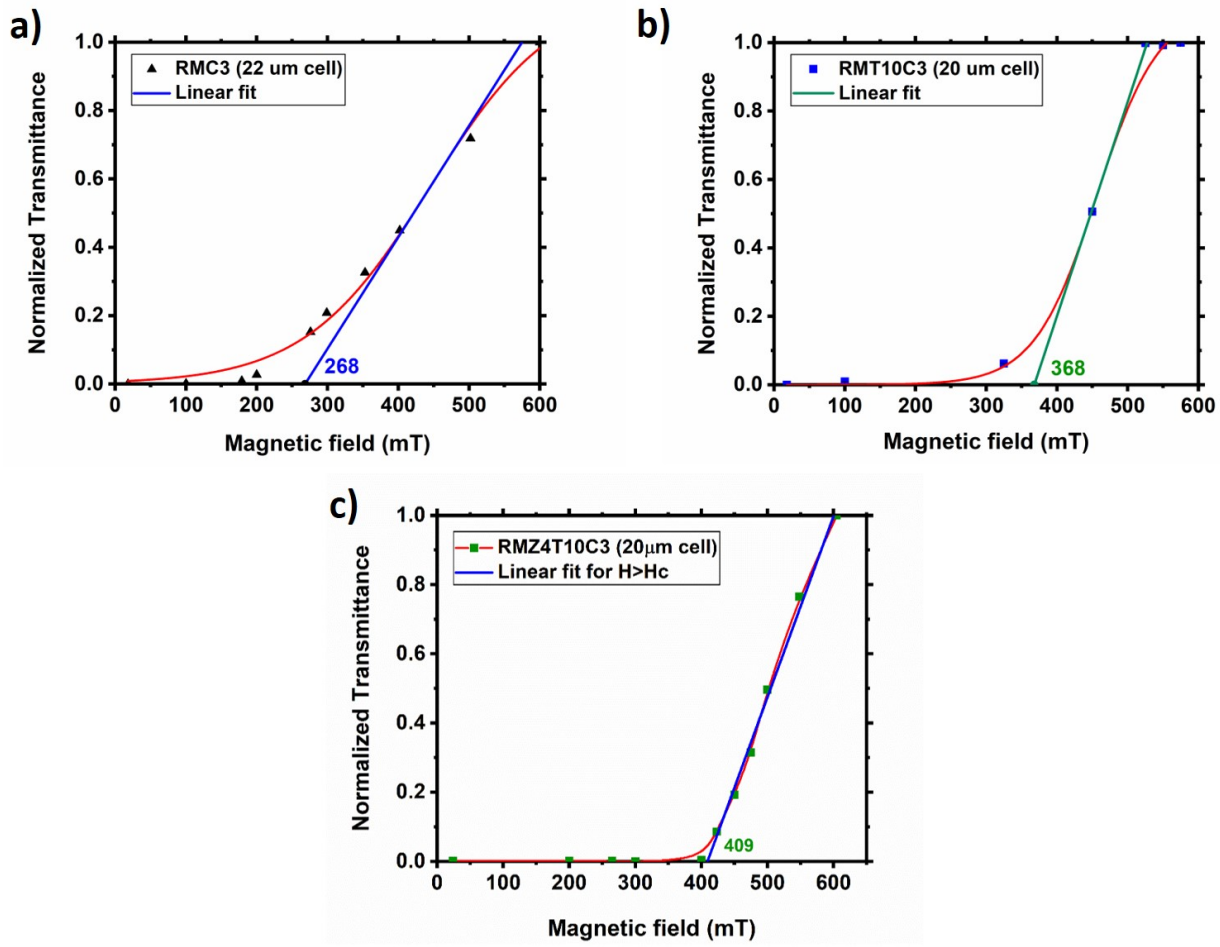

Figure 40: Influence of chain transfer agent, thiol chain-extender, and azobenzene dye on critical magnetic field. The threshold values were determined through linear fitting. a) RMC3 mixture in a 22 μm cell. b) RMT10C3 mixture in a 20 μm cell. c) RMZ4T10C3 mixture in a 20 μm cell.

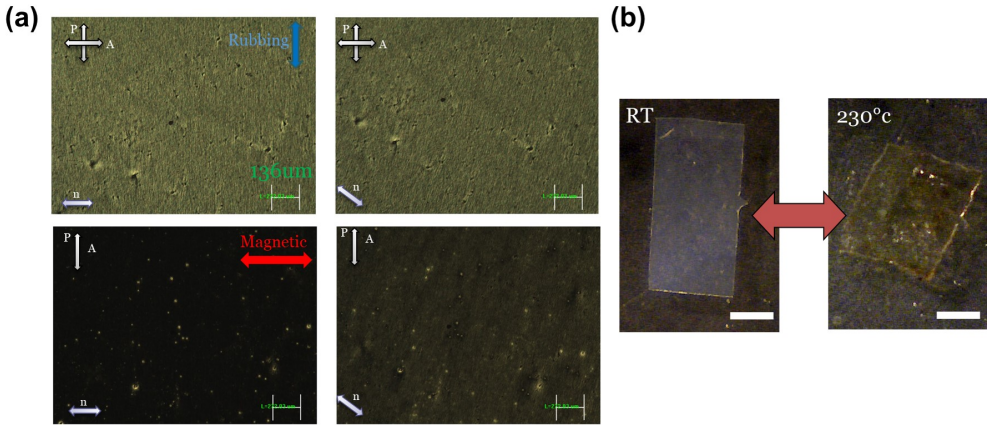

Figure 41: a) POM images of the polymerized sample (RMT10C3 composition) that confirm the molecular order at 0° and 45° under parallel and crossed polarizer (P) and analyzer (A)) b) Reversible 30% strain thermal actuation (scale bars = 1 mm).

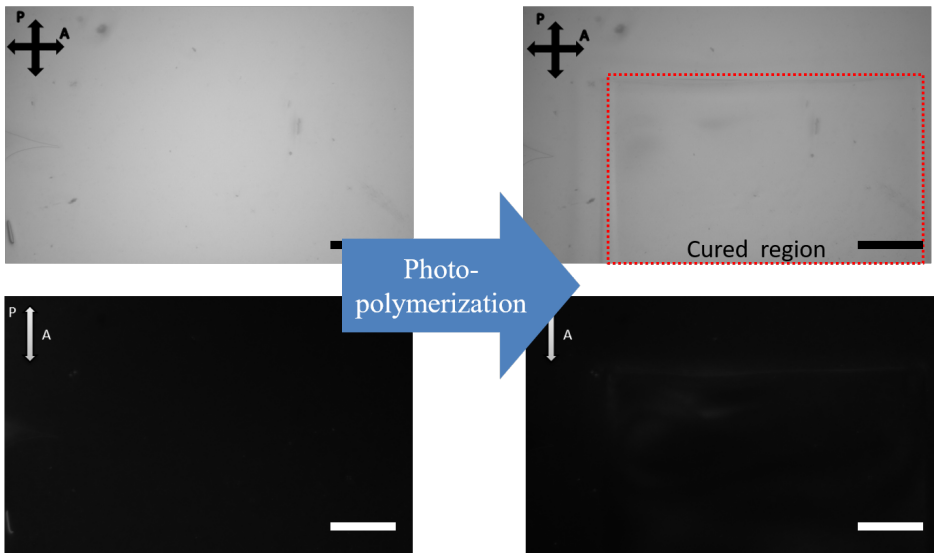

Figure 42: a) POM images of the polymerized sample that confirm the molecular order at 0° and 45° under parallel and crossed polarizer (P) and analyzer (A)) b) Reversible 27% strain thermal actuation (scale bars = 1 mm).

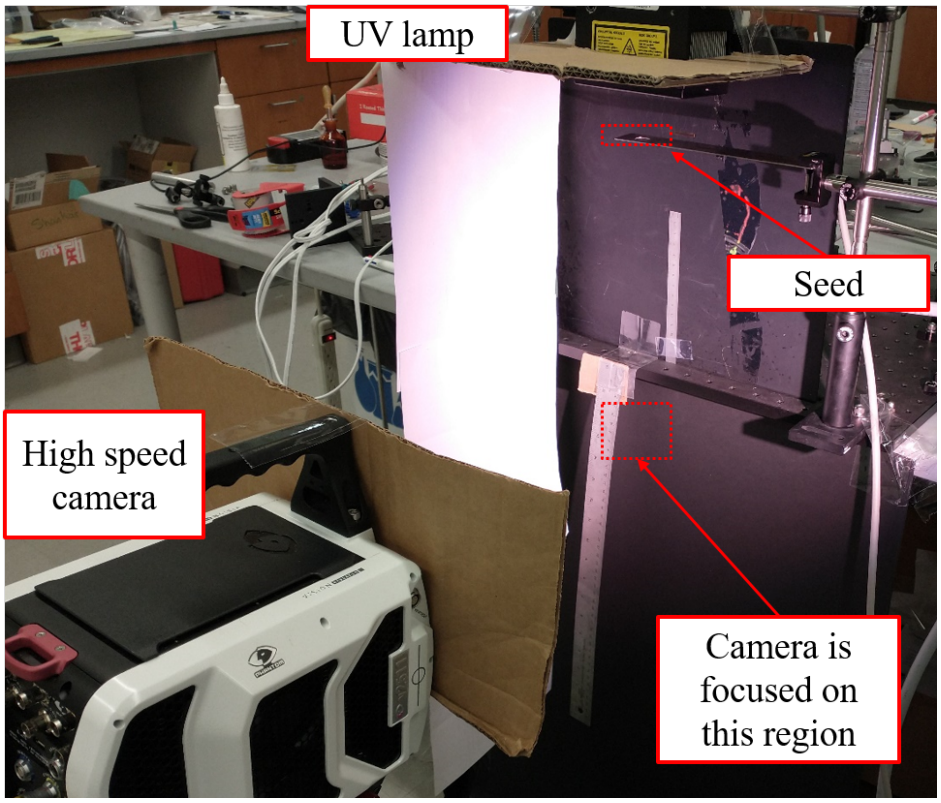

Figure 43: The setup for studying the flight dynamics of the printed LCE microflier in the presence and absence of UV light. The microflier was dropped from the sample location after 1 minute of UV exposure. The fall was captured at 25 cm distance from the dropping point by a high speed video camera at 5000 fps rate.

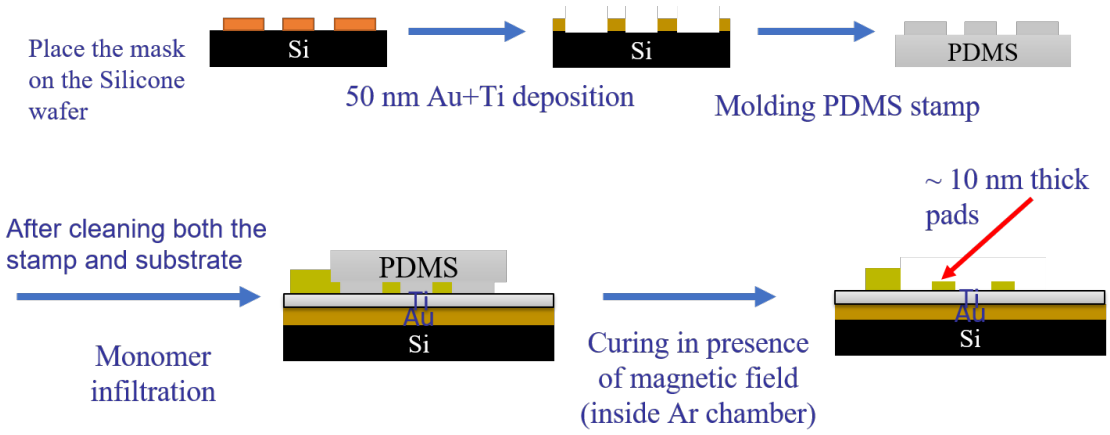

Figure 44: Soft lithography process steps for fabrication of ultrathin LCE films.

Bibliography

[1] Michael Wehner, Ryan L Truby, Daniel J Fitzgerald, Bobak Mosadegh, George M Whitesides, Jennifer A Lewis, and Robert J Wood. An integrated design and fabrication strategy for entirely soft, autonomous robots. *Nature*, 536(7617):451–455, 2016.

[2] Tian Chen, Osama R Bilal, Kristina Shea, and Chiara Daraio. Harnessing bistability for directional propulsion of soft, untethered robots. *Proceedings of the National Academy of Sciences*, 115(22):5698–5702, 2018.

[3] Yoonho Kim, Hyunwoo Yuk, Ruike Zhao, Shawn A Chester, and Xuanhe Zhao. Printing ferromagnetic domains for untethered fast-transforming soft materials. *Nature*, 558(7709):274–279, 2018.

[4] A Sydney Gladman, Elisabetta A Matsumoto, Ralph G Nuzzo, L Mahadevan, and Jennifer A Lewis. Biomimetic 4d printing. *Nature materials*, 15(4):413–418, 2016.

[5] TH Ware and TJ White. Programmed liquid crystal elastomers with tunable actuation strain. *Polymer Chemistry*, 6(26):4835–4844, 2015.

[6] Jürgen Küpfer and Heino Finkelmann. Nematic liquid single crystal elastomers. *Die Makromolekulare Chemie, Rapid Communications*, 12(12):717–726, 1991.

[7] Hyun Kim, Jennifer M Boothby, Sarvesh Ramachandran, Cameron D Lee, and Taylor H Ware. Tough, shape-changing materials: crystallized liquid crystal elastomers. *Macromolecules*, 50(11):4267–4275, 2017.

[8] Timothy J White and Dirk J Broer. Programmable and adaptive mechanics with liquid crystal polymer networks and elastomers. *Nature materials*, 14(11):1087–1098, 2015.

[9] Joselle M McCracken, Brian R Donovan, and Timothy J White. Materials as machines. *Advanced Materials*, page 1906564, 2020.

[10] Ping Xie and Rongben Zhang. Liquid crystal elastomers, networks and gels: advanced smart materials. *Journal of Materials Chemistry*, 15(26):2529–2550, 2005.

[11] Kenji Urayama. Selected issues in liquid crystal elastomers and gels. *Macromolecules*, 40(7):2277–2288, 2007.

[12] Kenji Urayama. Electro-opto-mechanical effects in swollen nematic elastomers. In *Liquid Crystal Elastomers: Materials and Applications*, pages 119–145. Springer, 2010.

[13] Kenji Urayama, Seiji Honda, and Toshikazu Takigawa. Deformation coupled to director rotation in swollen nematic elastomers under electric fields. *Macromolecules*, 39(5):1943–1949, 2006.

[14] Akihiko Matsuyama and Tadaya Kato. Discontinuous elongation of nematic gels by a magnetic field. *Physical Review E*, 64(1):010701, 2001.

[15] Lindsey Hines, Kirstin Petersen, Guo Zhan Lum, and Metin Sitti. Soft actuators for small-scale robotics. *Advanced materials*, 29(13):1603483, 2017.

[16] Kenneth D Harris, Cees WM Bastiaansen, and DJ Broer. Physical properties of anisotropically swelling hydrogen-bonded liquid crystal polymer actuators. *Journal of microelectromechanical systems*, 16(2):480–488, 2007.

[17] Donald L Thomsen, Patrick Keller, Jawad Naciri, Roger Pink, Hong Jeon, Devanand Shenoy, and Banahalli R Ratna. Liquid crystal elastomers with mechanical properties of a muscle. *Macromolecules*, 34(17):5868–5875, 2001.

[18] Hendrik Wermter and Heino Finkelmann. Liquid crystalline elastomers as artificial muscles. *e-Polymers*, 1(1), 2001.

[19] CL Oosten. v.; bastiaansen, cwm; broer, dj. *Nat. Mater*, 8:677–682, 2009.

[20] Matthew Hendrikx, Burcu Sırma, Albertus PHJ Schenning, Danqing Liu, and Dirk J Broer. Compliance-mediated topographic oscillation of polarized light triggered liquid crystal coating. *Advanced Materials Interfaces*, 5(20):1800810, 2018.

[21] Taylor H Ware, Michael E McConney, Jeong Jae Wie, Vincent P Tondiglia, and Timothy J White. Voxelated liquid crystal elastomers. *Science*, 347(6225):982–984, 2015.

[22] CL Van Oosten, KD Harris, CWM Bastiaansen, and DJ Broer. Glassy photomechanical liquid-crystal network actuators for microscale devices. *The European Physical Journal E*, 23(3):329–336, 2007.

[23] Chaolei Huang, Jiu-an Lv, Xiaojun Tian, Yuechao Wang, Yanlei Yu, and Jie Liu. Miniaturized swimming soft robot with complex movement actuated and controlled by remote light signals. *Scientific reports*, 5(1):1–8, 2015.

[24] Stefan Schuhladen, Falko Preller, Richard Rix, Sebastian Petsch, Rudolf Zentel, and Hans Zappe. Iris-like tunable aperture employing liquid-crystal elastomers. *Advanced materials*, 26(42):7247–7251, 2014.

[25] Yuxing Yao, James T Waters, Anna V Shneidman, Jiaxi Cui, Xiaoguang Wang, Nikolaj K Mandsberg, Shucong Li, Anna C Balazs, and Joanna Aizenberg. Multiresponsive polymeric microstructures with encoded predetermined and self-regulated deformability. *Proceedings of the National Academy of Sciences*, 115(51):12950–12955, 2018.

[26] Cedric P Ambulo, Julia J Burroughs, Jennifer M Boothby, Hyun Kim, M Ravi Shankar, and Taylor H Ware. Four-dimensional printing of liquid crystal elastomers. *ACS applied materials & interfaces*, 9(42):37332–37339, 2017.

[27] Arda Kotikian, Ryan L Truby, John William Boley, Timothy J White, and Jennifer A Lewis. 3d printing of liquid crystal elastomeric actuators with spatially programed nematic order. *Advanced Materials*, 30(10):1706164, 2018.

[28] María López-Valdeolivas, Danqing Liu, Dick Jan Broer, and Carlos Sánchez-Somolinos. 4d printed actuators with soft-robotic functions. *Macromolecular rapid communications*, 39(5):1700710, 2018.

[29] Silvan Gantenbein, Kunal Masania, Wilhelm Woigk, Jens PW Sesseg, Theo A Tervoort, and André R Studart. Three-dimensional printing of hierarchical liquid-crystal-polymer structures. *Nature*, 561(7722):226–230, 2018.

[30] Mohand O Saed, Cedric P Ambulo, Hyun Kim, Rohit De, Vyom Raval, Kyle Searles, Danyal A Siddiqui, John Michael O Cue, Mihaela C Stefan, M Ravi Shankar, et al. Molecularly-engineered, 4d-printed liquid crystal elastomer actuators. *Advanced Functional Materials*, 29(3):1806412, 2019.

[31] Devin J Roach, Xiao Kuang, Chao Yuan, Kaijuan Chen, and H Jerry Qi. Novel ink for ambient condition printing of liquid crystal elastomers for 4d printing. *Smart Materials and Structures*, 27(12):125011, 2018.

[32] Cyrus Mostajeran, Mark Warner, Taylor H Ware, and Timothy J White. Encoding gaussian curvature in glassy and elastomeric liquid crystal solids. *Proceedings of the Royal Society A: Mathematical, Physical and Engineering Sciences*, 472(2189):20160112, 2016.

[33] Tyler Guin, Michael J Settle, Benjamin A Kowalski, Anesia D Auguste, Richard V Beblo, Gregory W Reich, and Timothy J White. Layered liquid crystal elastomer actuators. *Nature communications*, 9(1):1–7, 2018.

[34] M Ravi Shankar, Matthew L Smith, Vincent P Tondiglia, Kyung Min Lee, Michael E McConney, David H Wang, Loon-Seng Tan, and Timothy J White. Contactless, photoinitiated snap-through in azobenzene-functionalized polymers. *Proceedings of the National Academy of Sciences*, 110(47):18792–18797, 2013.

[35] Bernard D Coleman and David Swigon. Theory of supercoiled elastic rings with self-contact and its application to dna plasmids. *Journal of elasticity and the physical science of solids*, 60(3):173, 2000.

[36] AN Gent and K-C Hua. Torsional instability of stretched rubber cylinders. *International Journal of Non-Linear Mechanics*, 39(3):483–489, 2004.

[37] AD Norman, KA Seffen, and SD Guest. Morphing of curved corrugated shells. *International Journal of Solids and Structures*, 46(7-8):1624–1633, 2009.

[38] Athene Margaret Donald, Alan H Windle, and Simon Hanna. *Liquid crystalline polymers*. Cambridge University Press, 2006.

[39] Pierre-Gilles De Gennes and Jacques Prost. *The physics of liquid crystals*, volume 83. Oxford university press, 1993.

[40] MI Boamfă, K Viertler, Alf Wewerka, Franz Stelzer, PCM Christianen, and JC Maan. Mesogene-polymer backbone coupling in side-chain polymer liquid crystals, studied by high magnetic-field-induced alignment. *Physical review letters*, 90(2):025501, 2003.

[41] Vsevolod Fréedericksz and V Zolina. Forces causing the orientation of an anisotropic liquid. *Transactions of the Faraday Society*, 29(140):919–930, 1933.

[42] S. Chandrasekhar. *Liquid crystals*. Cambridge University Press, Cambridge [England];New York, NY, USA, 2 edition, 1992.

[43] Paul R Gerber and Martin Schadt. On the measurement of elastic constants in nematic liquid crystals: comparison of different methods. *Zeitschrift für Naturforschung A*, 35(10):1036–1044, 1980.

[44] Hans Gruler, Terry J Scheffer, and Gerhard Meier. Elastic constants of nematic liquid crystals. *Zeitschrift für Naturforschung A*, 27(6):966—-976, 1972.

[45] NV Madhusudana and R Pratibha. Elasticity and orientational order in some cyanobiphenyls: Part IV. Reanalysis of the data. *MOL CRYST LIQ CRYST*, 89(N 1-4):249–257, 1982.

[46] Shin-Tson Wu, Willis H. Smith, and Anna M. Lackner. Diamagnetic Anisotropy Measurements of Nematic Liquid Crystals. *Molecular Crystals and Liquid Crystals*, 140(2-4):83–93, November 1986.

[47] F. Brochard. Backflow Effects in Nematic Liquid Crystals. *Molecular Crystals and Liquid Crystals*, 23(1-2):51–58, January 1973.

[48] J. S. Moore and S. I. Stupp. Orientation dynamics of main-chain liquid crystal polymers. 2. Structure and kinetics in a magnetic field. *Macromolecules*, 20(2):282–293, March 1987.

[49] Afzana Anwer and Alan H. Windle. Orientation kinetics of thermotropic main-chain liquid-crystalline polymers in a magnetic field. *Polymer*, 32(1):103–108, January 1991.

[50] Jungwoo Shin, Minjee Kang, Tsunghan Tsai, Cecilia Leal, Paul V. Braun, and David G. Cahill. Thermally Functional Liquid Crystal Networks by Magnetic Field Driven Molecular Orientation. *ACS Macro Letters*, 5(8):955–960, August 2016.

[51] Laurence Pottié, France Costa-Torro, Martine Tessier, Patrick Davidson, and Alain Fradet. Investigation of anisotropic epoxy–amine thermosets synthesised in a magnetic field. *Liquid Crystals*, 35(8):913–924, August 2008.

[52] Sonal Dey, Dena Agra-Kooijman, Wanting Ren, Philip McMullan, Anselm Griffin, and Satyendra Kumar. Soft Elasticity in Main Chain Liquid Crystal Elastomers. *Crystals*, 3(2):363–390, June 2013.

[53] Hong Yang, Axel Buguin, Jean-Marie Taulemesse, Kosuke Kaneko, Stéphane Meéry, Anne Bergeret, and Patrick Keller. Micron-Sized Main-Chain Liquid Crystalline Elastomer Actuators with Ultralarge Amplitude Contractions. *Journal of the American Chemical Society*, 131(41):15000–15004, October 2009.

[54] H. T. A. Wilderbeek, M. G. M. van der Meer, M. A. G. Jansen, L. Nelissen, H. R. Fischer, J. J. G. S. van Es, C. W. M. Bastiaansen, J. Lub, and D. J. Broer. Synthesis and properties of phenyl benzoate-based and biphenyl-based liquid crystalline thiolene monomers. *Liquid Crystals*, 30(1):93–108, January 2003.

[55] Bin Ni, Gaoyu Liu, Mengxue Zhang, Patrick Keller, Michael Tatoulian, and Min-Hui Li. Large-size honeycomb-shaped and iris-like liquid crystal elastomer actuators. *CCS Chemistry*, pages 1081–1088, 2021.

[56] Bin Ni, Gaoyu Liu, Mengxue Zhang, Michael Tatoulian, Patrick Keller, and Min-Hui Li. Customizable sophisticated three-dimensional shape changes of large-size liquid crystal elastomer actuators. *ACS Applied Materials & Interfaces*, 13(45):54439–54446, 2021.

[57] Taylor H Ware, Zachary P Perry, Claire M Middleton, Scott T Iacono, and Timothy J White. Programmable liquid crystal elastomers prepared by thiol–ene photopolymerization. *ACS Macro Letters*, 4(9):942–946, 2015.

[58] P. M S Roberts, G. R Mitchell, and F. J Davis. Memory Effects in Monodomain Liquid Crystal Elastomers Produced in Magnetic Fields. *Molecular Crystals and Liquid Crystals Science and Technology. Section A. Molecular Crystals and Liquid Crystals*, 299(1):223–228, June 1997.

[59] Axel Buguin, Min-Hui Li, Pascal Silberzan, Benoit Ladoux, and Patrick Keller. Micro-Actuators: When Artificial Muscles Made of Nematic Liquid Crystal Elastomers Meet Soft Lithography. *Journal of the American Chemical Society*, 128(4):1088–1089, February 2006.

[60] Jiaxi Cui, Dirk-Michael Drotlef, Iñigo Larraza, Juan P. Fernández-Blázquez, Luciano F. Boesel, Christian Ohm, Markus Mezger, Rudolf Zentel, and Aránzazu del Campo. Bioinspired Actuated Adhesive Patterns of Liquid Crystalline Elastomers. *Advanced Materials*, 24(34):4601–4604, September 2012.

[61] Zi Liang Wu, Axel Buguin, Hong Yang, Jean-Marie Taulemesse, Nicolas Le Moigne, Anne Bergeret, Xiaogong Wang, and Patrick Keller. Microstructured Nematic Liq-

uid Crystalline Elastomer Surfaces with Switchable Wetting Properties. *Advanced Functional Materials*, 23(24):3070–3076, June 2013.

[62] M.-H. Li, P. Keller, J. Yang, and P.-A. Albouy. An Artificial Muscle with Lamellar Structure Based on a Nematic Triblock Copolymer. *Advanced Materials*, 16(21):1922–1925, November 2004.

[63] James T. Waters, Shucong Li, Yuxing Yao, Michael M. Lerch, Michael Aizenberg, Joanna Aizenberg, and Anna C. Balazs. Twist again: Dynamically and reversibly controllable chirality in liquid crystalline elastomer microposts. *Science Advances*, 6(13):eaay5349, March 2020.

[64] Xiaojie Qian, Qiaomei Chen, Yang Yang, Yanshuang Xu, Zhen Li, Zhenhua Wang, Yahe Wu, Yen Wei, and Yan Ji. Untethered Recyclable Tubular Actuators with Versatile Locomotion for Soft Continuum Robots. *Advanced Materials*, 30(29):1801103, July 2018.

[65] Shannon E. Bakarich, Robert Gorkin, Marc in het Panhuis, and Geoffrey M. Spinks. 4D Printing with Mechanically Robust, Thermally Actuating Hydrogels. *Macromolecular Rapid Communications*, 36(12):1211–1217, June 2015.

[66] Jennifer E. Taylor, Angel Romo-Uribe, and Matthew R. Libera. Bimodal Orientation Defects in Main-Chain Thermotropic Liquid Crystalline Polymer Fibers. *Macromolecules*, 35(5):1751–1756, February 2002.

[67] Simon Krause, Roland Dersch, Joachim H. Wendorff, and Heino Finkelmann. Photocrosslinkable Liquid Crystal Main-Chain Polymers: Thin Films and Electrospinning. *Macromolecular Rapid Communications*, 28(21):2062–2068, November 2007.

[68] Lorena Ceamanos, Zehra Kahveci, María López-Valdeolivas, Danqing Liu, Dirk Jan Broer, and Carlos Sánchez-Somolinos. Four-dimensional printed liquid crystalline elastomer actuators with fast photoinduced mechanical response toward light-driven robotic functions. *ACS Applied Materials & Interfaces*, 12(39):44195–44204, 2020.

[69] Arda Kotikian, Connor McMahan, Emily C. Davidson, Jalilah M. Muhammad, Robert D. Weeks, Chiara Daraio, and Jennifer A. Lewis. Untethered soft robotic matter with passive control of shape morphing and propulsion. *Science Robotics*, 4(33):eaax7044, August 2019.

[70] Arda Kotikian, Javier M Morales, Aric Lu, Jochen Mueller, Zoey S Davidson, J William Boley, and Jennifer A Lewis. Innervated, self-sensing liquid crystal elastomer actuators with closed loop control. *Advanced Materials*, 33(27):2101814, 2021.

[71] Cedric P Ambulo, Michael J Ford, Kyle Searles, Carmel Majidi, and Taylor H Ware. 4d-printable liquid metal–liquid crystal elastomer composites. *ACS applied materials & interfaces*, 13(11):12805–12813, 2020.

[72] Luquan Ren, Bingqian Li, Yulin He, Zhengyi Song, Xueli Zhou, Qingping Liu, and Lei Ren. Programming Shape-Morphing Behavior of Liquid Crystal Elastomers via Parameter-Encoded 4D Printing. *ACS Applied Materials & Interfaces*, 12(13):15562–15572, April 2020.

[73] Zijun Wang, Nicholas Boechler, and Shengqiang Cai. Anisotropic mechanical behavior of 3d printed liquid crystal elastomer. *Additive Manufacturing*, page 102678, 2022.

[74] Zijun Wang, Zhijian Wang, Yue Zheng, Qiguang He, Yang Wang, and Shengqiang Cai. Three-dimensional printing of functionally graded liquid crystal elastomer. *Science advances*, 6(39):eabc0034, 2020.

[75] Chun Zhang, Xili Lu, Guoxia Fei, Zhanhua Wang, Hesheng Xia, and Yue Zhao. 4D Printing of a Liquid Crystal Elastomer with a Controllable Orientation Gradient. *ACS Applied Materials & Interfaces*, 11(47):44774–44782, November 2019.

[76] Brian H. Cumpston, Sundaravel P. Ananthavel, Stephen Barlow, Daniel L. Dyer, Jeffrey E. Ehrlich, Lael L. Erskine, Ahmed A. Heikal, Stephen M. Kuebler, I.-Y. Sandy Lee, Dianne McCord-Maughon, Jinqui Qin, Harald Röckel, Mariacristina Rumi, Xiang-Li Wu, Seth R. Marder, and Joseph W. Perry. Two-photon polymerization initiators for three-dimensional optical data storage and microfabrication. *Nature*, 398(6722):51–54, March 1999.

[77] Natalia A. Bakhtina, Ute Loeffelmann, Neil MacKinnon, and Jan G. Korvink. Two-Photon Nanolithography Enhances the Performance of an Ionic Liquid-Polymer Composite Sensor. *Advanced Functional Materials*, 25(11):1683–1693, March 2015.

[78] Hao Zeng, Daniele Martella, Piotr Wasylczyk, Giacomo Cerretti, Jean-Christophe Gomez Lavocat, Chih-Hua Ho, Camilla Parmeggiani, and Diederik Sybolt Wiersma. High-Resolution 3D Direct Laser Writing for Liquid-Crystalline Elastomer Microstructures. *Advanced Materials*, 26(15):2319–2322, April 2014.

[79] Hao Zeng, Piotr Wasylczyk, Camilla Parmeggiani, Daniele Martella, Matteo Burresi, and Diederik Sybolt Wiersma. Light-Fueled Microscopic Walkers. *Advanced Materials*, 27(26):3883–3887, July 2015.

[80] Joselle M McCracken, Vincent P Tondiglia, Anesia D Auguste, Nicholas P Godman, Brian R Donovan, Brody N Bagnall, Hayden E Fowler, Chance M Baxter, Valentina Matavulj, John D Berrigan, et al. Microstructured photopolymerization of liquid crystalline elastomers in oxygen-rich environments. *Advanced Functional Materials*, 29(40):1903761, 2019.

[81] Yubing Guo, Hamed Shahsavan, and Metin Sitti. 3d microstructures of liquid crystal networks with programmed voxelated director fields. *Advanced Materials*, 32(38):2002753, 2020.

[82] Yubing Guo, Jiachen Zhang, Wenqi Hu, Muhammad Turab Ali Khan, and Metin Sitti. Shape-programmable liquid crystal elastomer structures with arbitrary three-dimensional director fields and geometries. *Nature communications*, 12(1):1–9, 2021.

[83] Alexander Münchinger, Vincent Hahn, Dominik Beutel, Simon Woska, Joël Monti, Carsten Rockstuhl, Eva Blasco, and Martin Wegener. Multi-photon 4d printing of complex liquid crystalline microstructures by in situ alignment using electric fields. *Advanced Materials Technologies*, 7(1):2100944, 2022.

[84] Marco Carlotti, Omar Tricinci, Frank den Hoed, Stefano Palagi, and Virgilio Mattoli. Direct laser writing of liquid crystal elastomers oriented by a horizontal electric field. *Open Research Europe*, 1:129, 2021.

[85] Nicholas A Traugutt, Devesh Mistry, Chaoqian Luo, Kai Yu, Qi Ge, and Christopher M Yakacki. Liquid-crystal-elastomer-based dissipative structures by digital light processing 3d printing. *Advanced Materials*, 32(28):2000797, 2020.

[86] Shuo Li, Hedan Bai, Zheng Liu, Xinyue Zhang, Chuqi Huang, Lennard W Wiesner, Meredith Silberstein, and Robert F Shepherd. Digital light processing of liquid crystal elastomers for self-sensing artificial muscles. *Science Advances*, 7(30):eabg3677, 2021.

[87] Mengqi Fang, Tao Liu, Yang Xu, Binjie Jin, Ning Zheng, Yue Zhang, Qian Zhao, Zheng Jia, and Tao Xie. Ultrafast digital fabrication of designable architectured liquid crystalline elastomer. *Advanced Materials*, 33(52):2105597, 2021.

[88] Binjie Jin, Jiaqi Liu, Yunpeng Shi, Guancong Chen, Qian Zhao, and Shu Yang. Solvent-assisted 4d programming and reprogramming of liquid crystalline organogels. *Advanced Materials*, 34(5):2107855, 2022.

[89] Haiwei Chen, Ruidong Zhu, Jianxiong Zhu, and Shin-Tson Wu. A simple method to measure the twist elastic constant of a nematic liquid crystal. *Liquid Crystals*, 42(12):1738–1742, 2015.

[90] https://physlets.org/tracker/.

[91] Eisaku Iizuka. The Effects of Magnetic Fields on the Structure of Cholesteric Liquid Crystals of Polypeptides. *Polymer Journal*, 4(4):401–408, May 1973.

[92] Mohsen Tabrizi, Taylor H. Ware, and M. Ravi Shankar. Voxelated Molecular Patterning in Three-Dimensional Freeforms. *ACS Applied Materials & Interfaces*, 11(31):28236–28245, August 2019.

[93] Kyung Min Lee, Timothy J. Bunning, and Timothy J. White. Autonomous, Hands-Free Shape Memory in Glassy, Liquid Crystalline Polymer Networks. *Advanced Materials*, 24(21):2839–2843, June 2012.

[94] Paul Francis Jacobs. *Rapid prototyping & manufacturing: fundamentals of stereolithography*. Society of Manufacturing Engineers, 1992.

[95] Amir Skandani, J. Arul Clement, Stephanie Tristram-Nagle, and M. Ravi Shankar. Aliphatic flexible spacer length controls photomechanical response in compact, ordered liquid crystalline polymer networks. *Polymer*, 133:30–39, December 2017.

[96] Yanlei Yu, Makoto Nakano, Atsushi Shishido, Takeshi Shiono, and Tomiki Ikeda. Effect of cross-linking density on photoinduced bending behavior of oriented liquid-crystalline network films containing azobenzene. *Chemistry of materials*, 16(9):1637–1643, 2004.

[97] Pierre-Olivier Mouthuy, Michael Coulombier, Thomas Pardoen, Jean-Pierre Raskin, and Alain M Jonas. Overcurvature describes the buckling and folding of rings from curved origami to foldable tents. *Nature communications*, 3(1):1–8, 2012.

[98] Yanlei Yu, Makoto Nakano, and Tomiki Ikeda. Directed bending of a polymer film by light. *Nature*, 425(6954):145–145, 2003.

[99] Casper L Van Oosten, Cees WM Bastiaansen, and Dirk J Broer. Printed artificial cilia from liquid-crystal network actuators modularly driven by light. *Nature materials*, 8(8):677–682, 2009.

[100] Jaeho Choi, Wonhee Jo, Seung Yeol Lee, Yeon Sik Jung, Shin-Hyun Kim, and Hee-Tak Kim. Flexible and robust superomniphobic surfaces created by localized photofluidization of azopolymer pillars. *ACS nano*, 11(8):7821–7828, 2017.

[101] Stefano Palagi, Andrew G Mark, Shang Yik Reigh, Kai Melde, Tian Qiu, Hao Zeng, Camilla Parmeggiani, Daniele Martella, Alberto Sanchez-Castillo, Nadia Kapernaum, et al. Structured light enables biomimetic swimming and versatile locomotion of photoresponsive soft microrobots. *Nature materials*, 15(6):647–653, 2016.

[102] Yijie Jiang, Lucia M Korpas, and Jordan R Raney. Bifurcation-based embodied logic and autonomous actuation. *Nature communications*, 10(1):1–10, 2019.

[103] Hoon Yeub Jeong, Eunseo Lee, Sangho Ha, Namhun Kim, and Young Chul Jun. Multistable thermal actuators via multimaterial 4d printing. *Advanced Materials Technologies*, 4(3):1800495, 2019.

[104] Nicholas P. Godman, Benjamin A. Kowalski, Anesia D. Auguste, Hilmar Koerner, and Timothy J. White. Synthesis of Elastomeric Liquid Crystalline Polymer Networks via Chain Transfer. *ACS Macro Letters*, 6(11):1290–1295, November 2017.

[105] Allison K O'Brien, Neil B Cramer, and Christopher N Bowman. Oxygen inhibition in thiol–acrylate photopolymerizations. *Journal of Polymer Science Part A: Polymer Chemistry*, 44(6):2007–2014, 2006.

[106] Owies M Wani, Hao Zeng, and Arri Priimagi. A light-driven artificial flytrap. *Nature communications*, 8(1):1–7, 2017.

[107] Hao Zeng, Owies M Wani, Piotr Wasylczyk, and Arri Priimagi. Light-driven, caterpillar-inspired miniature inching robot. *Macromolecular rapid communications*, 39(1):1700224, 2018.

[108] Dario Floreano and Robert J Wood. Science, technology and the future of small autonomous drones. *nature*, 521(7553):460–466, 2015.

[109] E Farrell Helbling and Robert J Wood. A review of propulsion, power, and control architectures for insect-scale flapping-wing vehicles. *Applied Mechanics Reviews*, 70(1), 2018.

[110] Kevin Y Ma, Pakpong Chirarattananon, Sawyer B Fuller, and Robert J Wood. Controlled flight of a biologically inspired, insect-scale robot. *Science*, 340(6132):603–607, 2013.

[111] Noah T Jafferis, E Farrell Helbling, Michael Karpelson, and Robert J Wood. Untethered flight of an insect-sized flapping-wing microscale aerial vehicle. *Nature*, 570(7762):491–495, 2019.

[112] John Rogers, Bong Hoon Kim, Kan Li, Jin-Tae Kim, Yoonseok Park, Hokyung Jang, Xueju Wang, Zhaoqian Xie, Sang Won, Woo Jin Jang, et al. Three-dimensional electronic microfliers with designs inspired by wind-dispersed seeds. 2021.

[113] Ran Nathan, Gabriel G Katul, Henry S Horn, Suvi M Thomas, Ram Oren, Roni Avissar, Stephen W Pacala, and Simon A Levin. Mechanisms of long-distance dispersal of seeds by wind. *Nature*, 418(6896):409–413, 2002.

[114] David Lentink, William B Dickson, Johan L Van Leeuwen, and Michael H Dickinson. Leading-edge vortices elevate lift of autorotating plant seeds. *Science*, 324(5933):1438–1440, 2009.

[115] Eisaku Iizuka. The effects of magnetic fields on the structure of cholesteric liquid crystals of polypeptides. *Polymer Journal*, 4(4):401–408, 1973.

[116] Alexander Ryabchun and Alexey Bobrovsky. Cholesteric liquid crystal materials for tunable diffractive optics. *Advanced Optical Materials*, 6(15):1800335, 2018.

[117] G Durand, L Leger, F Rondelez, and M Veyssie. Magnetically induced cholesteric to nematic phase transition in liquid crystals. *Physical Review Letters*, 22(6):227, 1969.

[118] Sang Seok Lee, Hyeon Jin Seo, Yun Ho Kim, and Shin-Hyun Kim. Structural color palettes of core–shell photonic ink capsules containing cholesteric liquid crystals. *Advanced Materials*, 29(23):1606894, 2017.

[119] Nobuyuki Tamaoki. Cholesteric liquid crystals for color information technology. *Advanced Materials*, 13(15):1135–1147, 2001.

[120] Marc Del Pozo, Colm Delaney, Cees WM Bastiaansen, Dermot Diamond, Albert PHJ Schenning, and Larisa Florea. Direct laser writing of four-dimensional structural color microactuators using a photonic photoresist. *ACS nano*, 14(8):9832–9839, 2020.

[121] Michelle T Brannum, Aubrey M Steele, Maxwell C Venetos, LaShanda TJ Korley, Gary E Wnek, and Timothy J White. Light control with liquid crystalline elastomers. *Advanced Optical Materials*, 7(6):1801683, 2019.

[122] Yuchen Wang, Jiaqi Liu, and Shu Yang. Multi-functional liquid crystal elastomer composites. *Applied Physics Reviews*, 9(1):011301, 2022.

[123] Angel Martinez, Arul Clement, Junfeng Gao, Julia Kocherzat, Mohsen Tabrizi, and M Ravi Shankar. Thermomechanically active electrodes power work-dense soft actuators. *Soft Matter*, 17(6):1521–1529, 2021.

[124] Jiachen Zhang, Yubing Guo, Wenqi Hu, Ren Hao Soon, Zoey S Davidson, and Metin Sitti. Liquid crystal elastomer-based magnetic composite films for reconfigurable shape-morphing soft miniature machines. *Advanced Materials*, 33(8):2006191, 2021.

[125] Chenrun Feng, Chathuranga P Hemantha Rajapaksha, Jesus M Cedillo, Camilo Piedrahita, Jinwei Cao, Vikash Kaphle, Björn Lüssem, Thein Kyu, and Antal Jákli. Electroresponsive ionic liquid crystal elastomers. *Macromolecular rapid communications*, 40(19):1900299, 2019.